



A fundamental study of organic scintillation for X-ray dosimetry in medical imaging

Mauricio Nicolàs Torres Ruiz

► To cite this version:

Mauricio Nicolàs Torres Ruiz. A fundamental study of organic scintillation for X-ray dosimetry in medical imaging. Physics [physics]. Université de Strasbourg, 2014. English. NNT : 2014STRAE042 . tel-02918102

HAL Id: tel-02918102

<https://theses.hal.science/tel-02918102>

Submitted on 20 Aug 2020

HAL is a multi-disciplinary open access archive for the deposit and dissemination of scientific research documents, whether they are published or not. The documents may come from teaching and research institutions in France or abroad, or from public or private research centers.

L'archive ouverte pluridisciplinaire **HAL**, est destinée au dépôt et à la diffusion de documents scientifiques de niveau recherche, publiés ou non, émanant des établissements d'enseignement et de recherche français ou étrangers, des laboratoires publics ou privés.

École Doctorale de Physique et Chimie Physique

IPHC UMR7178

THÈSE

présentée par :

Mauricio Nicolás TORRES RUIZ

soutenue le : 18 décembre 2014

pour obtenir le grade de : **Docteur de l'université de Strasbourg**

Discipline/ Spécialité : Physique

A Fundamental Study of Organic Scintillation for X-ray dosimetry in Medical Imaging

THÈSE dirigée par :

M. JUNG, Jean-Marc

M. BARILLON, Rémi

Prof., IPHC, CNRS, Strasbourg, France – Directeur de thèse

Prof., IPHC, CNRS, Strasbourg, France – Co-directeur de thèse

RAPPORTEURS :

M. FATTAHI-VANANI M.

M. FROMM M.

Prof., Laboratoire SUBATECH, Nantes, France

Prof., Laboratoire Chrono-environnement, Besançon, France

AUTRES MEMBRES DU JURY :

M. NOURREDDINE, Abdel-Mjid

M. KUNTZ, F.

Prof., IPHC, CNRS, Strasbourg, France

Dr. AERIAL, Strasbourg, France

Acknowledgements

This PhD is the result of 3 years of research at the group of Radiochimie in the Institut Pluridisciplinaire Hubert Curien. During this period, I discovered that a PhD is not a single man adventure; it is constructed with the support and guidance of many who come along the path to help you reach your goals. It is also composed of great and less great moments, nevertheless I cherished every single one of them; they enriched me as a person and as a scientist.

First and foremost, I would like to express my most sincere gratitude to my supervisor, Professor Jean-Marc Jung, who was my mentor. Without his support and trust, this work could have never been accomplished. I would like to specially thank my co-supervisor, Professor Remi Barillon for his scientific advice and the insightful discussions and suggestions. I would like to thank Professors Fromm, Fattahi-Vanani and Nourreddine for accepting my invitation to be members of my jury and for their valuable recommendations to improve the quality of this dissertation.

To the group of Radiochimie, I would like to thank you for your warm welcome and good moments. Sylvia, the pool was fun indeed. Ali, we always need good football in life and a place where to watch it. Dariia, thanks for the good moments and laughs. Special thanks to Christophe Hoffmann for his help developing the experimental setup.

To all my friends who were with me throughout these years, thank you! You were the ones who broke the monotony and let me escape of the daily life routine. Arnaud and Katherine (and little Niels), thank you for so many interesting and fun moments (and future ones). We may not be able to change the world, but most important, it won't be able to change us either. Leslie, from sha, sha, sha and shoulder movements to freedom passing by... so many things. Luc, you and your family always made me feel like home. Cerrah, Strasbourg, Paris, Berlin. Pierre & Vincent & Gaël, thanks for your friendship.

To those who shared kilometers and kilometers on a saddle on the mountain or the road,

Acknowledgements

thank you for your company and adventurous spirit. It's nice to rediscover the beauty and value of simple things.

I would like to express my most sincere thanks to those who took care of me and gave me their support during the most difficult moments of this PhD, two surgeries. Without you, achieving this work would have been impossible.

A mis amigos, gracias por su compañía desde las lejanas tierras de los escarabajos y el café. Alvaro, gracias por su amistad y apoyo; siempre pude contar con ud. William, gracias por creer bro. Panita, desde el norteamericano hasta el doctorado.... Y Zoita, eres mi hermanita !

Una dedicación muy especial para mi familia. Gracias por entender que aunque no fue fácil haber dejado tanto atrás para cumplir un sueño, hubiese sido más difícil haber dejado un sueño atrás. A mi papá, gracias por atravesar el Atlántico para venir mi defensa, que gran honor haber contado con tu presencia. A mi mamá, gracias por mostrarme la existencia de la ciencia desde una muy temprana edad y que el conocimiento e inteligencia son para cuidar, valorar y desarrollar.

E para Juliana, obrigado por estar aqui e aí. Você foi uma fonte incessante de coragem e esperança, e me mostrou o valor real de um segundo..

Contents

Acknowledgements

List of figures	1
List of tables	3
Abbreviations	7
Introduction	9
1 Principles of the Interaction of Radiation with Matter	13
1.1 Interactions Between Light and Matter	15
1.1.1 Transition by Coupling of an Electromagnetic Wave	15
1.1.2 Mechanisms of Interaction	21
1.1.2.1 The Photoelectric Effect	21
1.1.2.2 Compton Scattering	24
1.1.2.3 Pair Creation	25
1.1.3 The Absorption of Photons in Matter	27
1.2 Charged Particles Interaction with Matter	29
1.2.1 Interaction of Ions with Matter	31
1.2.2 Interaction of Electrons with Matter	33
1.2.2.1 The Mass Stopping Power	33
2 Organic Scintillation	37
2.1 The Primary Processes	40
2.2 Evolution of the Primary Processes	41
2.3 Evolution of the lowest energy states	43
2.4 The Light Emission	46
2.4.1 The prompt component	47
2.4.2 The Delayed Component	48

Contents

2.4.2.1	The Triplet-Triplet Annihilation	48
2.4.2.2	Fluorescence by Ion Recombination	50
2.4.3	The Total Intensity	54
2.5	Dose and Luminescence	55
2.5.1	Organic Scintillators in Dosimetry	55
2.5.2	The Cavity Theory	56
2.5.3	The Birks Scintillation Model	59
2.5.4	The Voltz Model	60
3	The Experiment	63
3.1	The Fluorescence Observable	64
3.2	The Time-Correlated Single Photon Counting	66
3.2.1	The Mathematics behind the TCSPC	68
3.2.2	The Experimental Error	70
3.2.2.1	Counting Error	70
3.2.2.2	Accidental Coincidence	71
3.3	The Experimental Setup	72
3.3.1	The Photomultiplier Tube	73
3.3.2	The START and STOP Photomultiplier Tubes	75
3.3.3	The Electronic Chain	75
3.3.4	The Cube	76
3.3.5	The Scintillators	78
3.3.6	The X-Ray Machine	78
3.3.6.1	The Principles of X-Ray Generation	79
3.3.7	The Ionization Chamber	81
4	Experimental Results and Data Analysis	83
4.1	Fluorescence Decay Fitting	84
4.1.1	The Exponentially Modified Gaussian Distribution	86
4.1.2	Fit of the Measured Decay Curve	87
4.2	Results	90
4.2.1	Tables of Results	90
4.2.1.1	p-Terphenyl	91
4.2.1.2	Anthracene	92
4.2.1.3	σ and the Instrument Response	92
4.2.2	Graphs	94

4.2.2.1	Babyline	94
4.2.2.2	p-Terphenyl	95
4.2.2.3	Anthracene	105
5	Discussions, Conclusions and Perspectives	113
A	Poisson Counting	125
B	TPCSP Modules	129
C	EMG Fit Before the Fluorescence Peak	133
	Résumé	135
	Bibliography	155

List of Figures

1.1	The Photoelectric effect	22
1.2	Potential well with real and final wave functions	23
1.3	The Compton scattering	24
1.4	Pair creation	26
1.5	Photon Cross-Sections in for water	27
1.6	Absorption of photons in matter	28
1.7	Mass stopping power for liquid water-proton interaction	31
1.8	Bremsstrahlung radiation emitted as the electron passes about the nucleus where it is deviated and de accelerated.	34
1.9	Total stopping power for liquid water-electron interaction	35
2.1	Schema of the distribution of different high activation regions	42
2.2	Superexcited state evolution	43
2.3	The Jablonski Diagram	45
2.4	Franck-Condon Principle and Stokes' shift	46
2.5	Fluorescence Decay Curve	55
3.1	Principle of the generation and acquisition of the histogram	67

List of Figures

3.2	Left : Decay curves a,b and c with no pile up . Right : Pile up distortion of a, b and c	67
3.3	Signal photon count signal as observed in an oscilloscope during experiment setup	68
3.4	Experimental Saturation	70
3.5	Block diagram of the TCSPC setup	73
3.6	Components of the photomultiplier tube (PMT)	74
3.7	Electronic components used for the TCSPC	76
3.8	The cube where the PMTs are screwed, the sample and collimator are placed.	76
3.9	Lead collimator : guides X-rays & helps reducing backscattering radiation.	76
3.10	Experiment configuration inside the X-ray machine	77
3.11	The CP-160 Cabinet X-radiator System	79
3.12	X-ray energy spectrum	81
3.13	The Camberra Babyline 81	82
4.1	Convolution, Observed Measurement and Deconvolution	84
4.2	Raw data of the fluorescence decay curve	88
4.3	Fit results of the fluorescence prompt component.	89
4.4	Fluorescence decay curve for p-Terphenyl	89
A.1	The Poisson Distribution for different values of λ	126
B.1	The TAC principle	130
B.2	Histogram	131
C.1	Histogram of the Leading Edge mode	134

C.2 Histogram of the CFD mode	134
-------------------------------------	-----

List of Tables

1.1	Table of terms used in the Bethe-Bloch formula	32
2.1	Most common organic scintillators	39
2.2	List of processes of the lower energy states leading to the ground molecular state.	44
2.3	Characteristic times of different processes starting from energy absorption by the organic scintillator to the relaxation by light emission.	45
3.1	Characteristics of the organic scintillators used in this work.	78
4.1	Results for different kV at 3mA for p-Terphenyl	91
4.2	Results for different kV at 7mA for p-Terphenyl	91
4.3	Results for different kV at 7mA for p-Terphenyl	91
4.4	Results for different kV at 3mA for anthracene	92
4.5	Results for different kV at 5mA for anthracene	92
4.6	Results for different kV at 7mA for anthracene	92
4.7	Fitting values obtain for sigma for p-Terphenyl.	93
4.8	Fitting values obtain for sigma for anthracene.	93

List of Abbreviations

Abbreviation	Meaning
CFD	Constant Fraction Discriminator
CSDA	Continuous slowing down approximation
EMG	exponentially modified Gaussian
FWMH	Full Width at Half Maximum
IRF	Instrument response function
LE	Leading-Edge
MCA	Multichannel Analyzer
SD	Standard deviation
TAC	Time-to-Amplitude Converter
TCSPC	Time-Correlated Single Photon Counting

*"A journey of a thousand miles
begins with a single step."*

Laozi

Introduction

On January the 26th, 1896, the *Academie de Sciences* in Paris discovered the first X-ray images ever made by Röntgen at the end of November 1885. Röntgen explained that while working with a light-proof protected Crookes tube in his dark laboratory, he had observed a plate coated with barium platino-cyanide placed across the room from tube, glowed every time the tube was activated. Among the list of personalities invited to the event, Henri Poincaré, brilliant French mathematician and Henri Becquerel, who came from a distinguished family of scientists and scholars, was passionate by luminescence phenomena and professor at the Museum of Natural History and *Ecole Polytechnique*. Both French were particularly interested by this groundbreaking results. Becquerel believed that luminescence and X-rays were somehow related. He designed an experiment to study the luminescence by exposing a fluorescent to sunlight. A metallic object was placed between the fluorescent material and photographic plates, very similar to the ones used by Röntgen for his X-ray images. If any kind of emission was to be emitted, the shape of the metallic object would appear on the photographic plate. On the day he was planning to do his experiment, no sun was up in the sky. Becquerel wrapped up the photographic plates to protect them from the sun along with some uranium salts. To his surprise, several days later when he unwrapped the plates, he discovered the presence of some kind of image on the photographic plates. He discovered that this new kind of radiation had some properties in common with the X-rays, though it was more intense as it could traverse thicker layers of materials than X-rays and could be deviated by an external magnetic field, proof of the existence of charge. His work led to discover that air was formed by atoms and that uranium salts somehow interacted with the electrons. In other words, during his experiments, air was being ionized! The electroscope, built by Pierre Curie, was used by Becquerel to detect these ionizations, making him the first to detect nuclear radiation. Nevertheless he was never capable of explaining the origin of the radiation which was named after him, the Becquerel rays.

Simultaneously, Pierre and Marie Curie discovered Polonium. Becquerel studied this new

Introduction

element and discovered a new type of radiation, named beta radiation, made of electrons.

Between 1896 and 1899 X-rays and radioactivity were discovered including the construction of a machine capable of measuring the ionization of the air. It was until 1925, when Geiger, former student of Ernest Rutherford, created the first ionization chamber which is until today, the primary standard dosimetry device.

The first one to study luminescence phenomena was Alexandre Edmond Becquerel, father of Henri Becquerel, and who also discovered the photovoltaic effect in 1839. In 1857 created the phosphoroscope, a device to measure the luminescence (phosphorescence) resolved in time. In the 50's, research of luminescence took a huge leap thanks to Birks who studied scintillation in organic molecules (anthracene, benzene, xylene, etc.). His work led to a more complete comprehension of the mechanisms of excitation and relaxation and their corresponding yields (internal conversion, intersystem conversion, radiationless transitions, etc.). Birks was the first to study scintillation counting as well. His research showed for the first time that the fluorescence was composed of two different components, prompt and delayed. He also proposed a semi-empirical model between luminescence response and specific energy loss. Later in the 70's, the theoretical and experimental research of scintillation mechanisms took place in the *Centre National de Recherches Nucléaires* (CNRS) located in Strasbourg, where Laustriat, Voltz and Klein continued the work started by Birks. The developed models in Strasbourg described the creation and temporal evolution of geminate pairs after ionization by the incident radiation. Their work helped understand the temporal evolution, at a nanosecond scale, of pairs of spins in the singlet and triplet state responsible of the emission of fluorescence and phosphorescence. They improved the instruments used to measure fluorescence and developed for the first time a nanosecond resolved device modulated by an external magnetic field based on the nuclear coincidence experiments. This technique is known as the TCSPC or Time-Correlated Single Photon Counting Technique.

This research is focused on the dosimetry of X-rays with p-Terphenyl and anthracene, two different kind of organic scintillators. The objective of this fundamental research is to study the processes involved in fluorescence of an organic scintillator irradiated by a continuous source of X-rays (between 80kV and 140kV). At first, we will study the interaction of X-ray photons with a scintillating molecule. The interaction is described by the classical electric dipole for non ionization transition between vibronic states, followed by a more complete approach that takes into account the existence of quasi-free states in dense mediums. Secondary interactions caused by electrons created by ionization, are explained by the Bethe-Block formula for light charged particles. The evolution of the electron-hole pairs

formed within the scintillator is described by thermal diffusion of charges and the mutual Coulomb field generated between them. The experimental setup chosen to observe the emitted luminescence was the Time-Correlated Single Photon Counting technique (TCSCP). It was fully developed and adapted to detect X-rays with energies similar as those used in medical applications.

This work is divided in 5 chapters. The first one is dedicated to the matter-ray interactions and the coupling of matter with radiation, with special attention to X-ray matter-interaction and the deposit of energy by primary and secondary particles. In chapter 2, the different processes involved in organic scintillation in dense mediums will be presented and explained, as scintillation is the experimental observable on which this work is based. Birks and Voltz models are introduced at the end of the chapter, which are necessary for the interpretation of the results further on. The third chapter explains, at first, the basis and theory of the experiment used to acquire all the fluorescence decay curves for this work. Then, a complete description on how the experiment setup was built is presented along with mechanical aspects and electronic details. In chapter 4, the results obtained under different experiment conditions and the respective analyze are presented, preceded by a detail description of the the algorithm used to analyze the data. Finally, discussions and conclusion will be presented in chapter 5.

*"There is no subject so old that
something new cannot be said
about it."*

Fyodor Dostoevsky

1 Principles of the Interaction of Radiation with Matter

Introduction

Ever since the discovery of X-rays by Röntgen in 1895 and of natural radioactivity three years later, the study of the interaction between ionizing radiation and matter has been a dynamic research subject. The understanding of this domain is fundamental as radiation is an essential tool to explore and study the structural and spectral properties of matter in any of its states, from the infinitely small scale of particle physics to the bigger scale of molecular and material physics, passing by nuclear and atomic physics. X

Radiation is commonly defined as the propagation of electromagnetic waves or massive particles through space. As long as radiation does not interact with matter, it is known as the propagation of a certain amount of energy as well. The nature of the incident radiation, characterized by the presence or absence of charge and mass and the amount of energy, characterizes its interaction with matter. Furthermore, this does not imply that matter necessarily absorbs energy when traversed by radiation nor that absorption depends exclusively on the amount of energy carried by radiation.

The term *matter* has a wide range of definitions, though for the purpose of this research which is detection and X-ray dosimetry, matter is defined in two different ways. First, matter is considered to be a continuous medium where energy absorption is described by the stopping power, a continuous and differentiable function related to the coupling between the primary radiation and the traversed medium. Secondary electrons are always described by the Bethe-Block relationship as low energy particles having very low mass. Second, matter may be defined as a discrete medium taking into consideration the atoms and molecules that make it up. This definition is by far closer to reality though much more complex. Interactions are now

localized in space and result from the coupling between primary and secondary radiation to the local proper modes of electronic excitation, both in an intra or intermolecular scale. Let us recall that secondary electrons near thermal equilibrium, with kinetic energy ranging between 10eV and 20eV, cause the most damage to the medium and the vibronic coupling is at its maximum. This second approach allows to assess the local damage underwent by atoms and molecules caused by radiation as opposed to the first definition, where only an approximate average estimation of the damage can be assessed.

Interaction between a continuous medium and radiation is described by the statistical evolution of a very large number of particles interacting among each other and the medium. A transport equation, usually referred to as Boltzmann equation, describes the temporal evolution of the charge distribution in the phase space under the effect of internal and external forces. The time-dependent mean free path, energy loss and the momentum transfer is deduced by the diffusion processes of all particles (collision integral) among each other and the medium, concentration and momentum gradients and entrainment processes. Interaction between radiation and matter considered as a discrete medium is described by Monte-Carlo techniques involving the simulation of all possible events in accordance to physics and probability of occurrence of events. Results obtained with either approach should converge taking account of the law of large numbers.

The couple of matter and radiation is described by a cross-section calculated by average approximation in a continuous medium and ruled by microscopic phenomena in a discrete medium. Two distinct types of coupling exist in matter-ray interactions regardless the nature of incident radiation or difference between primary or secondary particles: i) interactions leading the *non-ionizing* excitation of the molecule and/or medium; ii) interactions leading to ionization. The result of these interactions is a deposit of energy in the medium in most of the cases, though only the second one is considered when a dose is measured by the standard detector, the ionization chamber. An ionization is defined as the transition from a bounded state to a quasi-free state of an electron. In weakly bounded mediums in dense or gas phases, though the initial electronic bounded states are similar, the final state depend on the nature of the matter and conductivity of the medium. The ionization of the electron is directly related to its initial wave function, hence the final state depends only on the intrinsic characteristics of the medium described by the final wave function.

This chapter is divided in two parts. Firstly, the interaction between photons and matter is described by the coupling of electromagnetic radiation and charge. Cross-sections between atomic or molecular bounded states are introduced followed by the dipolar approximation.

Next, the transition between a weakly bounded atomic or molecular state to a quasi-free state is described. This first part presents the needed theory to study excitation and ionization by X-rays. The interaction between particles with mass and matter is introduced in the second part of this chapter, with an special emphasis on the electron-matter interaction. Indeed, X-ray generate secondary electrons, therefore, the need to better understand this interaction.

1.1 Interactions Between Light and Matter

An introduction of the fundamental aspects of the interaction between light and matter will be followed by a brief description of the different processes resulting from this interaction: the photoelectric effect, the Compton scattering and pair creation.

1.1.1 Transition by Coupling of an Electromagnetic Wave

The different transition cross-sections can be deduced by solving Schrödinger's equation by defining the total Hamiltonian H of the system at first. The perturbation theory provides a first order solution considering a small displacement of the charge under the electromagnetic field[1]. Let us start by defining the Hamiltonian H :

$$H = H_M + H_L + H_{LM}, \quad (1.1)$$

where H_M is the matter Hamiltonian, H_L is the light Hamiltonian, and H_{LM} is the Hamiltonian corresponding to the light-matter interaction. As our interest is focused on the effects of light on matter and not the opposite, H_L may be neglected. H will be approached in a semiclassical way, where H_M and H_{LM} are treated using quantum mechanics and classical physics respectively[2]. Relation 1.1 can be expressed in terms of H_0 , the matter unperturbed Hamiltonian considered to be independent of time, and $V(t)$, the light-matter classical Hamiltonian:

$$H = H_0 + V(t). \quad (1.2)$$

To determine $V(t)$, the electromagnetic field has to be expressed in terms of the magnetic vector potential $\vec{A}(\vec{r}, t)$ and a scalar potential $\varphi(\vec{r}, t)$ [3]. The scalar potential must be used

Chapter 1. Principles of the Interaction of Radiation with Matter

because a description of a varying potential in space and time is needed for the construction of the Hamiltonian. The electromagnetic field is generally expressed using Maxwell's equations[4] in vacuum 1.3:

$$\begin{aligned}\vec{\nabla} \cdot \vec{E} &= \frac{\rho}{\epsilon_0} & \vec{\nabla} \times \vec{E} &= -\frac{1}{c} \frac{\partial \vec{B}}{\partial t}, \\ \vec{\nabla} \cdot \vec{B} &= 0 & \vec{\nabla} \times \vec{B} &= \mu_0 \left(\epsilon_0 \frac{\partial \vec{E}}{\partial t} + \vec{J} \right),\end{aligned}\tag{1.3}$$

where c is the speed of light, \vec{E} is the electric field, \vec{B} the magnetic field, ϵ_0 and μ_0 the permittivity and permeability of free space respectively, ρ is the free electric charge density and \vec{J} the conduction common density. In dense matter, the permittivity and permeability terms must be replaced to consider the characteristics of the medium.

The plane wave solution for the electric field is:

$$\vec{\nabla}^2 \vec{E}(\vec{r}, t) + \frac{1}{c^2} \frac{\partial^2 \vec{E}(\vec{r}, t)}{\partial t^2} = 0.\tag{1.4}$$

The plane wave solution for the magnetic field \vec{B} is the same as above.

The electromagnetic wave solution depends on 6 variables (E_x, E_y, E_z, B_x, B_y and B_z where x, y and z are the spatial axis) and due to Maxwell's equations, the problem is overdetermined. On the other hand, the potential vector is represented by only four variables (A_x, A_y, A_z and ϕ) leading to multiple possible solutions for the potential vector. This is avoided by choosing a gauge. A current choice is the Coulomb gauge where $\varphi(\vec{r}, t) = 0$ and $\vec{\nabla} \cdot \vec{A} = 0$ [5]. Moreover, knowing that in vacuum $\vec{J} = 0$ and that $\rho = \mu = 1$, the electromagnetic wave can be written as:

$$\vec{\nabla}^2 \vec{A}(\vec{r}, t) + \frac{1}{c^2} \frac{\partial^2 \vec{A}(\vec{r}, t)}{\partial t^2} = 0,\tag{1.5}$$

and it admits a wave solution of the form:

$$\vec{A}(\vec{r}, t) = A_0 e^{i(\vec{k} \cdot \vec{r} - \omega t)} \hat{n} + A_0^* e^{-i(\vec{k} \cdot \vec{r} - \omega t)} \hat{n}, \quad (1.6)$$

where \hat{k} is the wave propagation vector, ω is the frequency, A_0 is the wave amplitude and \hat{n} the polarization vector unit. This leads to \vec{E} and \vec{B} be written as:

$$\vec{E} = -\frac{\partial \vec{A}}{\partial t}, = i\omega \vec{A} \quad (1.7)$$

and

$$\vec{B} = \vec{\nabla} \times \vec{A} = i\vec{k} \times \vec{A}, \quad (1.8)$$

where ω describes an angular frequency.

Let us now introduce Lorentz equation[6] that describes the force that acts on a particle with charge q moving with a velocity \vec{v} in the presence of an external electric and magnetic field:

$$\vec{F} = q(\vec{E} + \vec{v} \times \vec{B}). \quad (1.9)$$

Writing Lorentz equation in Lagrangian mechanics[7] for the x-direction component:

$$F_x = -\frac{\partial U}{\partial x} + \frac{d}{dt} \left(\frac{\partial U}{\partial v_x} \right), \quad (1.10)$$

where U is the total potential energy.

Using equations 1.7, 1.8, 1.9) and 1.10, the total potential energy can now be written as:

$$U = q\varphi - q\vec{v} \cdot \vec{A}. \quad (1.11)$$

Let us define the total Lagrangian L :

$$L = T - U, \quad (1.12)$$

where T represents the kinetic energy and U , the potential energy defined above. By replacing the total potential energy given by 1.10, the total Lagrangian L becomes:

$$L = \frac{1}{2} m \vec{v}^2 + q \vec{v} \cdot \vec{A} - q\varphi, \quad (1.13)$$

where m is the mass of the particle.

The relationship between the classical Hamiltonian of the system and the Lagrangian is:

$$H = \vec{p} \cdot \vec{v} - L, \quad (1.14)$$

where \vec{p} is the momentum. Therefore, taking into consideration the conservation laws in Lagrangian mechanics, the following relationship is deduced:

$$\vec{p} = \frac{\partial L}{\partial \vec{v}} = m \vec{v} + q \vec{A}. \quad (1.15)$$

Expanding and regrouping 1.14 using 1.15, the classical Hamiltonian for a charged particle in an electromagnetic field turns out to be:

$$H = \frac{1}{2m} [\vec{p} - q \vec{A}(\vec{r}, t)]^2 + q\varphi(\vec{r}, t), \quad (1.16)$$

where the term $\varphi(\vec{r}, t)$ is equal to 0 due to the previous gauge choice.

The Hamiltonian for multiple particles in the absence of an electromagnetic field is given by the sum of the kinetic and potential energy:

$$H_0 = \sum_i \left(\frac{\vec{p}_i^2}{2m_i} + V_0(\vec{r}_i) \right). \quad (1.17)$$

H_0 is set to be, in presence of an external electromagnetic field:

$$H = \sum_i \left(\frac{1}{2m_i} (\vec{p}_i - q_i \vec{A}(\vec{r}_i))^2 + V_0(\vec{r}_i) \right). \quad (1.18)$$

Having obtained H_0 and H and according to formula 1.2, the classical Hamiltonian $V(t)$ describing the electromagnetic interaction with matter is:

$$V(t) = \sum_i \frac{q_i}{2m_i} (\vec{p}_i \vec{A} + \vec{A} \vec{p}_i). \quad (1.19)$$

Replacing x and \vec{p} by their quantum equivalent operators \hat{x} and $-i\hbar\vec{\nabla}$ in equation 1.18, $V(t)$ becomes:

$$\hat{V}(t) = \sum_i \frac{q_i}{2m_i} i\hbar (\vec{\nabla}_i \vec{A} + \vec{A} \vec{\nabla}_i), \quad (1.20)$$

the quantum Hamiltonian and \hbar Planck's reduced constant.

Using the chain rule $[\vec{\nabla} \vec{A} = (\vec{\nabla} \vec{A}) + \vec{A} \vec{\nabla}]$, we find that the quantum Hamiltonian is equal to:

$$\hat{V}(t) = \sum_i \frac{q_i}{m_i} i\hbar \vec{A} \vec{\nabla}_i = - \sum_i \frac{q_i}{m_i} \vec{A} \cdot \vec{p}_i. \quad (1.21)$$

The Dipolar Approximation

The exponential term $\exp[i\vec{k}\vec{r}]$ in the scalar potential \vec{A} presented in equation 1.6 can be developed in Taylor series, as:

$$\exp[i\vec{k}\vec{r}] = \exp[i\vec{k}\vec{r}_0] \exp[i\vec{k}(\vec{r}_i - \vec{r}_0)] = \exp[i\vec{k}\vec{r}_0] [1 + i\vec{k}(\vec{r}_i - \vec{r}_0) + \dots], \quad (1.22)$$

where \vec{r}_0 is defined as the center of mass of the system and \vec{r}_i the position of the i -th particle. to the center of mass.

Chapter 1. Principles of the Interaction of Radiation with Matter

The dipolar approximation consists [8] on neglecting all the terms in the series except the first one to be in the small displacement limit.

This approximation is possible in two cases:

- For nuclei: $k \ll \frac{1}{R_n} \Leftrightarrow E \ll 200 \text{ MeV}$
- For atoms: $k \ll \frac{1}{R_a} \Leftrightarrow E \ll 2 \text{ keV}$,

where k is the wavenumber, E the energy of the incident photon, R_n and R_a the nuclear and atomic postions respectively. For smaller energies, other approximations are proposed as seen in [9].

Now let us write again equation 1.21 considering the truncated taylor expansion and replacing the term A_0 by $i E_0/2\omega$. This leads to:

$$\hat{V}(t) = \frac{-iqE_0}{2m\omega} [(\vec{p}e^{-i\omega t} - \vec{p}e^{i\omega t})\vec{n}]. \quad (1.23)$$

Setting equation 1.23 to describe a many particle situation, the Hamiltonian can be written as:

$$\hat{V}(t) = \left(\sum_i \frac{q_i}{m_i} (\vec{p}_i \vec{n}) \right) \frac{E_0}{\omega} \sin(\omega t), \quad (1.24)$$

expression known as and the *electric dipole Hamiltonian*, which describes the interaction of matter and light.

The electric dipole Hamiltonian $\hat{V}(t)$ allows to find the transitions rates generated by $V(t)$ using the first order perturbation theory[10]. The matrix elements can be found using Fermi's golden rule to finally obtain the cross section given by:

$$\sigma = \frac{16\pi^2 q^2}{c \hbar} (E_i - E_f) r_{ij} \rho(E), \quad (1.25)$$

where $r_{ij} = \langle f | \vec{p} \vec{n} | i \rangle$ are the matrix elements of the electric dipole Hamiltonian, c , the speed of light, \hbar is the reduced Plank's constant, E_i and E_f the initial and final energy values and

$\rho(E)$ represents the density of final states.

1.1.2 Mechanisms of Interaction

There are four main interactions which lead to the loss of energy or total absorption of the photon in matter. The most important interaction in regard to this work is the photoelectric effect followed by the Compton scattering. The pair creation are presented as well though they are not relevant in this work[11].

1.1.2.1 The Photoelectric Effect

In this interaction, the incident photon is totally absorbed by the atom (figure 1.1). The photon transfers its energy, $E = h\nu$, to a K-shell electron from the atom. If the incident energy is bigger than the binding energy E_b , the electron is ejected with an initial kinetic energy E_k . The recoil energy E_r of the atom may be sometimes neglected when the incident energy is much smaller than the mass energy of the target atom ($h\nu \ll Mc^2$ where M)[12].

Energy and Momentum Conservation

The total energy and momentum conservation is given by the following equations:

$$E_k + E_r = h\nu - E_b. \quad (1.26)$$

$$\vec{p}_\gamma = \vec{p}_e + \vec{q}, \quad (1.27)$$

where \vec{p}_γ , \vec{q} and \vec{p}_e are the photon, electron and nucleus momentum respectively. This leads to define the incident energy of the photon $h\nu$ as:

$$h\nu = E_b + \frac{p_e^2}{2m} + \frac{q^2}{2M}, \quad (1.28)$$

where m is the mass of the electron and M the mass of the nucleus. Developing the previous

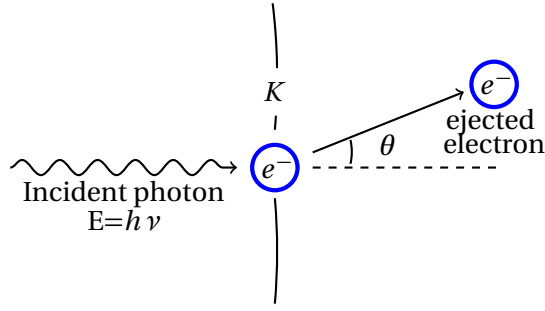


Figure 1.1 – The photoelectric effect - The energy of the incident photon is totally absorbed by a K-shell electron which is ejected from its orbital with a kinetic energy E_k .

equation, we can finally write:

$$h\nu = E_b + \frac{p_e^2}{2m} + \frac{h^2\nu^2}{2Mc^2} - \frac{p_e}{Mc} h\nu \cos \theta \quad (1.29)$$

Transition Cross-Section

Let us approach the photoelectric effect by considering the initial state of a weakly bound electron¹ in a finite potential well with a width L , as depicted in figure 1.2. This electron is described by the following plane wave function:

$$\psi_i(x) = \sqrt{k_B} e^{-k_B|x|}; E_i = \frac{\hbar^2 k_B^2}{2m}. \quad (1.30)$$

The final state of the electron is described by the quasi-free electron model. Taking into account the wave vector \vec{k}_e , the wave in the final state and the kinetic energy, E_k , of the electron are:

$$\psi_f(x) = \frac{1}{\sqrt{L}} e^{-k_e|x|}; E_k = \frac{\hbar^2 k_e^2}{2m}. \quad (1.31)$$

The cross ionization section σ_{pe} is :

¹Weakly bound means $E_b/h\nu \ll 1$

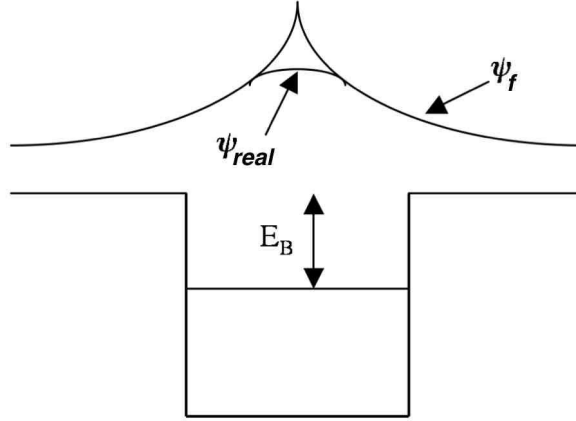


Figure 1.2 – Potential well with real and final wave functions

$$\sigma = \frac{16\pi^2 e^2 (E_i - E_f)}{c \hbar} \frac{16}{L} \frac{k_e^2 k_B^3}{(k_e^2 + k_B^2)^4} \frac{L}{2\pi \hbar} \sqrt{\frac{2m}{E_e}} = 128\pi \frac{e^2}{\hbar c} \frac{k_e^3 k_B^3}{(k_e^2 + k_B^2)^4} \quad (1.32)$$

Equation 1.32 turns out to be:

$$\sigma_{pe} = 64\pi \frac{e^2 \hbar}{mc} \frac{E_B^{3/2}}{E_e^{5/2}}. \quad (1.33)$$

when the incident energy is higher to the binding energy. As we can see, the cross section follows a $E_k \sim E^{-5/2}$ power law meaning that σ_{pe} varies inversely proportional to E_e . By neglecting the binding and recoil energy terms in equation 1.26, we can see that $h\nu \sim E_k$, therefore $\sigma_{pe} \sim E^{-5/2}$ [13]im.

The photoelectric effect is dominant for energies under 200KeV. Thereby, it plays a major role among the other energy loss mechanisms for primary photons, specially in the X-ray spectral domain studied in this work.

After the photoelectric effect has taken place, an outer shell electron fills the vacancy left by the ejected electron in the inner shell. This electronic transition irradiates and emits a *fluorescence X-ray photon*. If this photon interacts with an outer shell electron and ejects it from its orbital, it would generate an electron known as *Auger electron*.

1.1.2.2 Compton Scattering

The Compton scattering illustrated by figure 1.3 is the interaction between an incident photon of energy $h\nu$ with an outer shell electron in the atom and it is most likely to occur for energies between some hundred keV and 10MeV[14]. The photon transfers some of its energy and gets deflected from its original trajectory. For incident energies greater than the binding energy, E_b , the electron is ejected from its orbital.

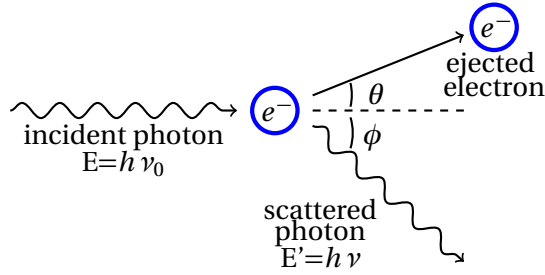


Figure 1.3 – The Compton scattering - The incident photon deposits some of its energy on an electron. The electron gets ejected of its orbital by θ , the angle of deflection and the photon deviated from its original trajectory by the angle ϕ .

The wavelength of the incident photon changes due to the photon-electron interaction. This is known as the Compton shift. Let us start the approach to the problem using classical mechanics and defining the photon momentum 1.34:

$$\vec{p} = \frac{E}{c} = \frac{h\nu_0}{c} = \frac{h}{\lambda_0}. \quad (1.34)$$

with E , the energy of the incident photon, ν_0 its frequency and λ_0 its wavelength. The conservation laws are :

$$h\nu_0 - E_b = E_k + E_r, \quad (1.35)$$

and,

$$\vec{p}_0 = \vec{p} + \vec{p}_e, \quad (1.36)$$

where \vec{p}_0 and \vec{p} are the momenta of the incident photon and scattered photon before and after the collision respectively and \vec{p}_e is the momentum of the ejected electron.

Using the three previous definitions, the final energy of the scattered photon is found to be:

$$h\nu = \frac{h\nu_0}{1 + (\frac{h\nu_0}{m_e c^2})(1 - \cos\theta)}; \xi = \frac{h\nu_0}{m_e c^2}, \quad (1.37)$$

where θ is the angle of the deflection of the electron and $m_e c^2$ its the energy at rest.

Using 1.37, the change in photon wavelength known as Compton shift is found to be:

$$\lambda - \lambda_0 = \frac{h}{m_e c}(1 - \cos\theta), \quad (1.38)$$

and the kinetic energy transferred to the electron is:

$$E_k = \frac{\xi(h\nu_0)(1 - \cos\theta)}{1 + \xi(1 - \cos\theta)} \quad (1.39)$$

From equations 1.38 and 1.39 we can see that the maximum deposited energy occurs when the collision angle θ is equal 180°

The differential-cross section is given by the Klein-Nishina formula :

$$\frac{d\sigma}{d\Omega} = \frac{r_0^2}{2} \frac{1 + \cos^2\theta}{[1 + \xi(1 - \cos\theta)]^2} \left[1 + \frac{\xi^2(1 - \cos\theta)^2}{(1 + \cos^2\theta)[1 + \xi(1 - \cos\theta)]} \right] \quad (1.40)$$

1.1.2.3 Pair Creation

A photon with an energy of at least equivalent to $2m_e^2(1.022MeV)$ can transform into an electron-positron pair². This interaction must take place in the nuclear Coulomb field to conserve the energy and the momentum of the system[15]. During the pair creation, the nuclear recoil may be neglected because of the mass difference between the electron and

²This interaction is presented here for informational purposes only as it is an interaction that can not occur due to the energies we worked with.

the nucleus. The kinetic energy of the created pair is given by:

$$E_{k(e^+)} + E_{k(e^-)} = h\nu - 1.022 \text{ MeV}, \quad (1.41)$$

where $E_{k(e^+)}$ and $E_{k(e^-)}$ are the kinetic energies of the positron and electron.

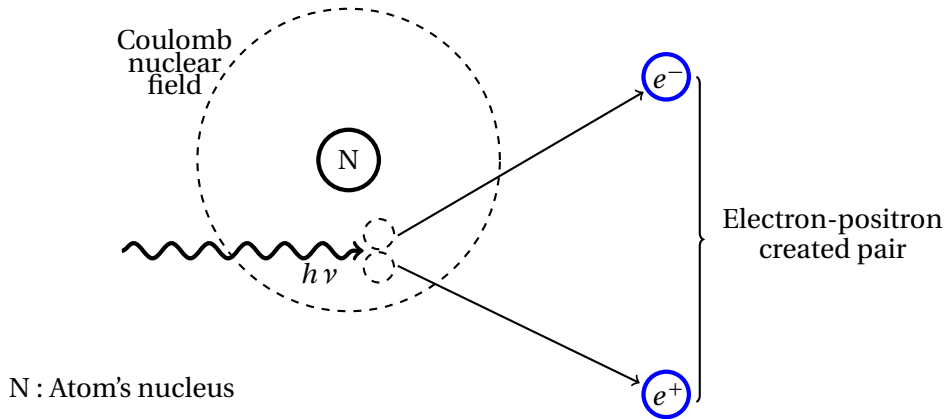


Figure 1.4 – Pair creation - The creation of the pair takes place in the vicinity of a nuclear field and the photon requires a minimum of energy at least equal to two times the mass of an electron.

The cross section for this interaction evolves from $2m_e$ to a constant value for high energies and it is defined as :

$$\sigma_{pair} \approx \frac{7}{9} 4\pi r_e^2 Z^2 \left(\ln \frac{183}{3Z^{1/2}} \right). \quad (1.42)$$

The Total Cross Section

The different cross-sections for the three most probable interactions as well as the total cross-section between photons and water are shown in the following figure:

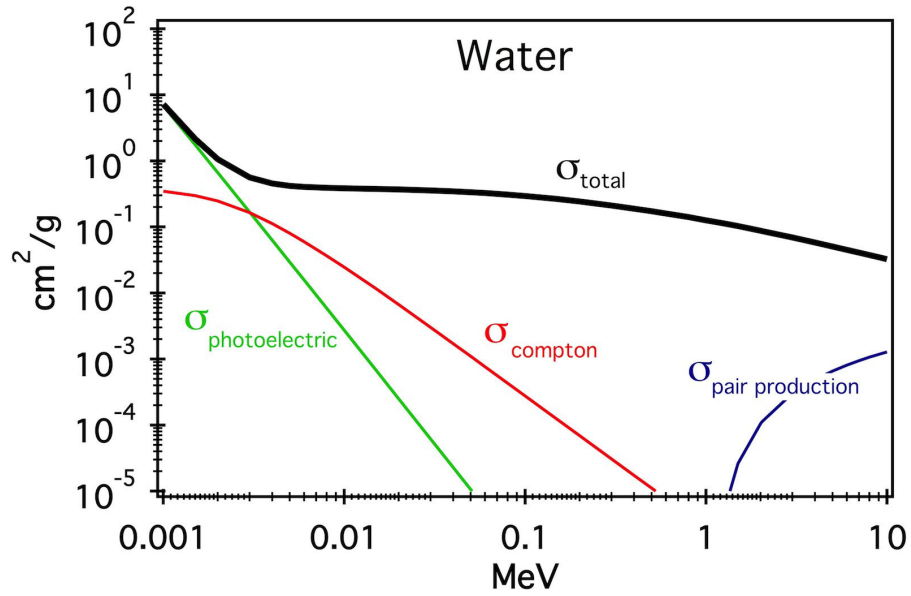


Figure 1.5 – The photon cross-sections in water for energies between 1 keV and 10 MeV. The photoelectric effect is the dominant effect at low energies followed by the Compton effect at middle range energies (see equation 1.46). The pair production becomes dominant for energies above the mass rest energy corresponding to two electrons [16].

1.1.3 The Absorption of Photons in Matter

The mechanism of interaction between a photon beam and matter have been previously presented. As seen, the number of photons of energy $h\nu$ diminishes as they are absorbed or scattered by the matter they cross. The fraction of absorbed mono energetic photons per unit of traversed distance in matter is known as the linear attenuation coefficient, μ (dimensions: length^{-1}).

Let us imagine a narrow beam composed of N_0 mono energetic photons. After crossing a distance x within matter of same density, let us define $N(x)$ as the number of photons remaining in the beam and n , the number of photons absorbed or scattered when the beam crosses a distance defined by Δx as depicted in figure 1.6. The number of photons n is then equal to:

$$n = N(x)\mu dx, \quad (1.43)$$

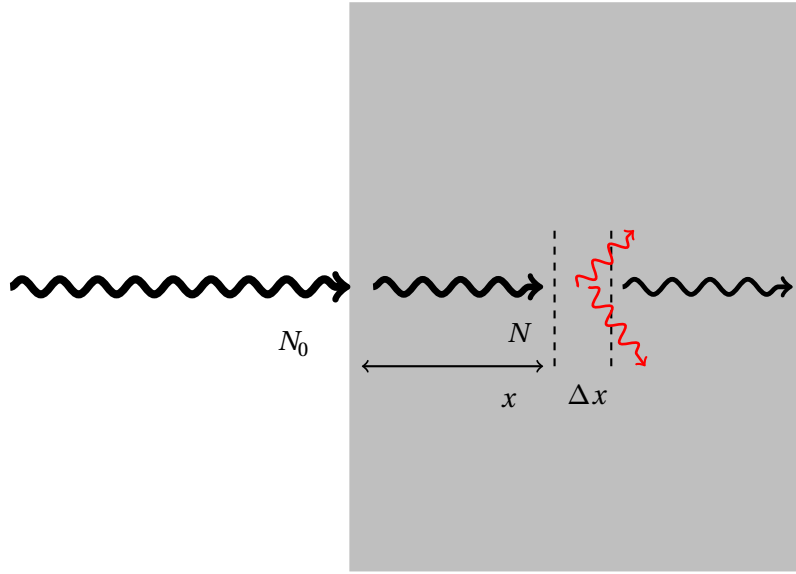


Figure 1.6 – The incident number of photons N_0 decreases as it penetrates matter at a rate determined by n , that represent the number of photons absorbed or scattered in a distance Δx .

In order to solve equation 1.43, the number of photons n in 1.43 may be replaced by $-dN(x)$, the variation of number of photons in the beam. This leads to the following relationship:

$$dN(x) = -N\mu dx, \quad (1.44)$$

and then by integrating the previous relationship, it is deduced that:

$$N(x) = N_0 e^{-\mu x}. \quad (1.45)$$

In order to get rid of the dependency of density of the crossed material in this coefficient and to generalize the expression of the linear attenuation coefficient, μ may be normalized by dividing by the density of the crossed material. This leads to a new coefficient known as the mass attenuation coefficient μ/ρ (units: $\text{length}^2/\text{mass}$) defined by :

$$\frac{\mu}{\rho} = \frac{\mu_e}{\rho} + \frac{\mu_c}{\rho} + \frac{\mu_p}{\rho}, \quad (1.46)$$

1.2. Charged Particles Interaction with Matter

where μ_e/ρ corresponds to the contribution of the photoelectric effect, μ_p/ρ that of the pair production, μ_c/ρ that of the Compton effect.

Theoretically, the total mass attenuation coefficient, μ/ρ , is found by using the following expression:

$$\frac{\mu}{\rho} = \sigma_{total} \frac{N_A}{A}, \quad (1.47)$$

in which N_A is Avogadro's number, A is the relative atomic mass a given crossed material.. The total cross-section σ_{total} is estimated by adding up the contributions of each different cross-section seen in 1.5

1.2 Charged Particles Interaction with Matter

The charged particles mainly lose energy due to the Coulomb interaction with the electrons and nuclei in the medium. High energy charged particles are most likely to interact with the electrons. In fact, the cross-section for particle-electron interaction is approximately one million times bigger than the cross-section for particle-nuclei interaction. Heavy ions (such as protons and alpha particles) traverse the medium essentially in a straight trajectory creating high density areas of ionized and excited atoms around the track. Their penetrating distance within matter is much shorter than that of X-rays because the cross-section of high energy charged particles is bigger.

The loss of energy of charged particles per unit length in matter is given by the *stopping power*, S , which is basic quantity that describes this phenomenon:

$$S = -\frac{dE}{dx}. \quad (1.48)$$

This equation is defined under two general assumptions: first, the incident charged particle moves with a much more higher velocity than the electrons in the medium, and second, this particle is much more heavier than the electrons in the medium.

Dividing the stopping power by the density of the medium leads to the mass stopping power defined as the loss of energy by the incident radiation per unit of distance per unit of mass:

$$S = -\frac{1}{\rho} \frac{dE}{dx}. \quad (1.49)$$

It is usually expressed in J*m²/kg units or MeV*cm²/g.

Depending the nature of the particle, there are two different kind of stopping powers:

- *Collision stopping power*: Both light and heavy charged particles lose energy through soft and hard collisions which may lead to atomic excitation or ionization. Experimentally, the collision stopping power is measured estimating the number of ion pairs created by the incident particle along its track.
- *Radiative stopping power*: Light charged particles such as electrons and positrons may lose energy by radiative means. Coulomb interactions cause the particle to deviate changing its trajectory and speed generating what is known as the Bremsstrahlung³ radiation.

The total stopping power S_{tot} is:

$$S_{tot} = S_{col} + S_{rad}, \quad (1.50)$$

where S_{col} and S_{rad} are the collision and radiative stopping power respectively.

Figure 1.7 shows the mass stopping power of liquid water for protons of energies ranging between 1keV and 10GeV. It is observed that the stopping power increases until a certain energy and then decreases. At that point, the particle has enough kinetic energy to cross the medium without losing as much energy as it did with kinetic energies below that point.

The depth of penetration is characterized by the *range* R is defined as maximum penetration depth once a particle comes to rest after transferring all its energy to the medium. R depends on the initial kinetic energy of the incident particle and the density of the medium. Heavy particles lose energy steadily and undergo small deflection angles tending to have straight trajectory. Light particles may lose all their energy in a single collision and they can be deflected in very large angles.

³It is the German word for *braking radiation*

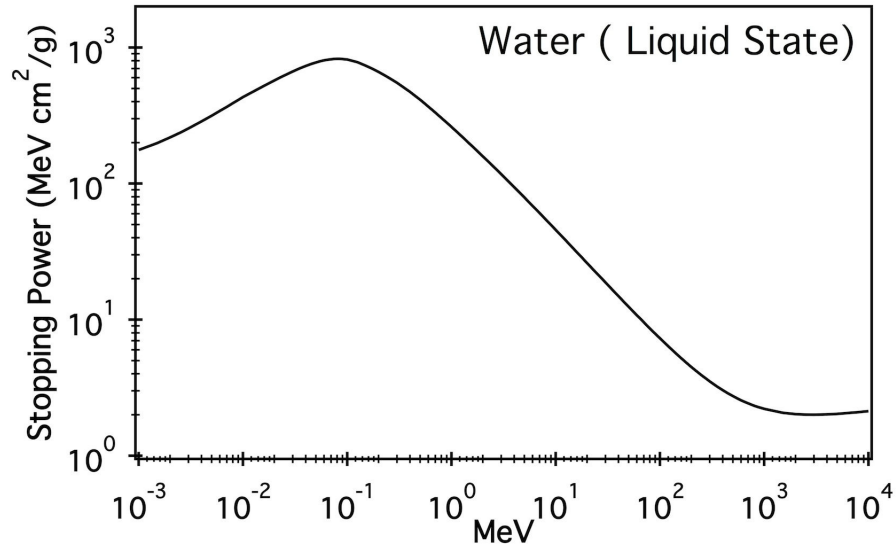


Figure 1.7 – Liquid water mass stopping power for protons -Data by NIST-PSTAR [17]

Regardless the nature of the particle, the range can be approached by the *continuous slowing down approximation* (R_{CSDA}) which means that the particle loses its energy constantly within matter making range estimations easier. R_{CSDA} is obtained by integrating the reciprocal of the stopping power between the total kinetic energy of the incident particle and 0 when the particle has come to rest.

$$R_{CSDA} = \int_0^{E_k} \left(-\frac{dE}{dx} \right)^{-1} dE, \quad (1.51)$$

where E_k is the initial kinetic energy of the incident particle. This approximation has its limits for light particles and in the case of electrons under 5keV, this is no longer valid and other approaches are necessary as studied in [18].

1.2.1 Interaction of Ions with Matter

Bohr was the first one to propose a classical stopping power considering that the ion transferred its energy by delivering individual impulses to the each electron on its path. Later, Bethe approached the problem using quantum mechanics and Bloch completed the formula considering electrons as confined in cylindrical dimensions giving them transverse momentum components instead of treating them as simply plane waves. The result is the

Chapter 1. Principles of the Interaction of Radiation with Matter

Bethe-Bloch stopping power formula which is found to be :

$$S = \frac{\kappa Z_2}{\beta^2} Z_1^2 [L_0(\beta) + Z_1 L_1(\beta) + Z_2^2 L_2(\beta) \dots]. \quad (1.52)$$

The terms found in formula 1.52 are detailed in the following table:

Symbol	Description	Value
Z_1	Incident particle atomic number	-
Z_2	Target atomic number	-
r_0	Bohr's electron radius (e^2/mc^2)	≈ 0.529
m_e	Mass of the electron	$9.1 \times 10^{-31} \text{ kg}$
v	Speed of the particle	m/s
c	Speed of light	$2.99 \times 10^8 \text{ m/s}$
β	Relative speed of the particle v/c	-
κ	$4\pi r_0^2 m_e c^2$	0.0005099 eV
L_0	Fano correction factor	-

Table 1.1 – Table of terms used in the Bethe-Bloch formula

The other corrective terms found in equation 1.52 $L_1, L_2 \dots$ will not be discussed for the sake of simplicity. Let us now define the Fano correction factor L_0 , defined by:

$$L_0 = \frac{1}{2} \ln \left(\frac{2m_e c^2 \beta^2 \Delta E_{max}}{1 - \beta^2} \right) - \beta^2 - \frac{C}{Z_2} - \ln \langle I \rangle - \frac{\delta}{2}. \quad (1.53)$$

The shell correction term $\frac{C}{Z_2}$ allows to adjust the formula due to the prior assumption that the speed of the ion is much bigger than that of the electron in the medium. $\langle I \rangle$ is the mean energy absorbed by the medium and allows to adapt the formula to the different quantum energy levels present in the target material. The $\frac{\delta}{2}$ term takes into consideration the polarization effects within the target. ΔE_{max} is the the maximum possible energy per collision between the incident particle and the medium and it can be approximated to $2m_e v^2$ for non relativistic energies[19].

1.2.2 Interaction of Electrons with Matter

Due the nature of the radiation source and the energies used to irradiate the organic scintillators, the interaction between electrons and matter must be considered as non negligible phenomenon. Indeed, X-rays with energies under 160kV were used to irradiate the organic scintillators and almost all the energy is transferred to the electrons in the medium, generating what is known as *secondary electrons*. These secondary electrons may interact with others electrons producing even more electrons.

There are some difference between the ion-matter and electron-matter interactions which are: Electrons with energies up to 10MeV should be considered as relativistic particles to describe their motion; in the free electron model, the electron-electron scattering is composed of a system of identical fermions; due to the presence of external forces such a nuclear Coulomb forces, the fast moving electron may radiate losing energy in a process known as Bremsstrahlung.

1.2.2.1 The Mass Stopping Power

The collision mass stopping power S_{col}/ρ of the electron is given by 1.54 where the relationship considers the lighter mass of this particle as well as the incident velocities. According to ICRU Report No. 37, the collision mass stopping power is:

$$\frac{S_{col}}{\rho} = \frac{N_A Z}{A} \frac{\pi r_0^2 2 m_e c^2}{\beta^2} \left[\ln \left(\frac{E_k}{I} \right)^2 + \ln(1 + \tau/2) + F^-(\tau) - \delta \right], \quad (1.54)$$

where m_e, I and β are defined in table 1.1, Z is that of the target material, A is the atomic weight of the target material, E_k the kinetic energy of the electron, and τ is given by:

$$\tau = \frac{E_k}{m_e c^2}, \quad (1.55)$$

and

$$F^-(\tau) = 1 - \beta^2 + \frac{\tau^2/B - (2\tau + 1) \ln 2}{(\tau + 1)^2}, \quad (1.56)$$

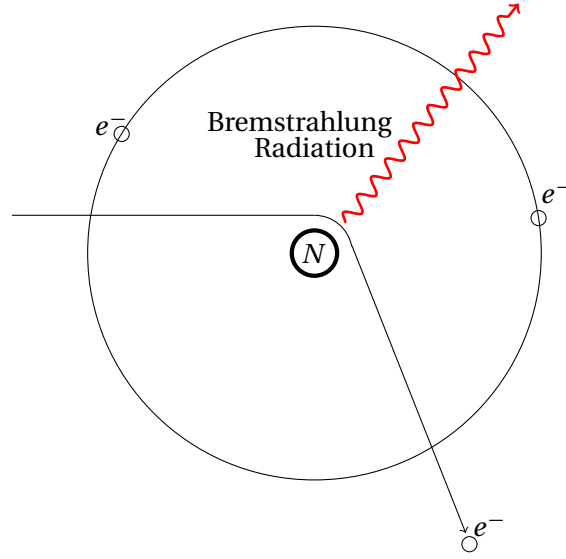


Figure 1.8 – Bremsstrahlung radiation emitted as the electron passes about the nucleus where it is deviated and de accelerated.

is a function related to the nature of the particle, in this case, electrons.

The radiative stopping power is due to the interaction between the incident electron and the nuclear Coulomb field and may generate radiation known as Bremsstrahlung (Figure 1.8). This radiation is emitted by the deceleration and change of trajectory of the electron. The radiative stopping power, S_{rad} , for an electron with kinetic energy E_k is:

$$\frac{S_{rad}}{\rho} = \sigma_0 \frac{N_A Z^2}{A} (E_k + m_e c^2) \bar{B}(Z, E), \quad (1.57)$$

where $\sigma_0 = \frac{1}{137} (\frac{e^2}{m_0 c^2})$ and $\bar{B}(Z, E)$ is a function depending on the atomic number and the energy of the incident electron.

The ratio between S_{rad} and S_{col} , (1.58) shows that the contribution on the total stopping power for electrons is only significant for dense atoms $Z > 80$ and high energy electrons with energies over $10 MeV$.

$$\frac{S_r}{S_e} \approx \frac{ZE}{800 MeV} \quad (1.58)$$

1.2. Charged Particles Interaction with Matter

The total stopping power (the sum of collision stopping power and radiative stopping power) for electrons with energies ranging between 10 keV and 1 GeV in liquid water is shown in graph 1.9. The radiative stopping power starts being significant for electrons with incident energies of about 5 MeV and above. For energies over 100 MeV it is the primary interaction causing the electron to lose energy. On the other hand, electrons with energies under 1 MeV mainly lose their energies colliding with the medium.

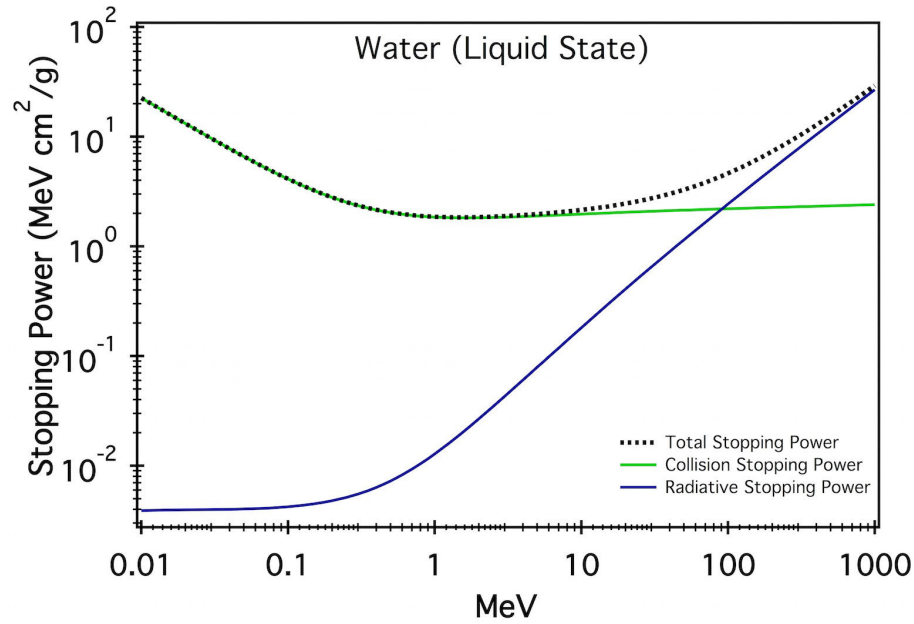


Figure 1.9 – Liquid water total stopping power for electrons -Data by NIST-ESTAR [20]

Finally, electrons may also lose energy through Cherenkov radiation though in a much more smaller scale compared to Bremsstrahlung, hence it will not be presented in this work.

*"Our senses enable us to perceive
only a minute portion of the
outside world."*

Nikola Tesla

2 Organic Scintillation

Introduction

Luminescence is the property that certain materials have of emitting light. This light is known as cold light because its origin is different from incandescence, the thermal radiation emitted by a black body. Luminescence by a body is shorter in wavelength than that of a black body at the same temperature; luminescence is emitted towards the blue and UV end of the visible spectrum while the black-body radiation radiation is in the infrared. There are several mechanisms leading to luminescence in nature such as electroluminescence (diodes), the emission of light in response to a strong electric field or electric current; chemiluminescence is light production during a chemical reaction; thermoluminescence (used in dosimetry) and cryoluminescence, light emission by heating or cooling the material; triboluminescence is the production of light resulting from a mechanical action; radioluminescence corresponds to the emission of light generated by the interaction of nuclear radiation and matter, etc. Luminescence is present in gas or vapor phases, liquid, solid crystals (organic or inorganic), glassy or plastics. Some materials are luminescent in the three states; therefore absorption and emission is related more to intramolecular forces than to intermolecular ones.

In this work, we were interested to the photoluminescence, emission of light is the response to photons, most specifically to photons between 80 and 140keV, energies commonly used in X-rays for medical applications. Luminescence is a commonly used to test nuclear and X-rays and the mechanisms that create this kind of light are similar to those of radioluminescence. Light results from the different fundamental mechanisms, fluorescence and phosphorescence which will be described further on. Most of the mediums are photo or radioluminescent and we will define a *scintillator* to be a medium whose quantum light

yield, defined as ratio between the number of light emitting states and the total number of excited states, is above 90%; the nature of the scintillator can be organic or inorganic.

Inorganic scintillators are common in nuclear ray detection and in bolometers. They are crystals which may be doped to increased the radioresistance properties of the scintillator. Radiation is highly absorbed due to their density which varies between 3.5 and 8.5 g/cm³. Light emission is quite fast, ranging from some tens of nanoseconds up to the microsecond after being excited, compatible characteristic with the detection of events. Historically, the most common inorganic scintillators used for radiation detection are : Sodium Iodide activated with thallium [NaI(Tl)]; barium fluoride [BaF₂]; bismuth germanate [BGO]; doped gadolinium oxyorthosilicate [GSO:Ce] and the lutetium yttrium silicate activated with cerium [LYSO(Ce)]. The quantum yield of inorganic scintillator is below 15%, nevertheless due to their density, the light output is considered high and it is of around 40000 photons per absorbed MeV.

As inorganic scintillators, organic scintillators are common in nuclear detection. They are mainly aromatic compounds which can be solid (anthracene), liquid (benzene, xylene), as well as diluted in liquid solvents (alkanes) or solids such as glass or organic matter (optical fibers doped with p-terphenyl). The application of organic scintillators go beyond nuclear detection and bolometry. They can be used in optical detection and industry (medical imaging). Thanks to their tissue equivalent density (1 - 1.4 g/cm³) no correction is needed when used in medical imaging and therapy. Despite their expected low resistance to radiation, organic scintillators are radioresistant and show less damage as predicted by theory. The most common organic scintillators are: anthracene and benzene; p-terphenyl, oxazoles and oxadiazoles (see table 2.1). Light emission generally occurs between 1 and 3 ns after excitation except for anthracene which is slower. Their quantum yield are very high, that of anthracene, reaching sometimes 100%. On the other hand, light output is quite low when compared to inorganic scintillators due to their low density and it is of around 10000 photons per absorbed MeV [22].

This work is based on the study of organic scintillators, more precisely anthracene and p-terphenyl. This choice was based on the fact that these two scintillators are widely used and because fiber optics for medical applications [23] may be doped with p-terphenyl.

Despite the type of scintillator, radio or photo luminescence is the result of the absorption of a certain amount of external energy deposited in the molecule in the medium by the incident radiation. The molecule is excited to a vibronic or superexcited state and then

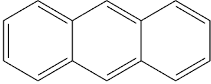
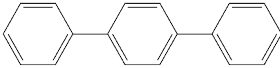
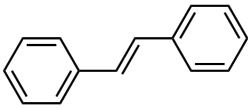
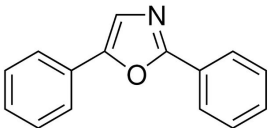
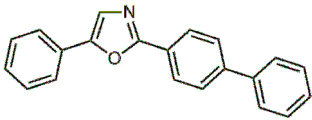
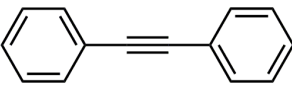
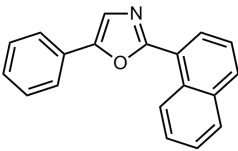
Organic Scintillator	Formula	Density (g/cm ³)	Chemical Structure
Anthracene	$C_{14}H_{10}$	1.28	
TP [p- Terphenyl]	$C_{18}H_{14}$	1.24	
trans-Stilbene	$C_{14}H_{12}$	0.97	
PPO .[2,5-dyphenyloxazole]	$C_{15}H_{11}NO$	1.06	
PBD .[2-Phenyl-5-(4-biphenyl)- 1,3,4-oxadiazole]	$C_{20}H_{14}N_2O$	1.10	
Diphenylacetylene	$C_{26}H_{20}$	0.99	
α -NPO .[2-(1-Naphthyl)- 5-phenyloxazole]	$C_{19}H_{13}N_2O$	0.99	

Table 2.1 – Some of the most popular organic scintillators proposed by Brooks [21].

relaxes through radiation or radiationless processes. There are two different paths that lead to molecular relaxation: internal conversion, where the molecule undergo transitions leading to lower energetic vibronic states finally reaching the ground state; autoionization, the ejection of a geminate electron resulting in the creation of a thermalized e-h pair where the electron is found in the conduction band of the material and the low mobility hole, in its valence band. The response to these two different relaxation paths is different generating

two different kind of emission of light: the first one known as prompt or fast emission (1-3 ns) results from internal conversion processes; the second one known as delayed emission (100 ns) is generated through geminate recombination after mutual slow diffusion under the effect of the mutual Coulomb field. When the organic scintillator is diluted in a non-scintillating solvent, it is this last one that statically has more probability to be excited to a higher, therefore scintillation is generated by the transfer of energy or charges to the scintillating molecules.

The fundamental aspects of organic scintillators in a pure medium needed for the interpretation of the experimental results obtained during this work is presented in this chapter. At first, the primary excitation mechanisms by incident radiation leading to excited molecular states is introduced. Next, the de-excitation transitions leading to ionization are described. In a third part, the relaxation mechanisms are presented with a special focus on the pair of spins which is a basic parameter in scintillation. After, the kinetic theory and temporal decay laws of fluorescence emission are presented. This chapter will end with a theory review of the relation between dose and luminescence where the models of Birks and Voltz are presented.

2.1 The Primary Processes

The primary process are considered to be all the initial transitions produced by the absorption of the energy in the medium. The incident radiation transfers energy along its path where excited, superexcited¹, ionized molecules and excitons are produced. The ionization of molecules leads to the creation of free electrons known as secondary electrons or δ rays[26]. Secondary electrons with enough kinetic energy may ionize other molecules in the medium generating more free electrons. Any electrons generated at this stage are known as secondary electrons as well.

The production of excitons is related to the density of the medium and to excitation energies over the ionization potential I_G . The electronic mobility is low in insulators due to the intermolecular structure. Consequently the probability for an electron to escape decreases, therefore the probability of creating an exciton increases. The electron remains bounded to its 'parent' molecule by the Coulomb interaction creating an electron(e)-hole(h) pair[27].

¹A superexcited state is a neutral excited state where the molecule has received enough energy to be over its ionization threshold, I_p . Hence, as the electron is coupled with the ionization energy continuum. For fast electrons interacting with solid or liquid organic scintillators, Platzman[24] proposed the creation of plasmons the very rapidly would decay superexcited states. Plasmons are considered as quasiparticles produced by the vibration of valence electrons in dense material with a lifetime of approximately some femtoseconds[25].

Nonetheless, excitons may be produced by excitation energies below the I_G ; two molecules excited below this potential may interact and also create an exciton as explained by Klein[28].

The basic primary processes are here summarized:

- $M + E \rightarrow M^*$: Molecular excitation
- $M + E \rightarrow M^{**}$: Molecular superexcitation
- $M + E \rightarrow M^+ + e^-$: Direct ionization
- $M + E \rightarrow (M^+, e^-)$: Exciton (geminate pair)

Activation Regions

Activation is defined as the deposit of energy by incident radiation. The volume and geometry of the activation regions depend on the nature of the incident radiation.

Heavy particles such as α particles and protons create a high density activation region along the particle trajectory creating a track spatially defined by a cylinder or radius r_0 as observed in figure (2.1). Secondary electrons with enough kinetic energy leave the track and may originate smaller regions of high density of activated molecules. These regions are called *spurs* or *blobs* depending on their geometry[29].

As opposed to heavy particles, photons and fast electrons among others, do not create a high activation cylindrical region along their paths. These light particles have a lower interaction probability with the medium and they transfer their energy to fewer particles. Consequently, smaller blobs and spurs may be produced along their trajectory. High activation areas may be produced by secondary electrons as well, but once again, these regions are significantly smaller than those generated by heavy particles[30].

2.2 Evolution of the Primary Processes

After the incident radiation has deposited its energy within the scintillator, the evolution of the states depend on the region where there are located.

In low density activation regions, the probability of interaction among molecules is low. Hence, excited molecules keep their spin parity and deexcite through internal conversion or

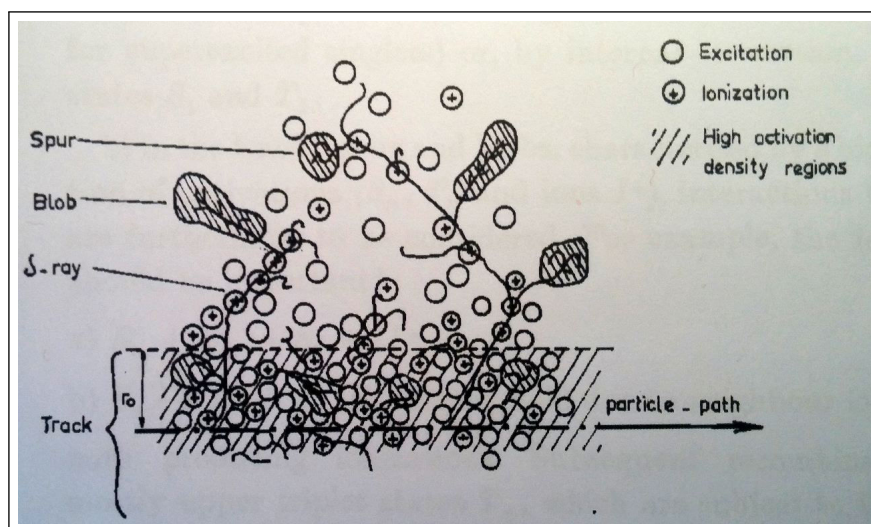


Figure 2.1 – Schema of the distribution of different high activation regions caused by a high energy heavy particle - *from: G.Laustriat, "Thermoluminescence decay of organic scintillators," Molecular Crystals, vol.4, no. 1-4, pp. 127-145, 1968.*

vibrational relaxation leading to the first excited electronic state S_1 . Superexcited molecules not only may undergo the same transitions to decay to the S_1 state as the excited molecules, but they may autoionize as well. The superexcited molecule dissipates its energy in the medium decaying to a thermalized e-h pair. This geminate pair may undergo geminate recombination to relax to S_1 electronic level; or if they electron and the parent molecule dissociate, a free electron is produced[31]. The probability $P(r)$ the electron escapes recombination is described by Onsager's theory[32] and it is:

$$P(r) \propto e^{-\frac{r_c}{r}}, \quad (2.1)$$

where r_c , the Onsager's critical radius, corresponds to the distance where the potential energy of the e-h equals the thermal Boltzmann energy of the system, $k_B T$:

$$r_c = \frac{q^2}{4\pi\epsilon_0\epsilon_r k_B T}, \quad (2.2)$$

where ϵ_0 and ϵ_r are the vacuum permittivity and the relative static permittivity respectively, and q , the charge of the electron.

The different mechanisms above described are shown in figure ??.

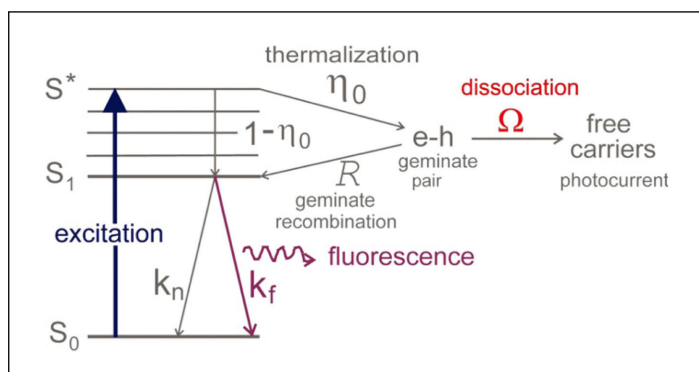


Figure 2.2 – Decay of a molecule in the superexcited state. The pair may dissociate or end up on the S_0 ground state. The constants - *from*: Falkowski et al., "Sano–Tachiya–Noolandi–Hong versus Onsager modelling of charge photogeneration in organic solids," Chemical Physics, vol.392, no. 1, pp. 122-129, 2012.

In high density zones, excited molecules undergo the different process in comparison to those occurring at low density zones. Nonetheless, as the concentration of excited molecule is higher, interaction among excited molecules is much more probable due to the electric fields created by the excited electrons therefore. These interactions increase the probability of autoionization[30].

During e-h recombination, triplet molecular states are created caused by the interaction between the nuclear magnetic moment μ and excited electron. Electron exchange leads to the creation of such triplet states as well. There is a spin-spin interaction between two electrons described by J , the exchange coupling constant. In fact, the Coulomb interaction between two electrons lift the degeneracy among states with different total spins making the triplet states accessible. As previously mentioned, the triplet-singlet ratio is of 3:1, so in these high density zones, triplet-state decay play an important role.

2.3 Evolution of the lowest energy states

Kasha's rule[33] describes how the molecule decays from the singlet and triplet states S_1 and T_1 to the ground state S_0 . All of the transitions are radiationless² except for two: fluorescence and phosphorescence. The difference between these transitions is their lifetime; the lifetime of phosphorescence may last hundreds or thousands of times more than the lifetime of fluorescence. Table 2.2 contains a list of all the different possible processes a molecule in the S_1 or T_1 level can undergo.

²Energy may be dissipated as heat, though it is neglected when compared to energy gap between different electronic levels.

Process	Transition	Rate Constant
Fluorescence	$S_1 \rightarrow S_0 + h\nu_s$	k_s
Intersystem crossing	$S_1 \rightarrow T_1$	k'_s
Non-radiative relaxation quenching	$S_1 \rightarrow S_0$	k''_s
Non-radiative mutual relaxation quenching	$S_1 + S_0 \rightarrow S_0 + S_0$	k_{ss}
Non-radiative external relaxation quenching	$S_1 + Q \rightarrow S_0 + Q$	k_{sq}
Phosphorescence	$T_1 \rightarrow S_0 + h\nu_T$	k_t
Non-radiative relaxation quenching	$T_1 \rightarrow S_0$	k'_t
Non-radiative external relaxation quenching	$T_1 + Q \rightarrow S_0 + Q$	k_{tq}
Triplet-Triplet annihilation	$T_1 + T_1 \rightarrow S_1 + S_0$	k_{tt}
	$T_1 + T_1 \rightarrow T_1 + S_0$	k'_{tt}
	$T_1 + T_1 \rightarrow Q + S_0$	k''_{tt}

Table 2.2 – Different processes that lead to the ground state from the excited singlet and triplet states S_1 and T_1 . The sum of the possible deexcitation pathways determine the total deexcitation constant k .

Table 2.3 summarizes the main processes taking place from energy absorption to radiative emission within an organic scintillator. All processes taking place before around 10 ps can be considered to occur immediately after the incident energy deposits its energy exciting and ionizing the molecules. This is due to the existing limits in nowadays electronics. The electronic time resolution of the experimental setup used in this work was of 1 ns which was more than enough to acquire and measure lifetimes of 3 ns, the shortest lifetime of one of the scintillators used.

The Jablonski diagram in figure 2.3 depicts different electronic and vibrational levels in a molecule and possible transitions occurring during molecular excitation and deexcitation. All transitions are radiationless except for the $S_1 \rightarrow S_0$ where the molecule may scintillate. Transitions between vibrational levels belonging to different electronic states are described by the Franck-Codon principle. Energy absorption transitions between electronic levels are extremely fast compared to nuclear motion. This is explained because of the great mass difference between the nucleus and electron. It may be considered the molecular structure remained static during energy absorption. On the other hand, S_1 excited states make take as long as some ns to decay, which allows the molecule to reorganize before light emission[34].

2.3. Evolution of the lowest energy states

Process	Time Scale (s)
Absorption	10^{-16}
Lifetime of single excited states (except for S_1)	$10^{-16} - 10^{-15}$
Direct Ionization	$10^{-16} - 10^{-15}$
Autoionization	$10^{-14} - 10^{-13}$
Excitons and e-h creation	$10^{-14} - 10^{-13}$
Electron thermalization	10^{-14}
Molecular vibrational relaxation	$10^{-13} - 10^{-11}$
Internal conversion	$10^{-11} - 10^{-9}$
Radiationless intercombination transitions or intersystem crossing	$10^{-10} - 10^{-8}$
Fluorescence decay	$10^{-9} - 10^{-7}$
Phosphorescence decay	$10^{-6} - 1$

Table 2.3 – Characteristic times of different processes starting from energy absorption by the organic scintillator to the relaxation by light emission.

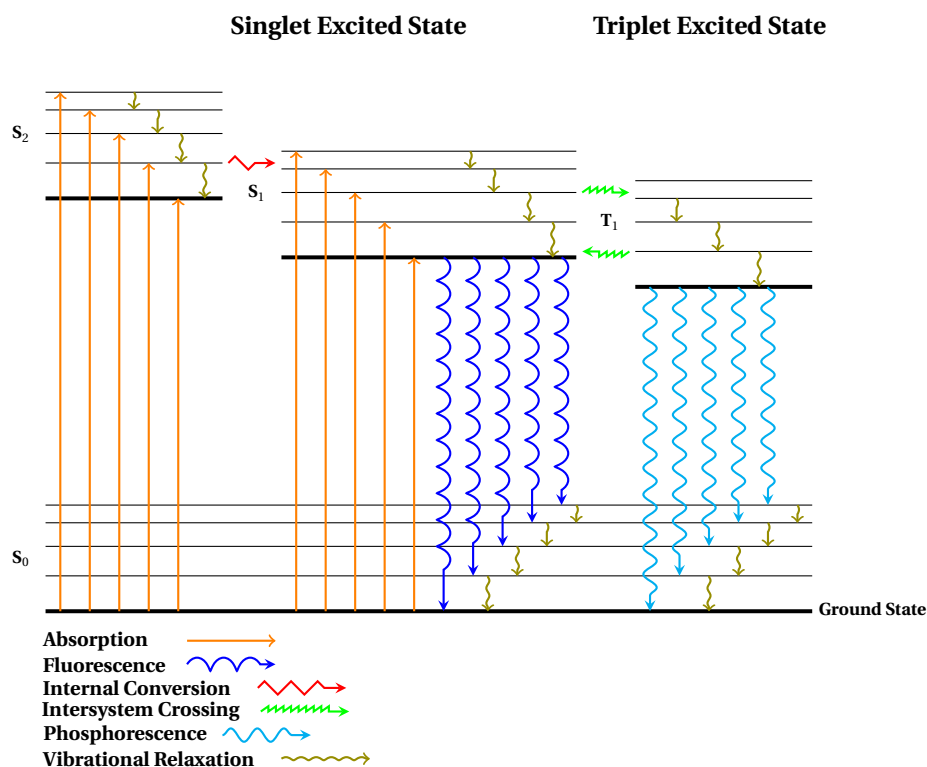


Figure 2.3 – The Jablonski Diagram: Most important excitation and de-excitation transitions in an organic scintillator.

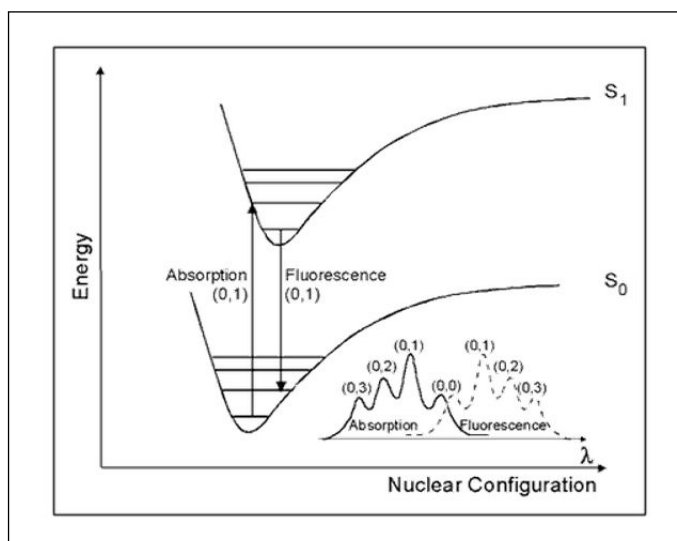


Figure 2.4 – Franck-Condon Principle and Stokes' shift

This reorganization of the molecular and electronic structure is responsible that the energies of absorption and emission are not the same. Generally the energy of emission is lower than the energy of absorption. This shift is known as the *Stokes' shift*. This explains why the molecule is transparent to its own emission. Image 2.4 shows the the absorption energy is higher than the emission which corresponds to the Franck-Condon principle. On the lower right corner, it can be observed the shift in wavelength between the absorption and emission spectra which corresponds to the Stokes' shift .

2.4 The Light Emission

The depletion of the first singlet excited electronic state to the ground state generates a radiative transition known as fluorescence³. The total intensity of light emitted by the organic scintillator has its origin on this transition and it is composed of two different components[35], the *prompt* and *delayed* components. The origin of these components depends on the molecular transitions that lead to the S_1 singlet electronic level.

Excited molecules in the singlet state are responsible for the prompt component. The origin of the delayed component of fluorescence was at first considered to be produced by e-h pairs in the triplet state. Later, it was proved that the delayed component originates through triplet-triplet annihilation[36, 37].

³Phosphorescence is emitted by the same transition though it takes place several orders of magnitude later than fluorescence. This transition is of no interest for this research so no further discussion will be here presented.

Intersystem crossing transitions are most likely to occur in high density activation regions, regions that are mainly created in the organic scintillator by heavy charged particles irradiation. Another approach to origin of the delayed component is through the ion recombination mechanisms[38]. Both approaches are presented in the following pages.

Let us now define $i_T(t)$ as the fluorescence observable considering the intensity of prompt (I_p) and delayed (I_d) components of fluorescence:

$$i_T(t) = i_p(t) + i_d(t). \quad (2.3)$$

2.4.1 The prompt component

In order to determine the intensity of the prompt component, the evolution of C_s , the local concentration of molecules on the S_1 has to be established. It is given by the following kinetic equation:

$$\frac{d}{dt} C_s = D_s \Delta C_s - \frac{1}{\tau_s} C_s, \quad (2.4)$$

where D_s the diffusion coefficient and τ_s is the fluorescence lifetime defined as the reciprocal of the sum of all the deexcitation rates that give rise to fluorescence defined by:

$$\frac{1}{\tau_s} = k_s + k'_s + k''_s. \quad (2.5)$$

Let us define $N_s(0)$ as the number of excited molecules right after the excitation produced by primary or secondary particles. After integrating equation 2.4 over the whole space and between 0 and an instant t , the number of excited particles after at instant t after excitation is:

$$N_s(t) = N_s(0) \exp(-t/\tau_s). \quad (2.6)$$

Based on the previous relations, the intensity of the prompt emission is found to decay

exponentially is equal to:

$$i_p(t) = k_s N_s(0) e^{(-t/\tau_s)}, \quad (2.7)$$

and the total intensity of light emitted defined within the interval $[0, t_0]$ is given by:

$$L_p(0, t_0) = \eta_s N_s(0) [1 - e^{(-t_0/\tau_s)}], \quad (2.8)$$

where η_s is the quantum fluorescence yield written $\eta_s = k_s \tau_s$ [39]. Finally, the total intensity of light due to the prompt emission is expressed as:

$$L_p = L(0, \infty) = \eta_s N_s(0). \quad (2.9)$$

2.4.2 The Delayed Component

Historically, the origin of the slow component was first described by the triplet-triplet interaction (table 2.2) and then by ion recombination.

2.4.2.1 The Triplet-Triplet Annihilation

The singlet excited electronic levels S_1 responsible for the delayed component of fluorescence is generated through triplet-triplet annihilation[40]. These molecules in the triplet state are generated in high density activation zones that are created by heavy ionizing particles or by secondary particles. The delay intensity emission is therefore related to the creation and evolution of these triplet states and it is given by:

$$i_d(t) = k_s N'_s(t) = k_s \int_0^R dx \int_0^\infty C'_s(r, t) 2\pi r dr. \quad (2.10)$$

At $t = 0$, both the local concentration of triplet states $C'_s(r, t)$ and $i_d(t)$ are equal to 0. Using the previous equation and the kinetic relationship given 2.4, the intensity of the delayed

emission is then written as:

$$\frac{dI_d}{dt} + \frac{1}{\tau_s} I_d = f(t), \quad (2.11)$$

where function $f(t)$ is determined by the evolution in time of the triplet states. Let us define $C_T(r, t)$ as the local concentration of triplet states at an instant t and at a distance r from the track. The evolution of the local concentration of triplet states is described by the kinetic equation below:

$$\frac{\partial}{\partial t} C_T(r, t) = D_T \Delta C_T(r, t) - \frac{1}{\tau_T} C_T(r, t) - \chi_{tt} C_T^2(r, t), \quad (2.12)$$

where χ_{tt} is the sum of the triplet-triple annihilation constant rates expressed as:

$$\chi_{tt} = 2K_{tt} + k'_{tt} + 2k'_{t't}. \quad (2.13)$$

Considering and solving equations 2.12 and 2.11, the intensity for the delayed component is given by:

$$i_d(t) = 2\pi \frac{\eta_s}{\tau_s} k_{TT} \int_0^L dL \int_0^t \exp\left(-\frac{t-\alpha}{\tau_s}\right) d\alpha \int_0^\infty C_T^2(r, \alpha) r dr, \quad (2.14)$$

where L is the particle range and

Equation 2.14 can be written in a much simpler form shown in equation 2.15 for times⁴ $t \gg \tau_s$. A and N are constants to be chosen depending on the type of organic scintillator and t_α is a relaxation time is given by 2.16:

$$i_d(t) \simeq \eta_s \frac{N}{[1 + A \ln(t + t/t_\alpha)]^2 (1 + t/t_\alpha)}, \quad (2.15)$$

and,

⁴By then, the prompt emission has totally decayed.

$$t_\alpha = \frac{r_0^2}{4D_T}, \quad (2.16)$$

where D_T is the diffusion coefficient of the triplet state.

This leads to obtain the total delayed intensity, L_d :

$$L_d = L_d(0, \infty) = \eta_s \frac{k_{tt}}{\chi_{tt}} N_T(0). \quad (2.17)$$

The chemical nature of the organic scintillator changes the response and characteristics of the delayed intensity, therefore an adjustment of the previous relations is needed in order to explain the new system[29, 30]. They are not here presented as they do not correspond to the subject of research of this work.

2.4.2.2 Fluorescence by Ion Recombination

A second approach to the origin of the delayed component of fluorescence in dense materials is through the evolution of the electron-hole(e-h) pair. In order to describe the evolution, let us introduce a distribution function $n(r, t)$ to determine the probability density of r , the distance between the e-h pair at a given time t .

The time evolution of the e-h pair depends on the relative diffusion between the hole and the electron in the presence of their mutual Coulomb field and by the recombination probability function by unit of time, $\lambda(r)$. The kinetic equation describing this phenomenon is characterized by the Debye-Smoluchowski equation[41, 42]:

$$\frac{\partial}{\partial t} n(r, t) = D_{e,h} \Gamma_r n(r, t) - \lambda(r) n(r, t) + n_0(r) \delta(t), \quad (2.18)$$

where $D_{e,h}$ is the sum of the electron diffusion coefficient D_e and the hole diffusion coefficient D_h ($D_{e,h} = D_e + D_h$), $n_0(r)$ is the initial e-h pair distribution at the end of thermalization, and $\Gamma_r(r, t)$ describes the differential operator of transport:

$$\Gamma_r = \frac{\partial^2}{\partial r^2} + \left(\frac{2}{r} + \frac{r_c}{r^2} \right) \frac{\partial}{\partial r}, \quad (2.19)$$

where r_c is given by equation 2.1, and $\lambda(r)$ is:

$$\lambda(r) = \frac{1}{\tau_0} \exp\left(\frac{-r}{r_0}\right), \quad (2.20)$$

where r_0 is a certain recombination distance associated to τ_0 , its recombination rate. At short distances, the function $\lambda(r)$ shows that the recombination yield is high.

The first term in equation 2.18 describes the relative diffusion of the e-h pairs under the influence of the Coulomb force; the second term corresponds to the probability of recombination of an e-h pair separated by a distance r at a rate $\lambda(r)^{-1}$; the last term as it depends on a δ function defined at 0, so at any other values this function is equal to 0.

Let us now define the electron-hole survival probability $P(t)$ defined by :

$$P(t) = 4\pi \int_x^\infty r^2 \lambda(r) n(r, t) dr, \quad (2.21)$$

and the delayed recombination velocity $R(t)$:

$$R(t) = 4\pi \int_x^\infty r^2 \lambda(r) n(r, t) dr, \quad (2.22)$$

where x is the minimal distance between two neighboring pairs in the medium.

Based on equation 2.18, two different kinetic recombination transitions may be observed:

- *The static mode:* In this mode it is considered that the recombination of the geminate pair takes place faster than the unit of time defined by $\lambda(r)$. It is referred as recombination by tunnel effect.
- *Diffusion Mode:* This mode is governed by the diffusion of the e-h pairs and occurs at long times.

The Static Mode In this mode, equation 2.18 is defined by the following relationship:

$$\frac{\partial}{\partial t} n(r, t) = -\lambda(r)n(r, t), \quad (2.23)$$

and $n(r, t)$ can be written as:

$$n(r, t) = n_0(r)e^{-\lambda(r)t}. \quad (2.24)$$

This leads to a description of $R(t)$ as follows:

$$R(t) = 4\pi \int_x^\infty r^2 \lambda(r) n_0(r) e^{-\lambda(r)t} dr, \quad (2.25)$$

and considering the definitions of $\lambda(r)$ and $P(t)$, $R(t)$ becomes:

$$R(t) \propto t^{-(\alpha+1)}, \quad (2.26)$$

where $\alpha = r_0/b$, b corresponding to the electron thermalization distance.

Diffusion Mode

This mode depends on all the terms in equation 2.18. Based on [41], the solution for $R(t)$ at a given excitation energy:

$$R(t) = \left(\frac{r_c^2}{4\pi D_{e,h}} \right) t^{-3/2} Q_{e,h} \quad (2.27)$$

where $Q_{e,h}$ is the recombination yield of the e-h pair. This process is more frequent for ionic liquids under VUV excitation. Studies have widely proven that this process is valid for low density mediums and for long times.

$$Q_{e,h} = 4\pi \int_x^\infty n_0(r) e^{\left(\frac{-r}{r_c}\right)} dr \quad (2.28)$$

Multiple Interactions

Equation 2.18 needs to be adjusted to describe high density zones of ionization. An extra term is added to describe the annihilation between different e-h pairs at $t = 0$. This term is composed of $c(t)$, the sum of the concentration of positive and negative particles and k , a constant proportional to the density of excited molecules in a region. Indeed, k is maximum in high density areas such as tracks and spurs.

$$\frac{\partial}{\partial t} n(r, t) = D_{e,h} \Gamma_r n(r, t) - \lambda(r) n(r, t) - 2k c(t) n(r, t) + n_0(r) \delta(t). \quad (2.29)$$

The solution of the distribution function $n(r, t)$ is found by solving the following equation of motion of pairs:

$$\frac{\partial}{\partial t} n(r, t) = -[\lambda(r) + 2k c(t)] n(r, t), \quad (2.30)$$

and

$$n(r, t) = n_0(r) \exp[-\lambda(r)t] \exp\left[-2k \int_0^t c(\theta) d\theta\right] \quad (2.31)$$

Let us now assume that the the function $c(t)$ varies proportional to the concentration of the excited molecules:

$$c(t) = \frac{c_0}{1 + 2k c_0 t}, \quad (2.32)$$

where c_0 is the initial concentration of excited molecules.

Writing equations 2.30 and 2.31 taking into account $c(t)$ leads to:

$$n(r, t) = n_0(r) \exp[-\lambda(r)t] (1 + 2k c_0 t)^{-1}. \quad (2.33)$$

Finally the recombination velocity is found to be:

$$R(t) = \frac{1}{1 + 2k c_0 t} 4\pi \int_0^\infty r^2 \lambda(r) n_0(r) \exp[-\lambda(r)t] dr \quad (2.34)$$

Once again, considering $\lambda(r)$ and $P(t)$, $R(t)$ is written:

$$R(t) \propto \frac{1}{1 + 2k c_0 t} t^{-(\alpha+1)}, \quad (2.35)$$

and as multi pair recombinations are the prevailing processes in high density zones, c_0 is assumed to be large over longer times (considered to be $2k c_0 t \gg 1$), hence $R(t)$ becomes:

$$R(t) \propto \frac{1}{2k c_0} t^{-(\alpha+2)}. \quad (2.36)$$

It has been observed that the density of excited molecules and the diffusivity of the medium play a role in determining the recombination velocity $R(t)$. All three of them are described by a power law t^{-n} where n is the variable to be chosen according to the type of recombination.

2.4.3 The Total Intensity

The prompt and delayed components of the fluorescence decay curve as well as the total decay profile ($i_T(t)$ describe by the relationship 2.3) can be observed in 2.5 for a sample of p-Terphenyl under X-rays irradiation.

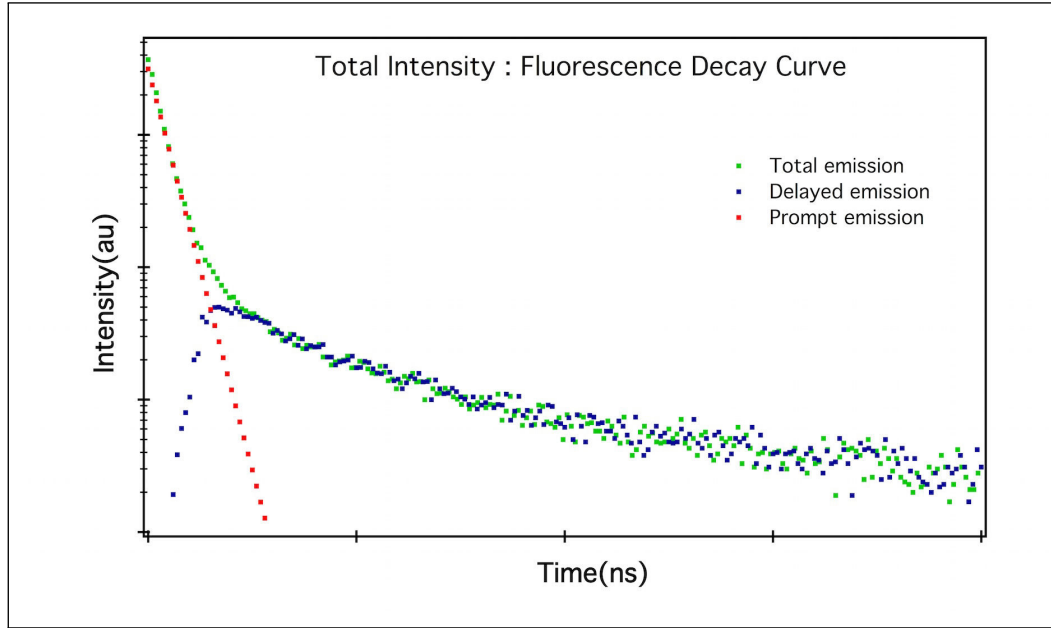


Figure 2.5 – The total emission (in green) is the sum of the prompt emission $i_p(t)$ (in blue) and the delayed emission $i_d(t)$ (in red). The decay curve was obtained by when irradiating a solid crystal of pure p-Terphenyl with X-rays

2.5 Dose and Luminescence

2.5.1 Organic Scintillators in Dosimetry

The idea of using organic scintillators in dosimetry was developed back in the 60's [43]. It presented the advantage of having density similar to that of water, the standard material used in medical dosimetry to mimic human tissue. Another advantage is that the emitted light is proportional to the absorbed energy for dE/dx below $50 \text{ MeV } c m^2/g$ [44]. Other publications agree on a linearity between light and dose from 100keV and above[45]. There are less studies for excitation energies below 100keV and results differ on the linearity which may be troublesome in low energy photon applications such as the brachytherapy. Nevertheless, some linearity has been observed for electron excitation between 20 and 250keV [46] while a nonlinearity response was observed for anthracene irradiated by photons with energies between 6 and 30keV [47]. At lower energies, the ionization processes - Temperature studies revealed no dependance between emitted light and temperature between 0 and 50°C with differences of less than 0.5% in the results [48]. In general, no temperature dependence is considered to exist when organic scintillators are used in a medical environment. Damage of organic scintillators induced by radiation is defined as a decrease in the output of scintillation per unit of absorbed dose. According to [49, 48] light yield diminishes as more

energy is deposited within the scintillator causing a decrease of around 5% for some kGy dose. Anthracene becomes yellowish and even dark with a high absorbed dose and not only its light yield decreases faster for small total doses, but also it depends on the rate the energy is delivered; the slower the rate, the damaged to the crystal increases[50]. Even if the light output yield changes, the fluorescence decay shape remains unchanged [51].

Finally, real-time dose monitoring and smaller detection volumes make of these detectors a very interesting and promising solution to be taken into account in medical dosimetry.

2.5.2 The Cavity Theory

The cavity theory defines the relationship between a radiation dose deposited inside a cavity and the energy absorbed by the surrounding medium [52].

For first time in the year 1912, Bragg proposed the possibility of measuring the electron fluence in a medium by associating it to the amount of ionization in a small volume of air contained within the same medium. He suggested the electron fluence caused under photon irradiation could be determined by multiplying the the number of electrons emitted per unit volume and their ranges; this product would be proportional to the ionization inside the small air volume. The cavity had to be sufficiently small to avoid the interaction of the ejected electrons within the cavity with the medium.

In 1929, Gray imagined a medium big enough it would attain electronic equilibrium under constant photon irradiation and then to place a very small cavity filled with gas within the equilibrium region. He proved that if the cavity was small enough, any scattering inside the cavity could be neglected. Considering that the same number of electrons pass through both materials, the ratio between the loss of energy per unit of volume in the medium and the gas would be the same as the ratio between the mass stopping powers for the electron in the medium and the gas $((S/\rho)_m$ and $(S/\rho)_g$). He assumed as well that the energy lost by the electrons was the same as the absorbed energy in the medium due to the idea that electrons lost their energy at a steady rate in the medium. Hence, the dose in the medium, D_m could be written as:

$$D_m = S_{mg} D_g, \quad (2.37)$$

where D_g is the dose in the gas and S_{mg} is equal to:

$$S_{mg} = \frac{(S/\rho)_m}{(S/\rho)_g}, \quad (2.38)$$

and:

$$D_g = J_g \frac{W}{e}, \quad (2.39)$$

where J_g is the charge per unit of mass produced by the ionized electrons and W/e is the average energy to produce an ion- electron pair in the gas[53].

In order to determine the dose, secondary electrons were not included in the calculations of the dose, which meant that precision of the dose was inversely proportional to the volume of the cavity and should he also assumed that the stopping power ratio did not depend on the energy of the incident radiation and that electrons lost energy steadily when crossing the medium.

Laurence then adapted Bragg-Gray formulas to take account of the dependance on energy of the mass stopping power ratio. The differential fluence or energy distribution Φ_T was derived:

$$\Phi_T dT = (dS/dV) \frac{dT}{(dT/dx)}, \quad (2.40)$$

This relationship gives the distribution of electrons per unit of volume per energy. The first term to the right of 2.40 represents the number of electrons with kinetic energy T_0 emitted per unit of volume and steadily stopped and the second term is known as the differential track length.

Laurence assumptions included monoenergetic electrons[54] generated by the medium of energy T_0 , neglecting Bremsstrahlung and electronic equilibrium. This led to D_g and D_m to be :

$$D_d = \frac{dS}{dV} \int_0^{T_0} \frac{1}{(dT/dx)_d} \left(\frac{dS}{\rho} \right)_g dT, \quad (2.41)$$

and

$$D_m = \frac{dS}{dV} \int_0^{T_0} \frac{1}{(dT/dx)_m} \left(\frac{dS}{\rho} \right)_m dT, \quad (2.42)$$

$$\frac{D_p}{D_m} = \frac{1}{T_0} \int_0^{T_0} \frac{(S/\rho)_d}{(S/\rho)_m} dT = \overline{(S/\rho)_m^d}, \quad (2.43)$$

where the last term is the weighed mean of mass stopping ratio $(S/\rho)_m^d$.

Laurence approach took into account the δ rays as the cavity size effect and introduced the mean energy notion for the first time. Nevertheless, it was still a model for small volumes and it was inaccurate for volumes where δ rays ionize at their turn.

Other cavities theories were developed to improve the existing theories. The mass stopping ratio used so far by a mass energy dissipation ratio acknowledge the fact electrons not necessarily follow straight paths in the cavity[55]. Burlin [56] proposed to replace the term S_{mg} in equation 2.37 by the ratio of the mass energy coefficients to estimate the dose for cavities larger than the range of secondary electrons, obtaining:

$$D_m = \left(\frac{\mu_{en}}{\rho} \right)_{m,g} D_g, \quad (2.44)$$

and the Burlin general cavity formula is:

$$D_g = [dS_{gm} + (1-d)(\mu_{en}/\rho)_{gm}]D_m \quad (2.45)$$

where d is a parameter given by:

$$(1-d) = (\beta L + e^{-\beta L} - 1)/\beta L, \quad (2.46)$$

where L is the volume of the cavity multiplied by a factor 4 divided by area defining the volume of the cavity and β is such that :

$$e^{-\beta L} = 0.01 \quad (2.47)$$

Equation 2.45 allows to estimate the dose regardless the volume of the cavity by using the parameter d . This parameter increased from 0 and 1 as the volume of the cavity decreases. Hence, dose could be measured considering both electrons and photons contribution in the dose.

Other more complete cavity theories were developed. For example, Kearsley theory added the electrons created by secondary electrons in its formulas just to mention one of many others who have taken into account many parameters to improve the Cavity theory.

2.5.3 The Birks Scintillation Model

Birks [57] defined L to be the total light emitted by an organic scintillator when excited by a particle of energy E . The relationship between E and L is given by:

$$L = SE, \quad (2.48)$$

where S is the absolute scintillation efficiency. This relationship is valid for low energy electrons ($E < 1$ MeV) which generate very low density activation areas along their path. The differential form of equation 2.48 is written:

$$\frac{dL}{dx} = S \frac{dE}{dr}, \quad (2.49)$$

with dL/dr defined as the specific fluorescence and dE/dx the specific energy loss.

The specific energy loss defined by Birks changes depending on the type of incident particle and its energy. Birks proposed a relationship to take account of the variation of the specific fluorescence caused by the nature of the incident particle:

$$\frac{dL}{dr} = \frac{S(dE/dx)}{1 + kB(dE/dx)}, \quad (2.50)$$

where B is a constant and k is quenching parameter in unimolecular mediums. For fast electrons, the specify luminescence is described by 2.49 and for particles with high dE/dx, equation 2.50 is approximated by :

$$\frac{dL}{dr} = \frac{S}{kB}. \quad (2.51)$$

Equation 2.51 is constant meaning the existance of a linear relationship between L and r.

Birks relationship is a semi-empirical approach that needs to be constantly adapted to correctly determine dL/dr for different type of particles and energies.

2.5.4 The Voltz Model

In the Voltz model [58], the specific luminescence, dS/dx is defined as:

$$\frac{dS}{dx} = \frac{dL_p}{dx} + \frac{dL_d}{dx}, \quad (2.52)$$

where dL_p/dx corresponds to the specific luminescence of the prompt component and dL_d/dx to that of the delayed component.

Let us start by the specific luminescence of the prompt component in the case of incident electrons:

$$\frac{dL_p}{dx} = \frac{q_s}{W_s} \frac{dE}{dx} \exp\left(-B_s \frac{dE}{dx}\right), \quad (2.53)$$

where q_s is the quantum efficiency of fluorescence, W_s represents the energy deposited on the molecule, dE/dx , the stopping power, and B_s is the quenching parameter. After W_s is deposited in the molecule, the molecule undergoes a vibronic transition. This electron is ejected to a higher energy single state S_n . Let us recall as explained before that the molecule

can: i) Directly De-excite to S_1 , and then to the ground state S_0 , ii) electronic quenching by interacting with a neighboring molecule annihilating internal conversion and the light emission. This process is defined by an exponential function that depends on B_s and dE/dx and describes the quenching probability.

The delayed component is defined by the following relation:

$$\frac{dL_d}{dx} = q_s \alpha \frac{\Phi_t}{W_t} \frac{dE}{dX} \exp\left(-B_t \Phi \frac{dE}{dx}\right), \quad (2.54)$$

where Φ_t/W_t relates to the efficiency of formation of triplet states, B_t is the corresponding quenching parameter described for the delayed component, α is the number of S_1 states formed by triplet-triplet annihilation.

*"I think our chances are not
looking great today but the only
way to fail for me is just not to try. "*

Gary Kasparov

3 The Experiment

Introduction

The experimental study of the fluorescence emitted by an organic scintillator excited by a continuous source was based on the measurement of the total light emitted per unit of time. The experiment parameters were the nature of the incident radiation, its energy and flux back then. Later, the development of impulse light sources (synchrotron, linear accelerators and pulsed cyclotron) and faster electronics made possible time resolved studies.

Since the 60's, the most common technique to acquire a time resolved fluorescence decay is to feed the signal of a photomultiplier tube (PMT) to a preamplifier and then to an amplifier to adapt it to be finally fed to an oscilloscope. Once the electronic perturbation by averaging the instrument artifacts is determined, the acquired shape corresponds to the fluorescence decay curve resolved in time. As the temporal resolution of oscilloscopes improved up to the existing subnanosecond limit, so did the precision of the timing information of decay profile. This experimental technique is widely used for liquid scintillation and pulse shape discrimination. Artifacts have different origins: first, the PMT saturates when exposed to high intensities of light and as a result, a decrease of the total measured height of the fluorescence peak occurs. It is probable saturation occurs during the photon multiplication processes in one or several dynodes, and due to the high number of incident photons the response may no longer be linear. Under extremely high intensities, saturation may occur even at the photocathode. Regardless the origin of saturation, the measured fluorescence decay profile does not contain precise timing information, specially for short times when light intensities are maximal. Second, the decay peak widens because the response of the electronic chain after the PMT can not be instantaneous. Consequently, the measured lifetime values may

lose their accuracy. Last, the signal-to-noise ratio of the measured decay curve decreases for increasing light intensities. This technique does not seem to be most adequate for medical applications, though some instruments are already commercialized.

At the end of the 60's, our laboratory developed a technique to measure recombination fluorescence using a nanosecond time resolved coincidence method. Since, the technique known as the TCSPC (Time-Correlated Single Photon Counting) has continuously evolved to measure all type of fast light signals (spectroscopy, UV, laser, etc.). This technique is based on temporal coincidence based on two input signals: one electronic signal synchronized with the external excitation source and another electronic signal generated by a PMT counting single fluorescence photons. For the work, the TCSPC has been adapted to work with two photomultipliers in temporal coincidence allowing to measure the fluorescence decay profiles generated by continuous excitation sources as it is the case for X-rays used in medical applications. The fluorescence decay curves were reconstructed with very high precision, condition required for the fundamental study in this work. Moreover, signal-to-noise ratio increased and PMT saturation was avoided and background noise such as external electromagnetic perturbations and electronic artifacts could be reduced to a maximum.

In the first part of the chapter, the fluorescence observable as well as its relation to the instrument response function IRF is presented. Second, a description of the general principles of the TCSCP and its mathematical aspects are discussed. Finally, the components used to mount the experimental setup are presented including the excitation source, different scintillator among others.

3.1 The Fluorescence Observable

The fluorescence observable is $i_T(t)$ as detailed in the previous chapter and defined in equation 2.3. Ideally, in order to obtain the fluorescence observable, the scintillator should be excited by a δ -pulse at $t = 0$ to avoid any distortions. The excitation pulse has a certain width that disturbs the fluorescence observable. Let us define $I_R(t)$ as the convolution of the observable $I_T(t)$ and $P(t)$, the excitation pulse:

$$I_R(t) = P(t) * i_T(t) \quad (3.1)$$

The electronics of the system adds more distortion to the measurements. Consequently, the

measured decay profile $I_M(t)$ defined by equation 3.2 is given by the convolution between $I_R(t)$ and $Q(t)$, the response function of the detection system:

$$I_M(t) = I_R(t) * Q(t). \quad (3.2)$$

Replacing $I_R(t)$ by the definition giving in 3.1 in 3.2 leads to:

$$I_M(t) = P(t) * i_T(t) * Q(t). \quad (3.3)$$

As convolution is commutative, it is possible to rearrange the the terms in 3.3 to define the total distortion of the system $S(t)$ given by the convolution of $P(t)$ and $Q(t)$. $I_T(t)$ becomes:

$$I_M(t) = i_T(t) * S(t). \quad (3.4)$$

The measured fluorescence intensity decay may be written using the integral notation as follows :

$$I_M(t) = \int_0^t i_T(t') S(t)(t - t') dt' \quad (3.5)$$

Let us recall that the total intensity $i_T(t)$ is the sum of the prompt and delayed components (formula 2.3). Now $I_M(t)$ can be written as¹[59] :

$$\begin{aligned} I_M(t) &= i_T(t) * S(t) \\ &= [i_p(t) + i_d(t)] * S(t) \\ &= [i_p(t) * S(t)] + [i_d(t) * S(t)] \\ &= I_p(t) + I_d(t), \end{aligned} \quad (3.6)$$

where $I_p(t)$ and $I_d(t)$ correspond to the convolution of the prompt ($i_p(t)$) and delayed ($i_d(t)$) observables with the total distortion of the system $S(t)$:

¹The convolution mathematical operation satisfies the algebraic *distributive property*.

$$I_p(t) = i_p(t) * S(t), \quad (3.7)$$

$$I_d(t) = i_d(t) * S(t). \quad (3.8)$$

In this work, an X-ray source was used to excite the organic scintillator. The X-ray photon flux was reduced for experimental reasons detailed further in this chapter. Hence the pulse excitation function $P(t)$ defined in 3.1 can be considered to be a δ -pulse, and in consequence, the perturbation $S(t)$ is equal to $Q(t)$, the response function of the detection system.

When the lifetime of the scintillator is equivalent to the width of the excitation pulse and electronic response, a deconvolution on $I_M(t)$ is needed to find $i_T(t)$ [60]. The method used to get $i_T(t)$ from the observed data will be explained in chapter 4.

3.2 The Time-Correlated Single Photon Counting

The TCSPC allows to obtain a statistical reconstruction of the fluorescence decay curve of an organic scintillator. The method can be compared to a stopwatch that records the time lapse between a *start* pulse from now on known as START and a *stop* pulse from now on referred as STOP. The START signal is originated at the precise moment the scintillator is excited by external source of radiation and the STOP corresponds to the pulse generated by the detection of a single photon emitted by the scintillator. The time event is sent to a memory block proportional to the measured time. The experiment is repeated until obtaining a very high statistical data precision that at the same time increases the signal-to-noise ratio. After many cycles, the distribution of timed events correspond to the fluorescence decay curve (see 3.1).

In order to precisely reconstruct the fluorescence decay curve, the STOP signal to stop the clock must be generated by a single photon. The picture 3.3 shows the signal generated by the flux of single photons. The PMT output signal is directly fed to the oscilloscope and it can be observed that the impulses have the same height meaning that there are only single photons being recorded. If the count rate is higher, 'pile-up' occurs leading to an overestimation of the fast photons over those arriving just after; the rising time of one or two photons can be discriminated electronically. This directly modifies the distribution of events, hence the decay curve statistical reconstruction (figure 3.2). It is also important to measure less than one photon per START-NO STOP period defined as the given lapse of time

3.2. The Time-Correlated Single Photon Counting

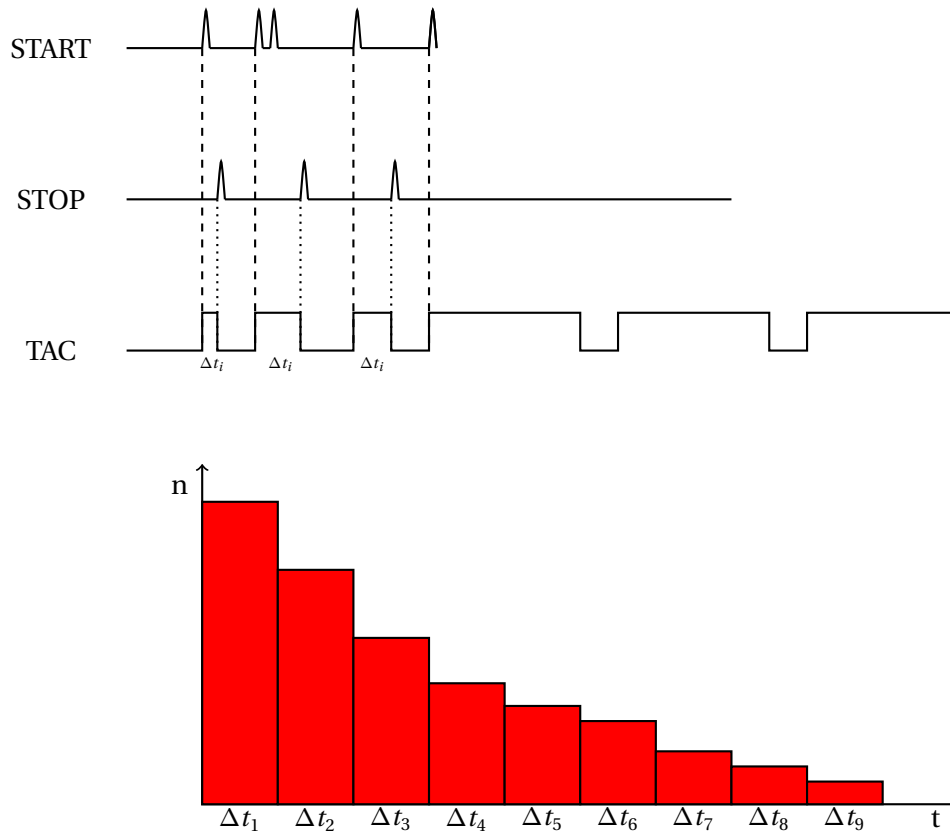


Figure 3.1 – Principle of time resolved measurement and histogram creation. The MCA records the time lapse between the START and STOP signals and assigns it to a given memory bin. Each time the value is measured again, the MCA adds a +1 count in the corresponding bin. As the cycle is repeated, the bin count increases and after many cycles, the profile of the decay curve is obtained.

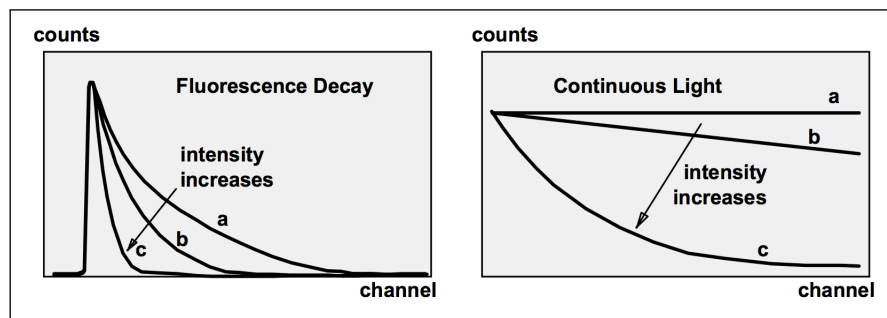


Figure 3.2 – Left : Decay curves a,b and c with no pile up . Right : Pile up distortion of a, b and c

to reset the electronics if no STOP signal is detected after a given START signal. The ideal single photon count should be between 0.1 and 0.01 per period[61]. Even if the scintillator

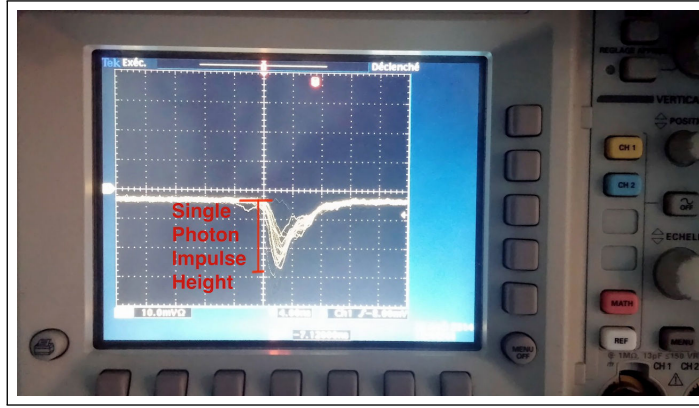


Figure 3.3 – Signal photon count signal as observed in an oscilloscope during experiment setup

emits a very low intensities of light, a diaphragm must be used to reduce the size of the STOP PMT window exposed the emitted light by the scintillator in order to avoid two or more photons arriving at the same time to the photocathode.

3.2.1 The Mathematics behind the TCSPC

The probability of detecting n photons in a given interval within an excitation cycle is described by a *Poisson Distribution* (see Appendix A). Let $t_i + \Delta t$ be the time interval assigned to the $i - th$ bin in the MCA and N , the average of photons detected. The probability $p_i(n)$ is written in the following form:

$$p_i(n) = \frac{N_i^n}{n!} e^{-N_i} \quad (3.9)$$

Now let us define the probabilities of detecting 0, 1 or more than one photons:

$$p_i(0) = e^{-N_i} \quad (3.10)$$

$$p_i(1) = N_i e^{-N_i} \quad (3.11)$$

$$p_i(n > 1) = 1 - p_i(0) - p_i(1) = 1 - (1 + N_i) e^{-N_i} \quad (3.12)$$

3.2. The Time-Correlated Single Photon Counting

The number of detected photons D_i in the $i - th$ channel after many START-STOP cycles C is :

$$D_i = C \left[p_i(1) + p_i(n > 1) \right] \quad (3.13)$$

Let us recall that the TCSPC is a technique that requires very low intensities of light with the purpose of only detecting one photon at a time in the STOP photomultiplier :

$$p_i(1) \approx N_i \quad (3.14)$$

$$p_i(n > 1) \approx N_i^2 \quad (3.15)$$

$$(3.16)$$

and equation 3.13 is now :

$$D_i \approx C \left(N_i + N_i^2 \right) \approx C N_i \approx N_i \quad (3.17)$$

Hence, the number of counts in a given memory bin is proportional to the to the intensity of light recorded in the time lapse defining the bin.

As only one photon is recorded by the TAC per cycle, the number of photons counted per channel per cycle is less than one. This count rate must be respected at all times not to statistically disturb the results. Else, one observes the *pile-up effect*. This probability distribution is defined by :

$$D_{si} = D_i \left(1 - \frac{1}{C} \sum_{j=1}^{i-1} D_j \right), \quad (3.18)$$

where D_{si} is the number of stocked photons in the memory bin i and D_j corresponds to the sum of all the other events stocked in all the different memory bins except bin i . Ideally, the sum should tend to 0 to have a 1:1 ratio between the detected number of photons D_i and the stored number of photons D_{si} . To achieve this condition, the value of C should increase as the N_j does not change. In other terms, in only 1% of the START-STOP cycles, a photon should be detected. Else, the value of the measured lifetime τ decreases[62]. It is of extreme

importance to be rigorous and precise to set the STOP detector to only detect single photons. Graph 3.4 shows the distortion of the fluorescence decay curve generated by not setting the STOP PMT in single photon counting mode

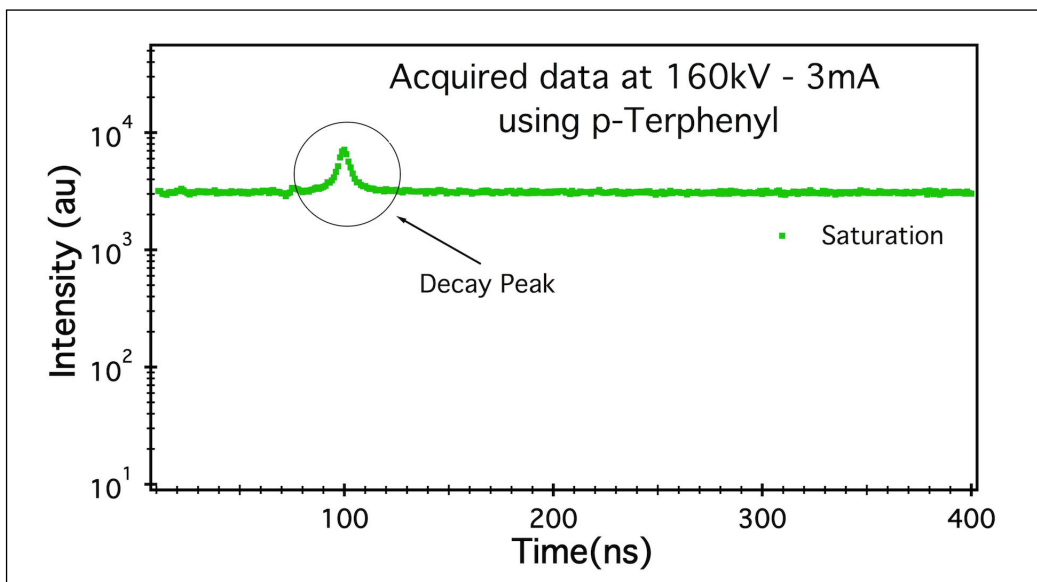


Figure 3.4 – No valid information is contained in this data set. The peak is believed to be a highly distorted and inaccurate fluorescence decay curve.

3.2.2 The Experimental Error

The TCSPC is a Poisson counting technique where the noise is described by the Poisson noise. The noise for each single registered data point is determined by the square root of the number of counts, this meaning that error decreases as the count increases. Accidental counting is another source of experimental error, though as explained further on, it can be limited by adjusting the experimental conditions correctly.

3.2.2.1 Counting Error

The standard error in Poisson counting is determined by the square root of the number of counts. Therefore, the error in the $i - th$ channel after N counts is given by:

$$\sigma_i = \sqrt{N_i}, \quad (3.19)$$

and the relative error is:

3.2. The Time-Correlated Single Photon Counting

$$\frac{\sigma_i}{N_i} \quad (3.20)$$

The relative scatter of the decreases as $1/\sqrt{N_i}$. For instance, the error on 10000 counts is equal to 1% error. If more precision is required, the number of counts should be simply increased.

The relative error between the interval $[a, b]$ is given by :

$$\frac{\sqrt{\sum_{a=i}^b N_i}}{\sum_{a=i}^b N_i}. \quad (3.21)$$

As expected, the error decreases when the area under the fluorescence decay curve between to points is estimated.

3.2.2.2 Accidental Coincidence

Only time-correlated events are registered in the MCA. Nevertheless, let us estimate the probability where two uncorrelated events are registered within the limits of the time resolution of the electronics. Let us define that time window as t_w and τ_1 and τ_2 and the counting rates per interval of detectors 1 and 2 [63, 64]. The total probability that uncorrelated events 1 and 2 occur within the time interval t_w is:

$$P_a = (\tau_1 t_w)(\tau_2 t_w). \quad (3.22)$$

Let us identify the START PMT to detector 1 and the STOP PMT to detector 2 to match the experimental conditions in this work. The probability to detect one photon in detector 1 is $\tau_1 t_w = 1$. This is always true because the START PMT was used to start a new timing window so it must always detect a photon. The probability to detect a photon in the PMT STOP is $\tau_2 t_w \ll 1$ due to the need to have very low count rates. Therefore, the accidental coincidence is only determined by the count rate of the STOP PMT.

According to 3.22, the general relationship of rate of accidental counts τ_{12} per cycle is:

$$\tau_{12} = \tau_1 \tau_2 t_w, \quad (3.23)$$

and for the TCSPC, t_{12} is:

$$\tau_{12} = \tau_2 t_w. \quad (3.24)$$

In order to avoid accidental coincidence counting, the count rate of the PMT STOP must be as small as possible as well as to avoid pile-up.

3.3 The Experimental Setup

The following components were used in order to mount the TCSPC experiment:

- 1 photomultiplier tube (PMT) Photonis XP2020
- 1 photomultiplier tube (PMT) Hammamatsu R-3235
- 1 One mechanical diaphragm with adjustable opening
- 2 constant fraction discriminators (CFD) ORTEC 584
- 1 time-to-amplitude converter (TAC) ORTEC 566
- 1 delay card
- 1 multichannel analyzer (MCA) ORTEC Easy-MCA
- 1 computer with Maestro® to save the fluorescence decay profiles
- 1 aluminum cube

Figure 3.5 shows the block diagram of the experimental setup for the TCSPC. An aluminum cube was used to place the organic scintillator, a collimator and to fix the PMT. The two photomultiplier tubes were used to detect the fluorescence photons emitted by the detector once it was excited by a X-ray source. The PMT signals were fed into two to different CFD to adapt the signals for the TAC. Before the CFD signal fed by the PMT referred as STOP, was

delivered to the TAC, a 75 ns delayed was used. The TAC signal was delivered to a MCA and finally the decay curve was observed in a PC. The details of the experiment are presented in the following pages as well as the other components required for the setup.

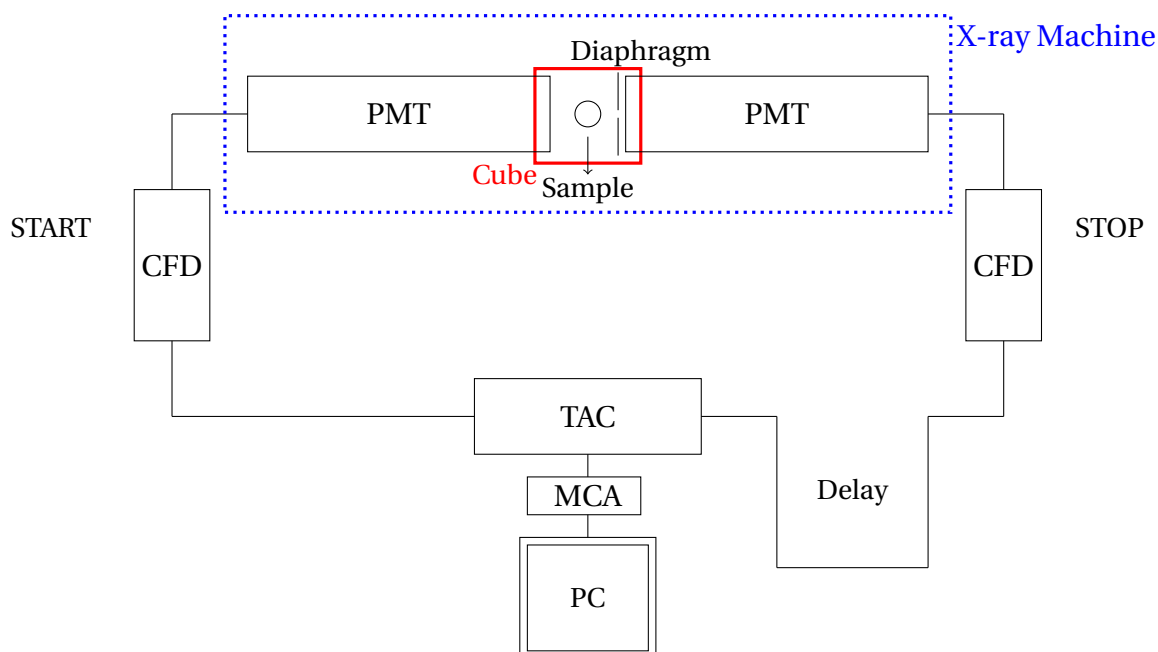


Figure 3.5 – The block diagram of the Time-Correlated Single Photon Count Technique used for this work. The PMT are powered by a voltage generator and the other components except for the MCA and PC, are powered by a rack.

3.3.1 The Photomultiplier Tube

A photomultiplier tube is composed of a detection window with a photocathode at its entrance. Incoming photons are guided to the cathode where they generate photoelectrons. These electrons are then accelerated and guided by the means of electric fields to a second dynode where once again, the electrons are multiplied. The process is repeated through out several dynodes. At the end of the multiplying chain, there is a anode that collects the electrons and generates output signal. It is important to note that the output signal is proportional to the number of generated photons in the photocathode, reason why it is very important that PMT is totally sealed. Else, atoms inside the PMT could be ionized by the accelerated electrons creating free electrons that would alter the proportionality of the signal.

The multiplication factor is known as gain and is given by :

$$\mu = (a E^k)^n \quad (3.25)$$

A is a constant, k depends of the type of cathode (it usually varies between 0.7 and 0.8), n is the number of dynodes and E voltage between dynodes[65]. Accordingly, operating voltage is a very important variable in order to obtain a good gain and it can usually go up to a couple of kV.

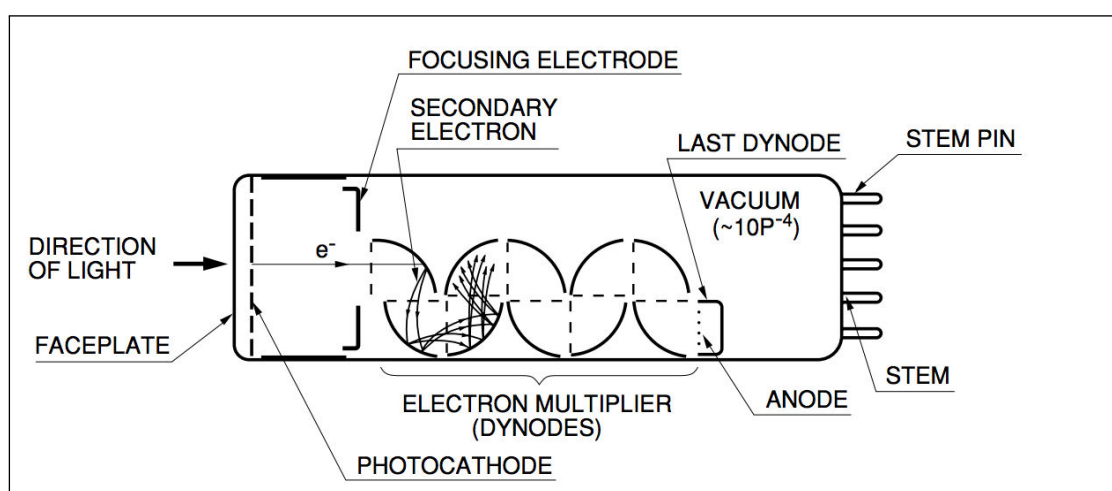


Figure 3.6 – Components of the photomultiplier tube (PMT) - *from*: Hamamatsu Photonics, KK, "Photomultiplier tubes: Basics and applications", Edition 3a, 2006

Another important parameter is the quantum efficiency $\eta(\nu)$ and it is the relationship between output photoelectrons and the incident photons. It depends on the nature of the photocathode, the reflection coefficient among others and the wavelength of the incident photon among others.

The PMT generates analog output signals that are characterized by a rising time, a fall time and a FWMD time. The temporal shift between the detection of photons in the cathode and the output signal is given by the electron transit time. This lapse of time corresponds to the time the electron takes to arrive from the cathode to the anode. The spread of this transit time corresponds to the standard deviation σ of all the transit times if the cathode were to emit the maximum possible number of photoelectrons. All these time parameters depend on the type of cathode, the size and geometry of the tube and operating kV.

3.3.2 The START and STOP Photomultiplier Tubes

As previously explained, two different PMT were required in the experimental setup. One PMT, referred as the PMT START, generates the electric signal needed to start recording the time and a second PMT, referred as the STOP PMT, generates the signal that stops the recording.

Let us start by describing the STOP PMT. In order to generate the STOP signal, the PMT had to be set in single-photon counting mode. In order to do so, a diaphragm was placed in front of the PMT to reduce the detection area to approximately 6^2 mm, hence the probability of detecting two or more photons at the same time practically became negligible. As explained earlier in this chapter, this is a mandatory experimental condition for recording high precision fluorescence decay profiles. We used the Hamamatsu R-3235 because of its very high sensitivity and gain and extremely short response.

The START PMT was a Photonis XP2020. The role of the START PMT is to detect the first fluorescence photons emitted by the scintillator to generate the needed signal to start the time recording. Hence there was no mechanical system to reduce the size of its detection window as opposed to the STOP PMT. In this case, it was of no importance if more than one photon was detected because the interest was on just starting the electronics.

3.3.3 The Electronic Chain

Each of the PMT output analog signal was fed to a constant-fraction discriminator (ORTEC 584). Each CFD delivers a negative logic output signal at the precise instant the rising time of PMT analog signal crosses a preset threshold. Regardless the slope of the analog signal, the CFD is triggered at the same instant providing very precise timing. The fast logic output signal is then fed into an time-to-amplitude convertor. The TAC is an electronic component that generates an analog output signal with a height proportional to the time difference between the START and STOP input signals. When the START signal is detected, a capacitor starts to be charged until the input of a STOP signal. The capacitor is charged by a constant voltage, consequently, the charge is proportional to the time ($V \propto t$). The voltage pulse from the TAC is fed to an ORTEC Easy-MCA multichannel analyzer. To each different voltage value, a corresponding memory bin is assigned. The time resolution depends on the chosen number of bins set in the MCA. The MCA was set in a 1 k resolution per $1\mu\text{s}$, which meant that each channel had an assigned time value of 0.976 ns. Finally, the data is sent from the MCA to a software in a PC where the time resolved fluorescence decay is displayed. In

Chapter 3. The Experiment

Appendix B more details are given about these different components.

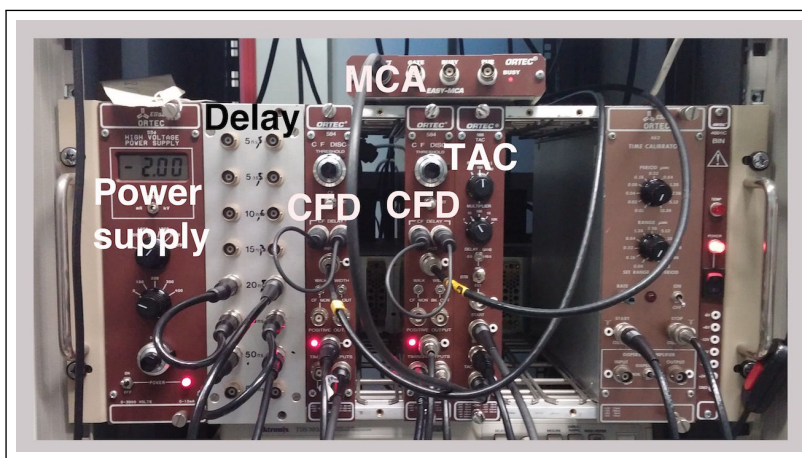


Figure 3.7 – Electronic components used for the TCSPC

3.3.4 The Cube

The sample was placed inside an aluminum cube (fig:3.8) where the two photomultiplier tubes type Hamamatsu R-3235 were screwed to two adjacent faces of the cube. A diaphragm was placed in front of one of the PMT. A hollow cylinder in lead was used to collimate the X-rays. The collimator was put perpendicular to the two PMTs and it had a 1 mm opening. A screwing mechanism allowed to place the organic scintillator in the correct position. The cube was designed to keep any other source of photons outside the cube.

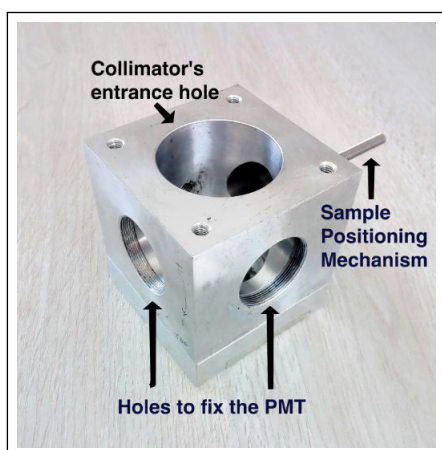


Figure 3.8 – The cube where the PMTs are screwed, the sample and collimator are placed.

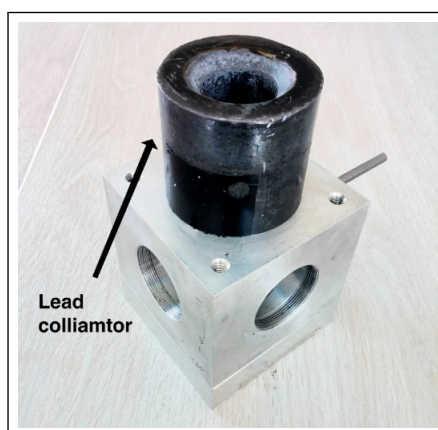


Figure 3.9 – Lead collimator : guides X-rays & helps reducing backscattering radiation.

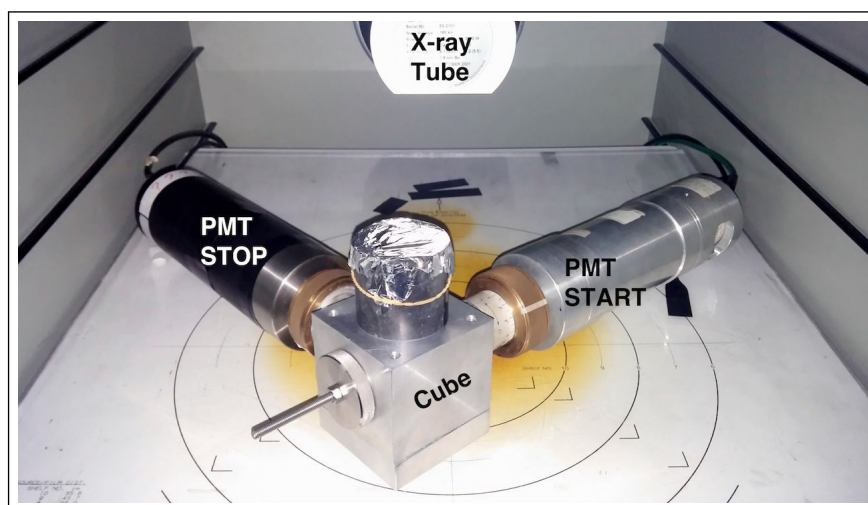


Figure 3.10 – The experiment configuration. The PMT START and STOP are screwed to the cube and the collimator opening is placed just under the X-ray window to avoid as much as possible any sort of backscattering radiation. The organic scintillator is placed inside the cube where no other source of light can come in to disturb or even damage the PMTs.

Several conditions had to be met in order to obtain the most adequate set up. First, the geometry between the excitation source, the sample and the PMT is very important. The sample was placed directly under the collimator in the middle of the cube and the PMTs were fixed directly in front of the sample. It can be pictured as a XYZ frame in 3D space with the origin at $(0,0,0)$; the two PMTs are on the x -axis and y -axis, the collimator on the z -axis and the organic scintillator at the origin. The crystal had to face both PMT to be sure that the emitted photons by the sample are detected. One PMT was almost totally shielded using the diaphragm to allow a single-photon count. To determine the size of the diaphragm, an oscilloscope was fed directly by the PMT where the signal could be analyzed. Third, the thickness of the walls of the cylinder used to collimate the X-rays was enough to auto absorb the possible lead fluorescence under X-ray radiation. Forth, it was important to find a position between the other end of collimator and x-ray tube window in order to avoid as much as possible x-ray diffraction and scattering inside the machine. Different distances were tested while a ionization chamber placed outside the cube measured the dose. It was found that a distance of 1cm was enough to guide the x-rays into the cube through the collimator. Fifth, a 3mm layer of lead was placed between the X-ray source and the scintillator. This was required to decrease the intensity of the X-rays to avoid PMT saturation. At the same time, the characteristic radiation was filtered as well. Finally, comparisons made with and without collimator let us determine that more than 99% of scattered and diffracted x-rays were absorbed when using the collimator.

3.3.5 The Scintillators

Two different organic scintillators were used in this work: Anthracene and p-Terphenyl monocrystals as shown in table 2.1. Very small samples were needed to generate enough light to record the fluorescence decay curve. They were grown by fusion zone, technique that allows to have a purity of over 99%. The picture on the right corresponds to the sample of anthracene with a thickness of around 0.5 mm. The sample of p-Terphenyl had a radius of approximately 4mm. The following table shows the organic scintillators used in this work[66]:

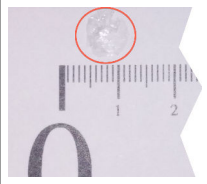

	Anthracene	p-Terphenyl
		
Emission (λ_{max})	448 nm	391 nm
Absorption(λ_{max})	357 nm	276 nm
τ^2	17.99 ns	3.15 ns
weight	2.8 mg	76.2 mg

Table 3.1 – Characteristics of the organic scintillators used in this work.

The obtained values of the lifetime for to each of the studied organic scintillators correspond to the values found in literature for both p-Terphenyl[67] and anthracene[68, 69] as well as the measured values of the lifetimes here in the laboratory are presented in table 3.1, allowing to validate the experimental setup of the TCSPC.

3.3.6 The X-Ray Machine

A Faxitron X-ray CP-160 system (picture 3.11) was used for the research. It has a 1000W Comet MXR-160/0.4-3/0 with a variable output up to 160kV and a max current of 16mA. It was possible to set the voltage-current of our choice to follow the desired experiment conditions and the system was controlled using a LABVIEW program specifically developed for this purpose. The irradiation time could also be programmed The machine complies with all the radiation protection regulations and the manufacturer's recommendations and user guidelines were respected to avoid any safety hazard.

²Lifetimes were measured using a Horiba JovinYvon FluoroMax®-4 Spectrofluorometer



Figure 3.11 – The CP-160 Cabinet X-radiator System

3.3.6.1 The Principles of X-Ray Generation

X-rays are a type of electromagnetic radiation with wavelengths ranging between 0.5 and 2.5. According to the quantum theory, the electromagnetic radiation can be considered as photons with an associated energy of:

$$E = h \nu, \quad (3.26)$$

where $h = 6.63 \times 10^{-34} \text{Js}$ is Planck's constant and the relationship between the frequency ν and wavelength λ is:

$$\lambda = c / \nu, \quad (3.27)$$

where c is the speed of light.

X-rays are produced by accelerating electrons under the influence of a potential difference V . They electrons gain the kinetic energy E_k :

$$E_k = \frac{1}{2} m_e v^2 = e V, \quad (3.28)$$

where m_e is the mass of the electron, v its velocity and e its charge.

The electrons lose their energy through collisions and radiative interactions generating X-rays in the process. Only around 1% of the total kinetic energy generate the X-rays, the other 99% is dissipated as heat.

The X-rays are produced in an X-ray tube where there are two electrodes, a cathode and an anode in the vacuum. A high voltage generator produces the difference potential needed to accelerate the electrons that are generated in the cathode. First, the electrons are produced in the cathode by a constant current. Due to the electrical resistance in the cathode filament, the current heats it up and electrons are released. This phenomenon is known as thermionic resistance. Increasing the current passing through the filament would increase the number of electrons emitted. The generated electrons are collected on the surface of the filament and due to charge repulsion among the charges. The number of created electrons is limited and kept into place by a negatively charged cup around the filament until the potential between the anode and the cathode is activated that accelerates the electrons from the cathode to the anode. The electrons gain a kinetic energy proportional to the applied potential and the electron charge as seen in formula 3.28. The produced electrons are guided and focused to the anode.

Anodes are made of different materials depending on their intended use. Tungsten (W) one of the most common material used in anodes. The generation of X-rays occur when the accelerated electrons ejected from the cathode interact with the anode. Electrons can interact with other electrons removing electrons from the orbits in the atom. X-rays mostly interact with K-shell electrons. The vacancy in the orbital is occupied by an outer shell electron. A photon is created during this transition with an energy corresponding to the difference between the binding energies of the initial and final orbital. The photons generate characteristic peaks in the X-ray emission spectrum and it is specific of each material. Figure 3.12 shows an X-ray energy spectrum where the K-radiation is observed.

Electrons also interact with the atomic nucleus transforming their kinetic energy into electromagnetic radiation in a process known as *Bremstrahlung*. Electrons lose more kinetic energy when their trajectory is closer to the nucleus due to stronger decelerations and change in trajectory. The maximum X-rays are produced by direct collisions between the electron and the nucleus though these events are very improbable (Less than 0.5% [70]) Indeed, the probability of interaction decreases as the distance between the trajectory of the electron

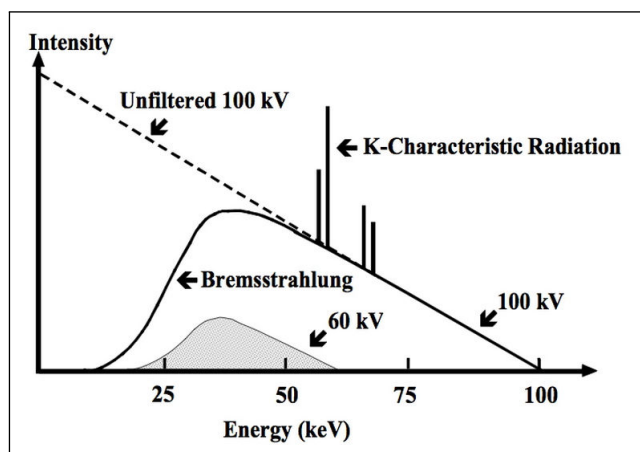


Figure 3.12 – X-ray energy spectrum. - *from*: J.C.P Heggie, N. A. Liddell, and K. P. Maher, "Applied Imaging Technology," 4th Edition, 2001.

and nucleus decreases too. The results of these interactions is a continues spectrum with a maximum determined by the voltage between anode and cathode.

As the voltage increases, the energy spectrum grows to the left of the x-axis in 3.12. Just increasing the current in the cathode will increase the number of electrons which will increase the measured intensity of X-rays.

3.3.7 The Ionization Chamber

A Camberra Babyline 81 portable Gamma and X-ray Doserate Meter/Dosemeter is an detector capable of estimating the dose rate and the dose absorbed by human tissue under photon irradiation with energies ranging between 8keV to 10MeV.

The dose rate of the Faxitron CP-160 X-ray machine was determined for different kV/mA combinations using a calibrated (November 2014) Camberra Babyline 81 (Figure 3.13). Dose rates measured by this detector are presented in the next chapter.

The objective was to compare the dose rase measurements acquired with the Babyline to those measured by the TCSPC for each of the two organic scintillators. The results are presented in the next chapter as well.

Special attention was given to the position of the chamber in order to respect the same geometry as used with the TCSPC setup (as seen in Figure 3.10) in order to reproduce the same experimental conditions.



Figure 3.13 – The Camberra Babyline 81

"It is the tension between creativity and skepticism that has produced the stunning and unexpected findings of science."

Carl Sagan

4 Experimental Results and Data Analysis

Introduction

The experimental results from this work are the continuation of 40 years of research in this laboratory. Until today, research was mainly focused to the understanding of the different mechanisms of scintillation as a result of the incident radiation. In this work, both the fundamental mechanisms of fluorescence emission and a quantitative approach of the relationship between dose and scintillation are presented together for the first time. For this first research, two of the most common and known scintillators, anthracene and p-Terpheny were excited by X-rays between 80kV and 140kV and currents of 3, 5 and 7mA. The experimental data was recorded by the instruments and methods described in chapter 3 to record as accurately as possible the fluorescence decay curves in order to extract the researched data in the best possible conditions.

Considering the important amount of experimental data recorded, a systematic data analysis was developed to study all the fluorescence decay curves. The experimental decay curve contains the information of the prompt and delayed component for a scintillator excited by a certain X-ray tube kV/mA combination. As mentioned in Chapter 3, the observed decay curve is the convolution between the physical response of the organic scintillator with the instrument response function of the system described in the previous chapter and by figure 4.1. A deconvolution procedure is needed when lifetimes of the studied organic scintillator are of the same order of magnitude as the IRE. There are several deconvolution techniques such as the least-square iterative deconvolution method, the method of moments, the exponential series method or the Fourier transform method among many others (including variations of the methods here listed) [71, 72, 73, 74] . The choice for the deconvolution

procedure depends on the number of exponential decay laws in the decay profile or if there is a need for an initial guess of the decay law or laws. The least-square method has proven to be one of the most accurate technique to derive simple decay profiles and it allows partial or total fits of the data. [75]. Special attention was given to the fit procedure in order to improve the statistics as results could significantly vary with similar fit conditions.

Once the parameters describing the prompt component were found, the delayed component was determined by subtracting the fitted prompt component from the total decay curve. Both components are integrated and then the ratio R , between them was found. The fitting procedure

This chapter is divided in two parts: the first one presents the mathematical method in detail used to adjust and fit the fluorescence decay curve in order to deduce the fluorescence decay lifetime τ by the exponentially modified Gaussian. The results are presented in the second part for anthracene and p-Terphenyl.

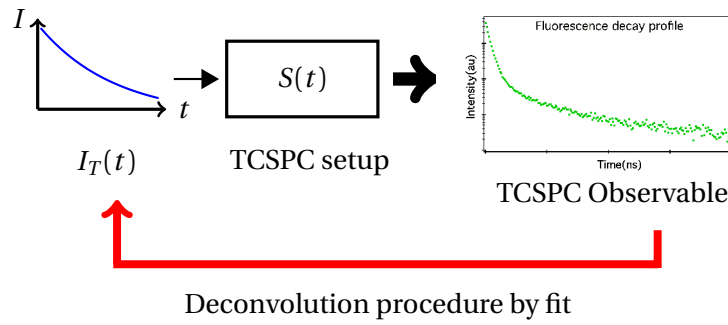


Figure 4.1 – This figure represents what it is observed using the TCSPC technique and

4.1 Fluorescence Decay Fitting

We were interested in the reconstruction of the intensity decay curve of the scintillator based on the experimental results. In this section, the procedure used to obtain the real physical responses $i_T(t)$, $i_p(t)$ and $i_d(t)$ is described.

The first step was to determine the instrument response function IRF . Based on [60, 76, 77], the $S(t)$ was approximated by a Gaussian distribution. These papers describe different techniques to deconvolve fluorescence decay curves. To validate their deconvolution procedures, experimental data were reproduced to determine the goodness of fit. The response of the

scintillator was described by a decay function and the instrument response by a Gaussian distribution:

$$G(x) = \frac{1}{\sigma\sqrt{2\pi}} e^{-(x-\mu)^2/2\sigma^2}. \quad (4.1)$$

Results in these papers were both accurate and precise which validated the approximation method for the deconvolution in the study and analysis of decay curves. Therefore, the instrument response function $S(t)$ is represented by a Gaussian distribution.

As seen in equation 3.2, the observed light intensity $I_M(t)$ is the convolution between $i_T(t)$ and the $S(t)$. Let us write this equation again, replacing $S(t)$ by $G(t)$. We obtain :

$$I_M(t) = i_T(t) * G(t). \quad (4.2)$$

Taking into account equation 2.3, $I_M(t)$ becomes:

$$I_M(t) = [i_p(t) + i_d(t)] * G(t) = i_p(t) * G(t) + i_d(t) * G(t), \quad (4.3)$$

Furthermore, the convolutions between the the prompt and delayed component of fluorescence with $G(t)$ are defined by:

$$I_p(t) = i_p(t) * G(t) \quad (4.4)$$

$$I_d(t) = i_d(t) * G(t) \quad (4.5)$$

Before going any further, let us recall that:

- $I_M(t)$ corresponds to the observed experimental data.
- The assumption that $S(t)$ is described by a Gauss distribution.
- The prompt fluorescence $i_p(t)$ is given by a single exponential function.

Considering that the prompt component is described by a single exponential, it seemed a logical choice to first determine $I_p(t)$, and based on equation 3.6, $I_d(t)$ is:

$$I_d(t) = I_M(t) - I_p(t). \quad (4.6)$$

As seen in equation 4.4, $I_p(t)$ is the convolution between two functions. The convolution between the exponential and a Gaussian distribution was analytically solved; the result was an accurate fit of prompt component of the observed fluorescence curve[78]. This convolution is known as the *exponentially modified Gaussian*.

4.1.1 The Exponentially Modified Gaussian Distribution

The exponentially modified Gaussian (EMG) function is defined by the convolution of an exponential and a Gaussian distribution. This distribution fits to right tailed peaks¹ and it is commonly used in other domains such as chromatography and spectroscopy.

Let us start by writing the EMG function:

$$y(t) = e(t) * g(t) = \int_{-\infty}^{\infty} e(t)g(t - t') dt', \quad (4.7)$$

where t' is the accessory variable of integration. The accessory variable t' represents the shift of the function $g(t)$ relative to $e(t)$ ². Let us now replace $e(t)$ and $g(t)$ by the exponential distribution and gaussian distribution. As both $e(t)$ and $g(t)$ are defined for $t > 0$, the integration limit³ is $[0, t]$ The function $y(t)$ is defined by:

$$y(t) = \int_0^t A \frac{1}{\sqrt{2\pi\sigma^2}} e\left(-\frac{t'}{\tau}\right) e\left(-\frac{(t-t')^2}{2\sigma^2}\right) dt' \quad (4.8)$$

$$= A \frac{1}{\sqrt{2\pi\sigma^2}} \int_0^t e\left(-\frac{t'}{\tau}\right) e\left(-\frac{(t-t')^2}{2\sigma^2}\right) dt', \quad (4.9)$$

$$(4.10)$$

¹It is less adequate to fit left tailed peaks[79]

²The convolution integral is commutative; the accessory variable can be written in the function $e(t)$ too. Choosing $g(t)$ is an strategical approach to solve the integral easier.

³Though it is mathematically not correct, the limits of the integral can be defined from $[0, +\infty]$ or even from $[-\infty, +\infty]$, the results will only have a negligible error.

where A is the amplitude of the exponential function and μ the position of the gaussian peak. The analytical solution of the convolution integrals shown above may be solved taking account the following algebraic identity:

$$\lambda\alpha + \frac{(\alpha - \beta)^2}{2\gamma^2} = \tau\lambda - \frac{1}{2}\gamma^2\lambda^2 + \frac{(\alpha - \beta + \gamma^2\lambda)^2}{2\gamma^2}. \quad (4.11)$$

Identity 4.11 allows to rearrange the terms in the exponential functions to evaluate the integral. The solution to equation 4.9 is:

$$y(t) = C + \frac{A}{2} \exp\left[\frac{\sigma^2}{2\tau^2} - \frac{t - \mu}{\tau}\right] \left[1 + \operatorname{erf}\left(\frac{t - \mu - \frac{\sigma^2}{\tau}}{\sigma\sqrt{2}}\right)\right], \quad (4.12)$$

where C is a variable to adjust the offset, if any, τ is the decay time of the scintillator, σ the standard deviation of the gaussian and erf is the error function⁴.

4.1.2 Fit of the Measured Decay Curve

Equation 4.12 was used to fit the experimental profiles of the different acquired decay curves in order to determine τ , the lifetime of the scintillator. The equation depends on five parameters: τ, σ, μ, A and C . The fitted parameters C, A and μ were compared to the experimental data to have a quick idea of the goodness of fit; the value of σ , corresponding to the gaussian distribution describing the IRF, remained almost constant as it depended on the electronic response of the system and the lifetime of the organic scintillator. Finally, the lifetime of studied organic scintillator was given by τ and the profile of the prompt component $I_p(t)$ could be traced.

The figure 4.2 illustrates one of many recorded curves by the TCSPC technique. By giving a first glance to the curve, it was possible to have a rough idea of the parameters of the values of A, c and μ . A was the height of the peak; C , the offset, was estimated by calculating the average height of the data before the peak; and μ defined by the location of the peak.

The result of the fit of the decay curve is presented in figure 4.3 which is divided in three

⁴The error function $\operatorname{erf}(z)$ is a function defined by $\operatorname{erf}(z) = \frac{2}{\sqrt{\pi}} \int_0^z \exp(-x^2) dx$

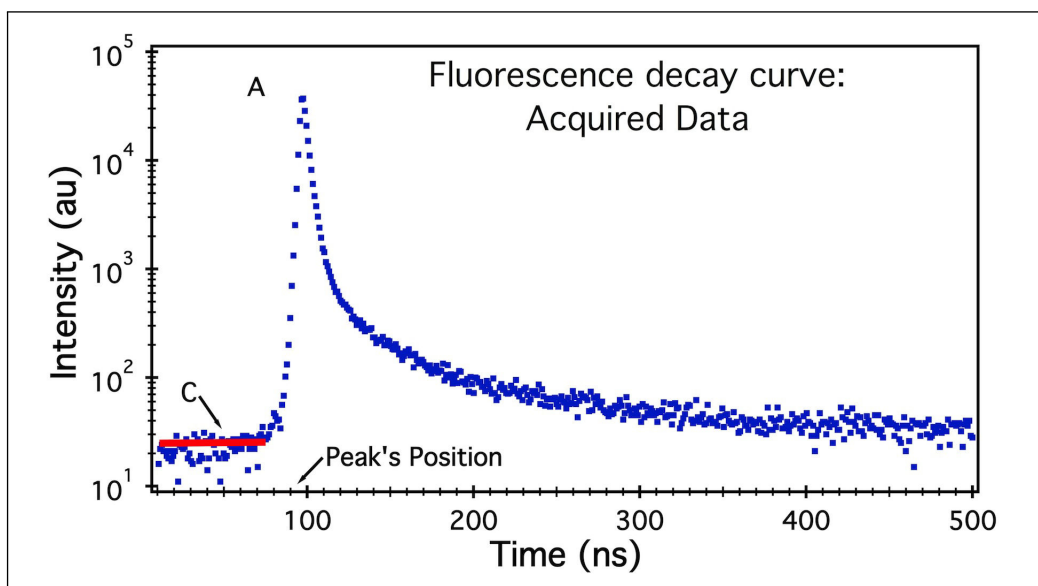


Figure 4.2 – Raw data of the fluorescence decay curve

parts: the middle graph shows the measured decay profile in green and in blue the fitted curve by equation 4.12⁵, the dotted gray curve in the bottom only shows the fit curve; the red dotted curve corresponds to the residuals, the difference between the measured data and the fitted curve. The estimated value of τ is used to estimate the prompt component and then using equation 4.6, the delayed component is found. Results are shown in 4.4 for a sample of p-Terphenyl irradiated by X-ray set at 160kV and 3mA.

⁵The observed difference between the EMG fit and the fluorescence decay curve *before* the peak is discussed in appendix C

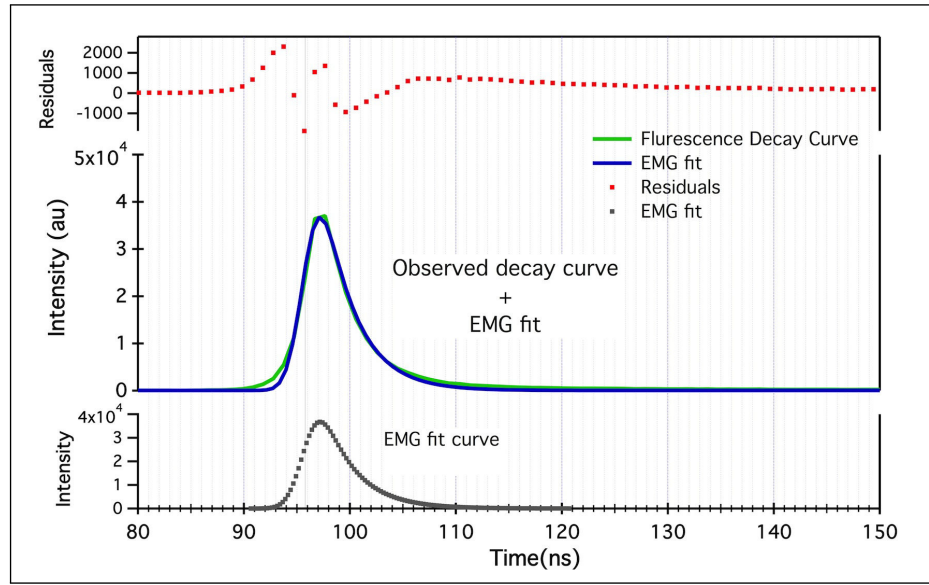


Figure 4.3 – Fit results of the fluorescence prompt component.

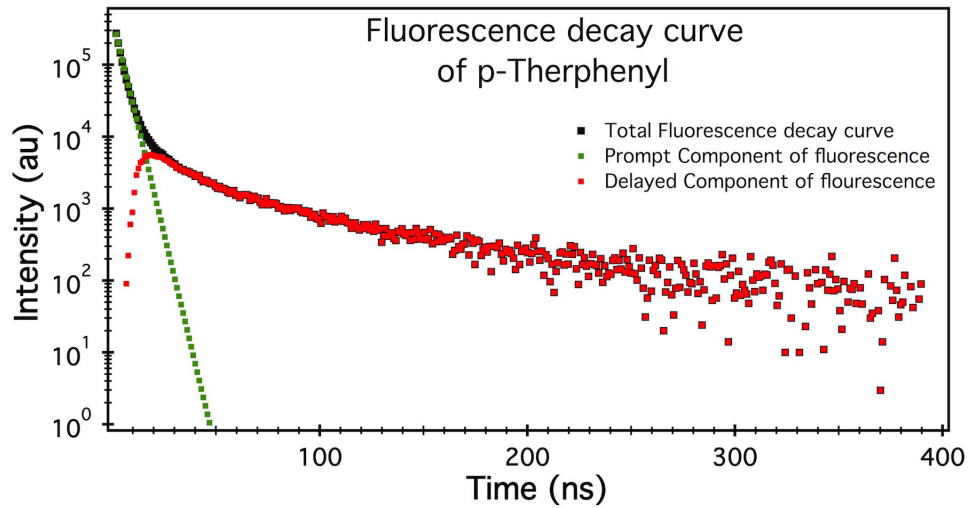


Figure 4.4 – This fluorescence profile corresponds to the light emitted by a p-Terphenyl scintillator under X-ray irradiation. The dotted line in green corresponds to the prompt intensity $i_p(t)$ and the area under this curve is L_p , the total light emitted by the component. The red dotted line corresponds to the delayed component $i_d(t)$ and its total are is represented by L_d . The sum of the two components is the total fluorescence decay curve

Residuals

The residual is defined as the gap between the fit value \hat{y} and the observed value y :

$$\text{Residual} = \hat{y} - y \quad (4.13)$$

The difference between the maximum data value for the measured fluorescence decay curve and the fit was estimated for all decay curves. At the highest point of the fluorescence peak, a difference of around 10% was observed between the measured value and the fit value. In theory, the residual for this point should be zero; this is only true for this single point at because its origins depends exclusively on the prompt component of fluorescence. For $t \in [1, \sim 10\tau \text{ ns}]$, the fluorescence decay curve is composed of both the prompt and delayed components. Hence the residual value contains the value of the delayed component as well, making it impossible to determine what corresponds to the delayed component to the residual value. Consequently, the error due to the fit was estimated to be of 10%.

4.2 Results

The organic scintillators were irradiated using different X-ray tube currents and potentials between the anode and cathode. First, different tables with the relevant experimental results will be presented for each of the two studied scintillators. Then, data will be presented in graphs.

4.2.1 Tables of Results

Experimental curves were fitted and analyzed and the results are shown in tables 4.4, 4.5, 4.6, 4.1, 4.2 and 4.3. Each estimated value of τ and the respective error in its estimation for each kV/mA combination is presented; L_p and L_d are the number of counts integrated between 0 and 400 ns and normalized to 1 hour for the prompt and delayed component respectively; L_p/L_d is the ratio between the areas of the two components; the different errors are given by ΔL_p , ΔL_d and $\Delta L_p/L_d$.

kV	p-Terphenylnyl							
	3mA							
	$\tau(ns)$	$\Delta\tau(ns)$	L_p	ΔL_p	L_d	ΔL_d	L_p/L_d	$\Delta L_p/L_d$
80kV	3.0	0.3	2952	10.3%	693	10.6%	4.25	20.8%
90kV	3.1	0.2	8559	10.2%	1938	10.5%	4.41	20.7%
100kV	3.1	0.3	14964	10.2%	3396	10.4%	4.40	20.6%
110kV	3.0	0.3	21037	10.1%	4766	10.3%	4.41	20.4%
120kV	3.1	0.3	27681	10.1%	6301	10.3%	4.39	20.4%
130kV	3.1	0.3	37129	10.1%	8138	10.2%	4.56	20.3%
140kV	3.1	0.3	49033	10.1%	10584	10.2%	4.63	20.4%
150kV	3.1	0.3	69286	10.1%	14537	10.3%	4.76	20.4%
160kV	3.1	0.2	98896	10.0%	20497	10.2%	4.82	20.2%

Table 4.1 – Table of results for different values of kV at 3mA for p-Terphenyl.

4.2.1.1 p-Terphenyl

kV	p-Terphenyl							
	5mA							
	$\tau(ns)$	$\Delta\tau(ns)$	L_p	ΔL_p	L_d	ΔL_d	L_p/L_d	$\Delta L_p/L_d$
80kV	3.1	0.2	10739	10.3%	2509	10.6%	4.44	20.9%
90kV	3.0	0.3	27425	10.1%	6406	10.3%	4.28	20.4%
100kV	3.1	0.2	42102	10.1%	9880	10.0%	4.27	20.03%
110kV	3.1	0.3	65217	10.1%	16008	10.2%	4.72	20.4%
120kV	3.1	0.4	91304	10.2%	22572	10.3%	4.04	20.5%
130kV	3.1	0.7	101693	10.2%	25468	10.3%	4.01	20.5%
140kV	3.1	0.5	140313	10.2%	33839	10.3%	4.14	20.5%
150kV	3.2	0.3	186616	10.1%	45006	10.1%	4.74	20.2%
160kV	3.1	0.3	227672	10.2%	54907	10.4%	4.76	20.5%

Table 4.2 – Table of results for different values of kV at 5mA for p-Terphenyl.

kV	p-Terphenyl							
	7mA							
	$\tau(ns)$	$\Delta\tau(ns)$	L_p	ΔL_p	L_d	ΔL_d	L_p/L_d	$\Delta L_p/L_d$
80kV	3.1	0.2	16902	10.2%	4219	10.4%	4.01	20.6%
90kV	3.1	0.4	38029	10.1%	9487	10.2%	4.01	20.4%
100kV	3.1	0.2	63084	10.20%	14178	10.4%	4.44	20.6%
110kV	3.1	0.5	88036	10.2%	21641	10.3%	4.07	20.5%
120kV	3.1	0.4	137414	10.2%	33505	10.3%	4.10	20.5%
130kV	3.1	0.3	144128	10.2%	35331	10.3%	4.08	20.5%
140kV	3.1	0.3	207274	10.1%	45629	10.3v%	4.54	20.5%

Table 4.3 – Table of results for different values of kV at 5mA for p-Terphenyl.

4.2.1.2 Anthracene

	Anthracene							
kV	3mA							
	$\tau(ns)$	$\Delta\tau(ns)$	L_p	ΔL_p	L_d	ΔL_d	L_p/L_d	$\Delta L_p/L_d$
80kV	17.0	0.4	5971	10.2%	418	10.8%	14.29	21.0%
90kV	16.6	0.4	22726	10.1%	1625	10.5%	13.98	20.6%
120kV	16.4	0.4	37996	10.1%	2685	10.3%	14.15	20.4%
140kV	16.8	0.4	126366	10.1%	8272	10.3%	15.27	20.4%
160kV	16.7	0.4	321802	10.0%	22707	10.2%	14.17	20.2%

Table 4.4 – Table of results for different values of kV at 3mA for anthracene.

	Anthracene							
kV	5mA							
	$\tau(ns)$	$\Delta\tau(ns)$	L_p	ΔL_p	L_d	ΔL_d	L_p/L_d	$\Delta L_p/L_d$
80kV	16.2	0.4	12029	10.2%	889	10.7%	14.18	20.9%
90kV	17.0	0.3	42104	10.1%	3101	0.4%	13.58	20.5%
120kV	16.7	0.4	168510	10.1%	12546	10.3%	13.43	20.4%
140kV	16.5	0.4	294204	10.1%	22509	10.3%	13.07	20.4%
160kV	17.0	0.7	561941	10.1%	42088	10.2%	13.35	20.3%

Table 4.5 – Table of results for different values of kV at 5mA for anthracene.

	Anthracene ⁶							
kV	7mA							
	$\tau(ns)$	$\Delta\tau(ns)$	L_p	ΔL_p	L_d	ΔL_d	L_p/L_d	$\Delta L_p/L_d$
80kV	16.6	0.2	16200	10.2%	1097	10.7%	14.76	20.9%
90kV	16.9	0.22	61368	10.1%	4197	10.4%	14.62	20.5%
120kV	16.4	0.24	240829	10.1%	16343	10.3%	14.74	20.4%
140kV	16.6	0.18	416483	10.1%	31345	10.3%	13.29	20.4%

Table 4.6 – Table of results for different values of kV at 7mA for anthracene.

4.2.1.3 σ and the Instrument Response

Tables 4.8 and 4.7 show σ^7 obtained during the fit which corresponds to the width of the instrument response. The units of σ are in ns for both tables. The precision to 1/100 of the ns is calculated by the fit algorithm.

⁶The X-ray machine is limited to max. power of 1000W. In consequence, the 160kV experimental measurement cannot be done at this current.

⁷The relationship between the FWHM and σ is: $FWHM = 2\sqrt{2\ln 2}\sigma \approx 2.355\sigma$

	p-Terphenyl					
kV	3mA		5mA		7mA	
	σ	$\Delta\sigma$	σ	$\Delta\sigma$	σ	$\Delta\sigma$
80	1.26	0.01	1.27	0.01	1.38	0.01
90	1.30	0.01	1.36	0.01	1.38	0.01
100	1.26	0.01	1.37	0.02	1.38	0.01
110	1.26	0.01	1.31	0.01	1.37	0.01
120	1.26	0.01	1.38	0.01	1.37	0.01
130	1.29	0.01	1.38	0.01	1.38	0.01
140	1.28	0.01	1.38	0.01	1.36	0.01
150	1.28	0.01	1.33	0.01	X	X
160	1.29	0.01	1.30	0.01	X	X

Table 4.7 – Fitting values obtain for sigma for p-Terphenyl.

	Anthracene					
kV	3mA		5mA		7mA	
	σ	$\Delta\sigma$	σ	$\Delta\sigma$	σ	$\Delta\sigma$
80	5.07	0.06	5.33	0.15	5.3	0.07
90	5.17	0.06	5.23	0.06	5.46	0.07
120	5.24	0.06	5.27	0.06	5.39	0.07
140	5.22	0.06	5.35	0.17	5.50	0.07
160	5.25	0.06	5.16	0.15	X	X

Table 4.8 – Fitting values obtain for sigma for anthracene.

The observation of σ depends on the light emitted by organic scintillator which at the same time depends on τ , its lifetime. Therefore, the observed $S(t)$ is not the same for anthracene and p-Terphenyl. It is understood that the electronic response of the detection chain is always the same, but as the lifetimes change for different organic scintillators, so does the value of σ . It is important to notice that regardless the energy of the X-rays used to excite the organic scintillator, the value of σ must remain constant under the same experimental conditions. The different estimated values of σ for p-Terphenyl were compared each other and the same was done with the σ values of anthracene. Once again, these comparisons allowed to determine the goodness of fit and to validate the experimental setup.

4.2.2 Graphs

4.2.2.1 Babyline

The dose rates measured by the Camberra Babyline 81 as function of the different kV/mA combinations are presented in the following graphs. In graph 4.5, the dose rate is traced as function of the voltage for different currents; in graph 4.6, the dose rate is plot as function of the current for different voltages.

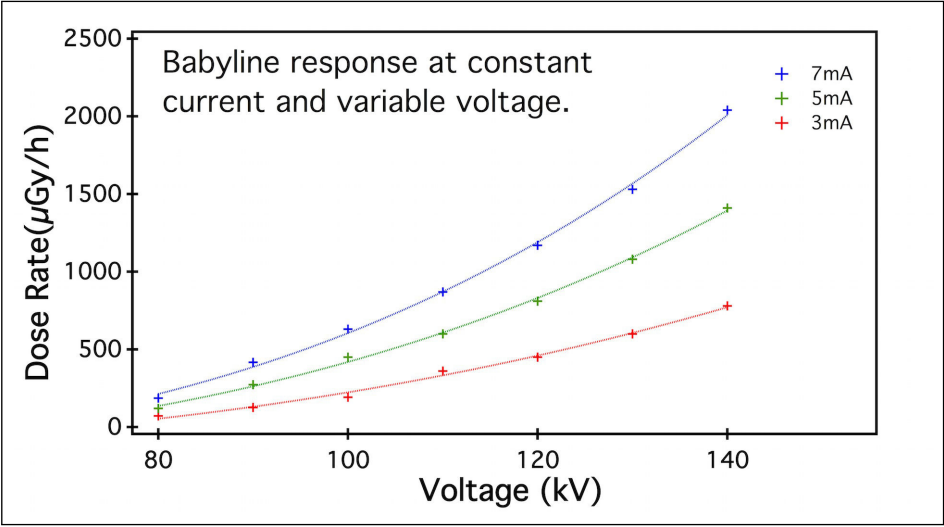


Figure 4.5

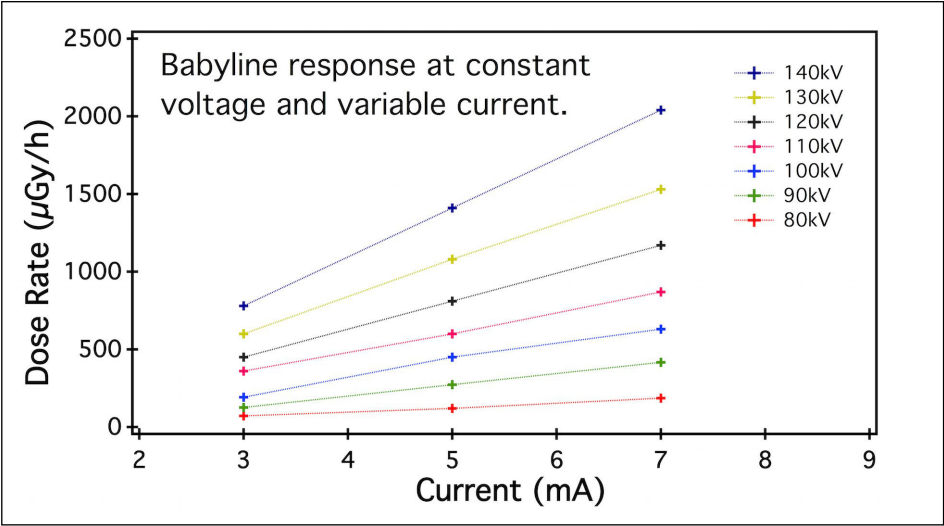


Figure 4.6

4.2.2.2 p-Terphenyl

The experimental data for p-Terphenyl irradiated by different energies of X-rays is plot in the following graphs :

- The first three graphs show a decay curve at 140kV for the three different currents used where the power law $t^{-3/2}$ is observed, characteristic of the delayed component as seen in Chapter 2.
- Graphs 4.10, 4.11 and 4.12 show the variation of the total light intensity ($L_p + L_d$) as well as the prompt (L_p) and delayed (L_d) components in function of the voltage (kV) at constant current (mA). Voltage varied between 80kV and 160kV with a 10kV step for each of the three different currents used (3mA, 5mA and 7mA). For each voltage-current pair, the total, delayed and prompt experimental measurement was plot. Graph 4.13 shows to the total light intensity ($L_p + L_d$) emitted by p-Terphenyl for each of the three different currents.
- The variation of the total light intensity ($L_p + L_d$), the prompt (L_p) and delayed (L_d) components in function of the current (mA) at constant voltage (kV) is plotted in graphs 4.14 to 4.20. Voltage was constant while three different currents were set: 3mA, 5mA and 7mA.
- The total delayed component in function of the Camberra Babyline⁸ is plot in graphs 4.21, 4.22 and 4.23. The first of the three graphs corresponds to the intensity measured at 3mA for different kV (80kV-90kV-100kV-110kV-120kV-130kV-140kV) in function of the measured dose rate using the dosimeter. The second corresponds to 5mA with the same voltage range and the third graph is the plot for 7mA with a voltage range finishing at 140kV⁹.

⁸The *Portable Gamma and X-ray Doserate Meter/Dosimeter* was used to determine the dose at each voltage-current pair

⁹The X-ray machine has a limit of 1000W, therefore the 150kV and 160kV cannot be set at this current.

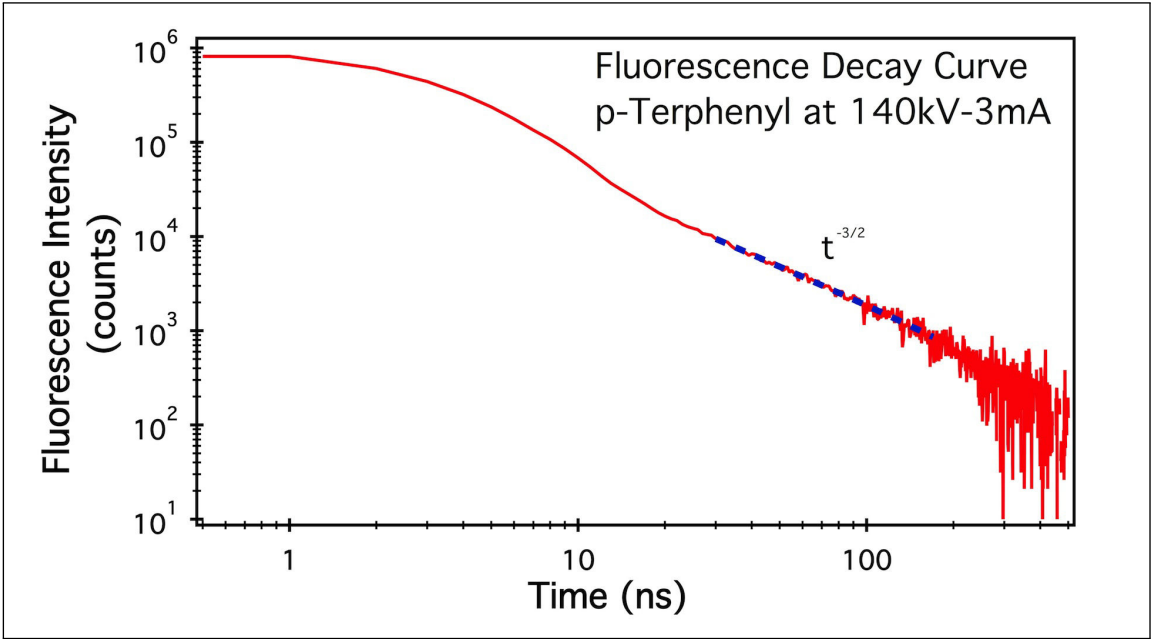


Figure 4.7

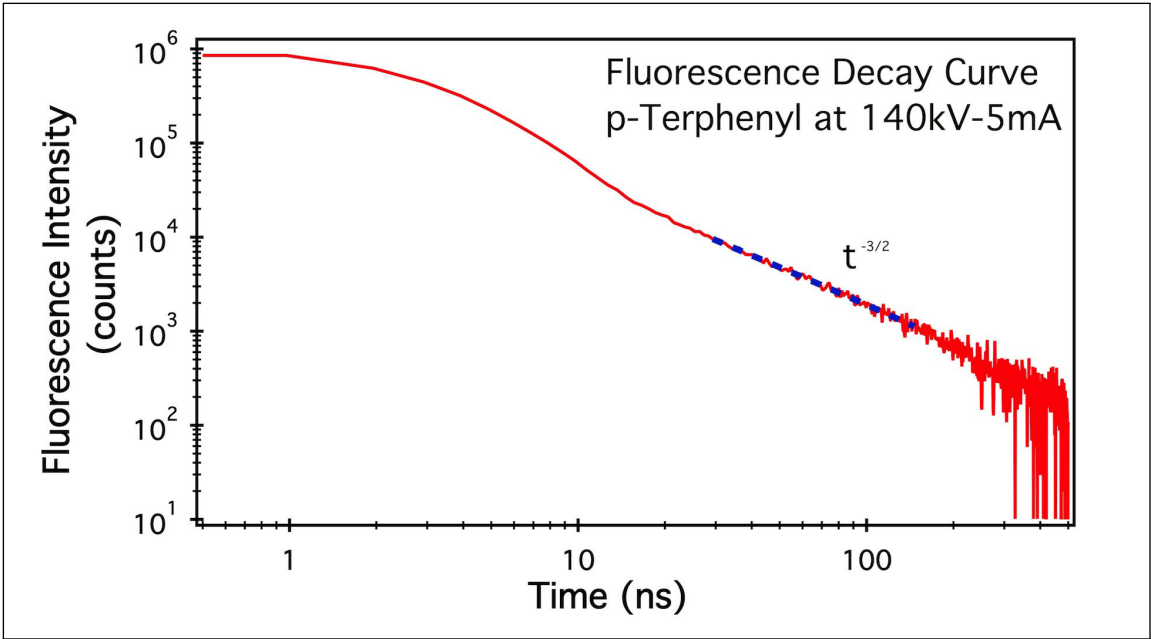


Figure 4.8

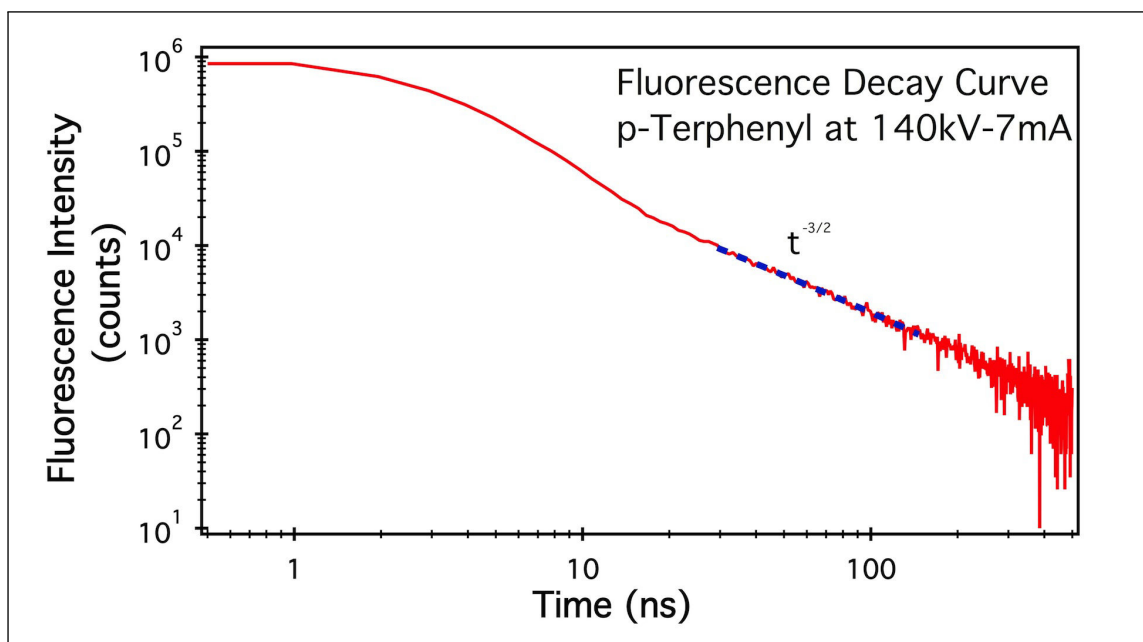


Figure 4.9

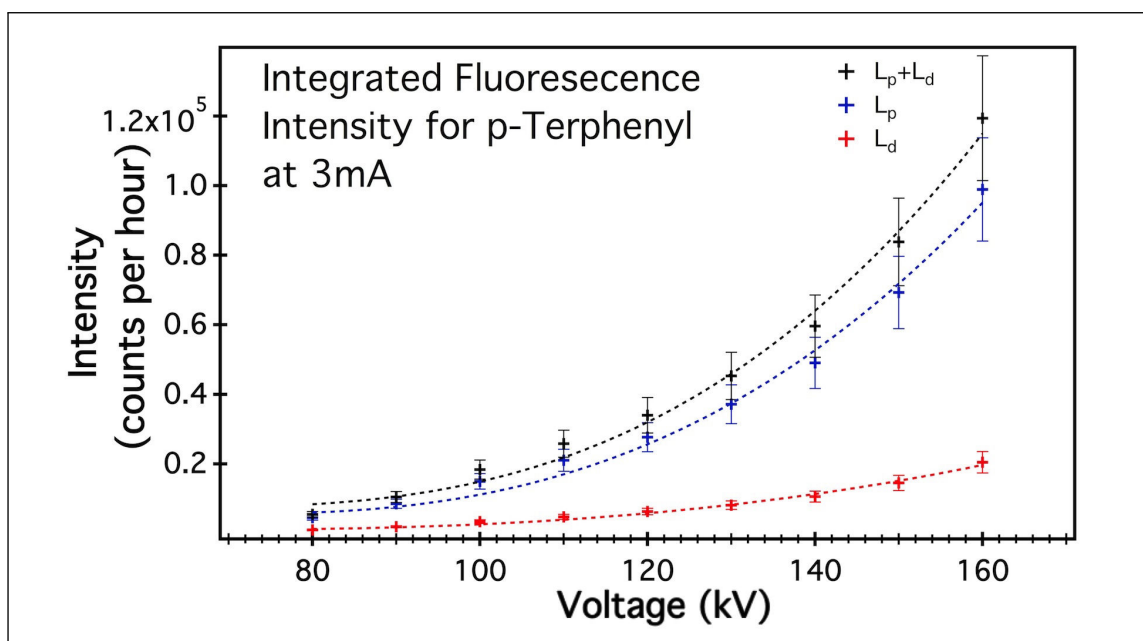


Figure 4.10

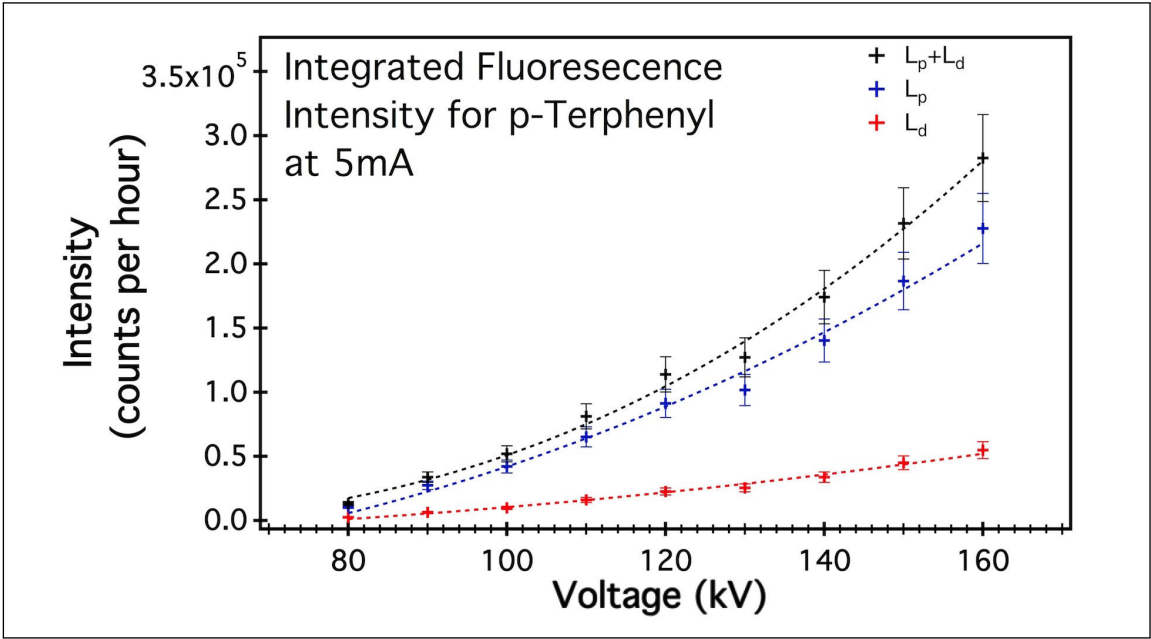


Figure 4.11

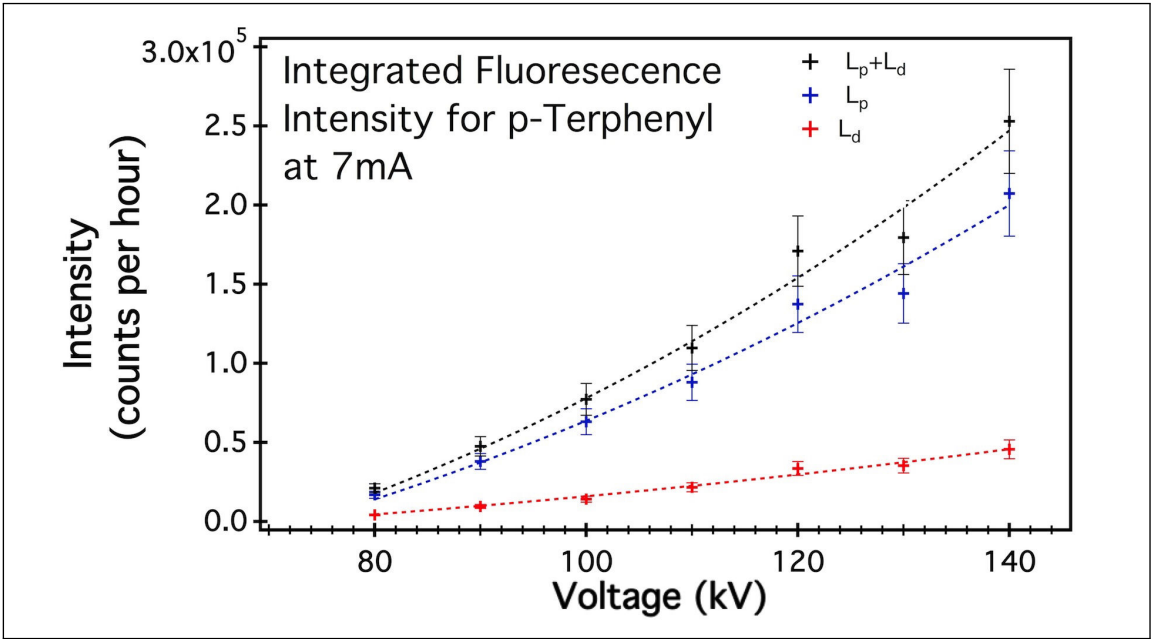


Figure 4.12

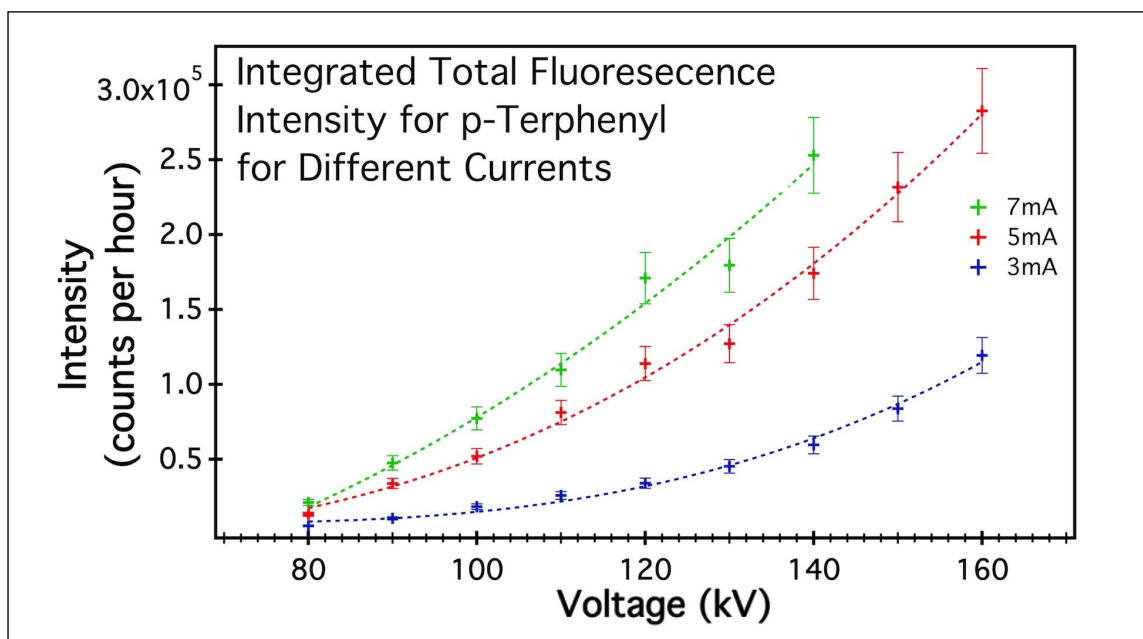


Figure 4.13

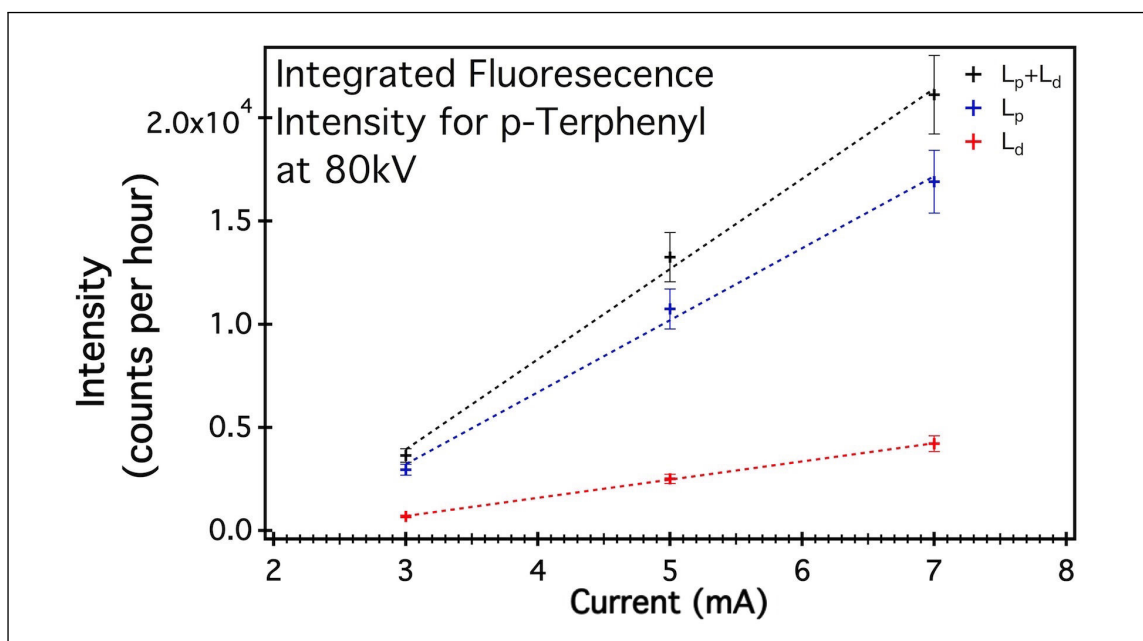


Figure 4.14

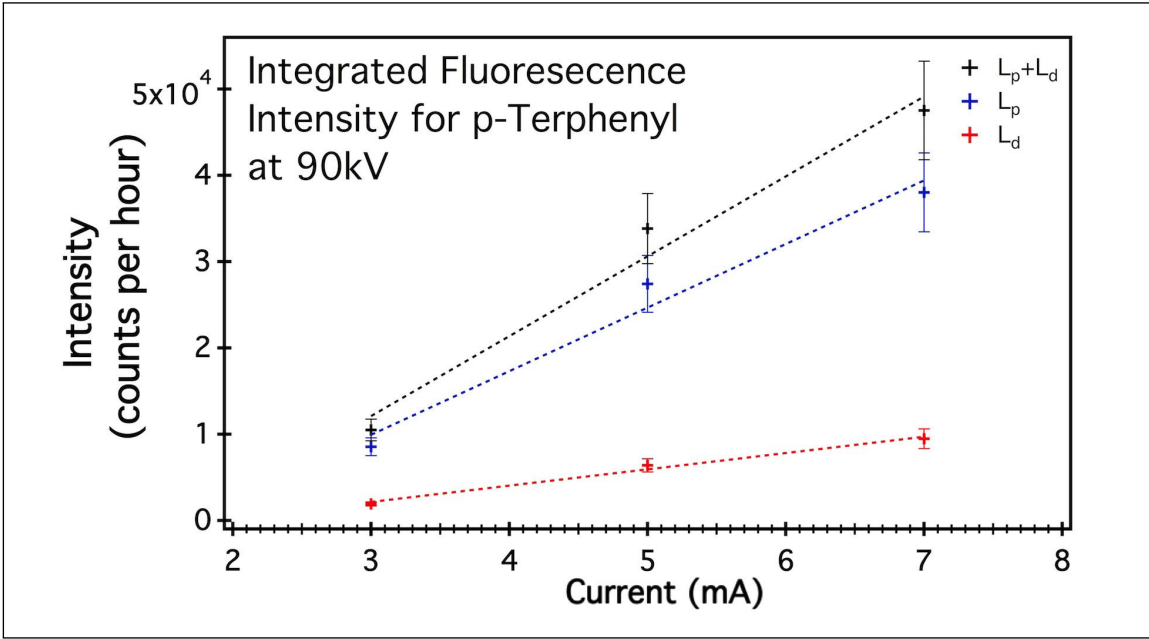


Figure 4.15

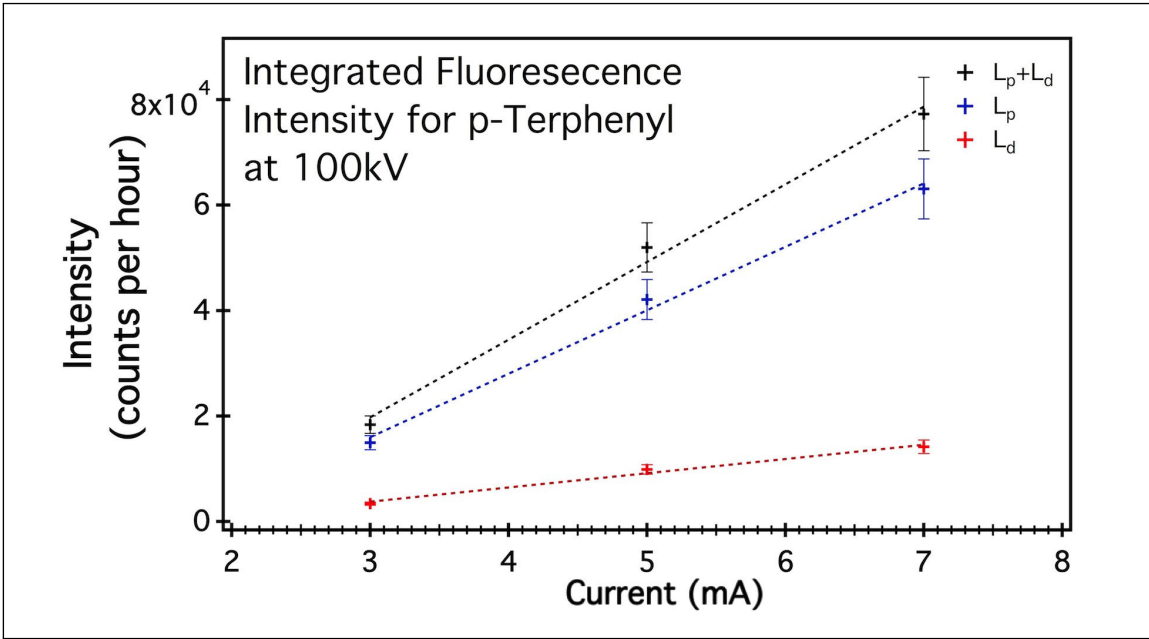


Figure 4.16

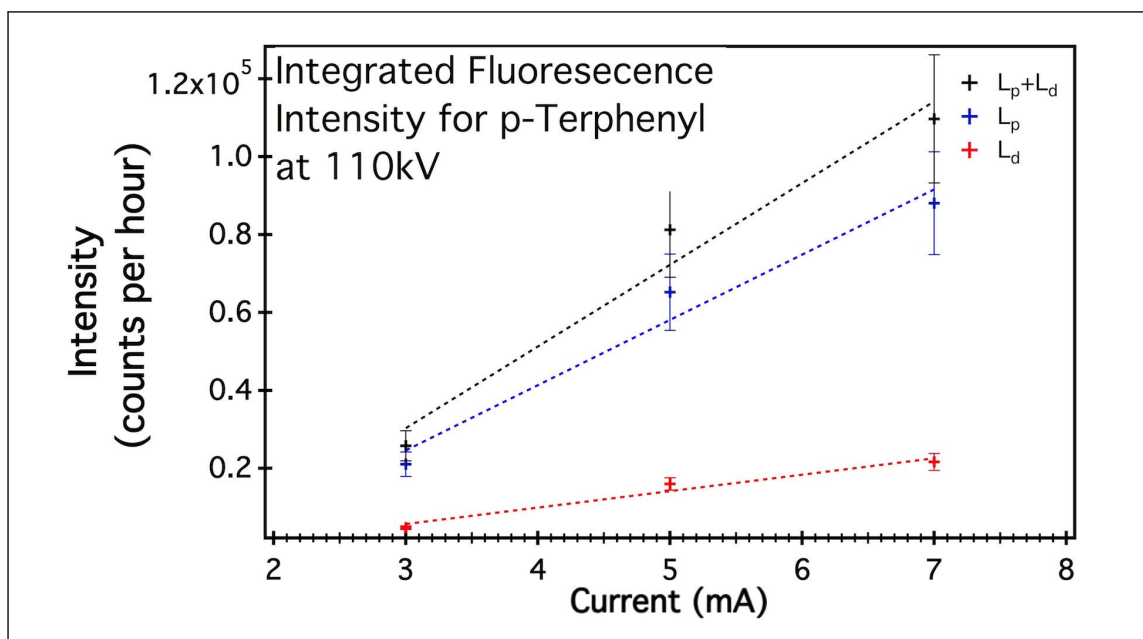


Figure 4.17

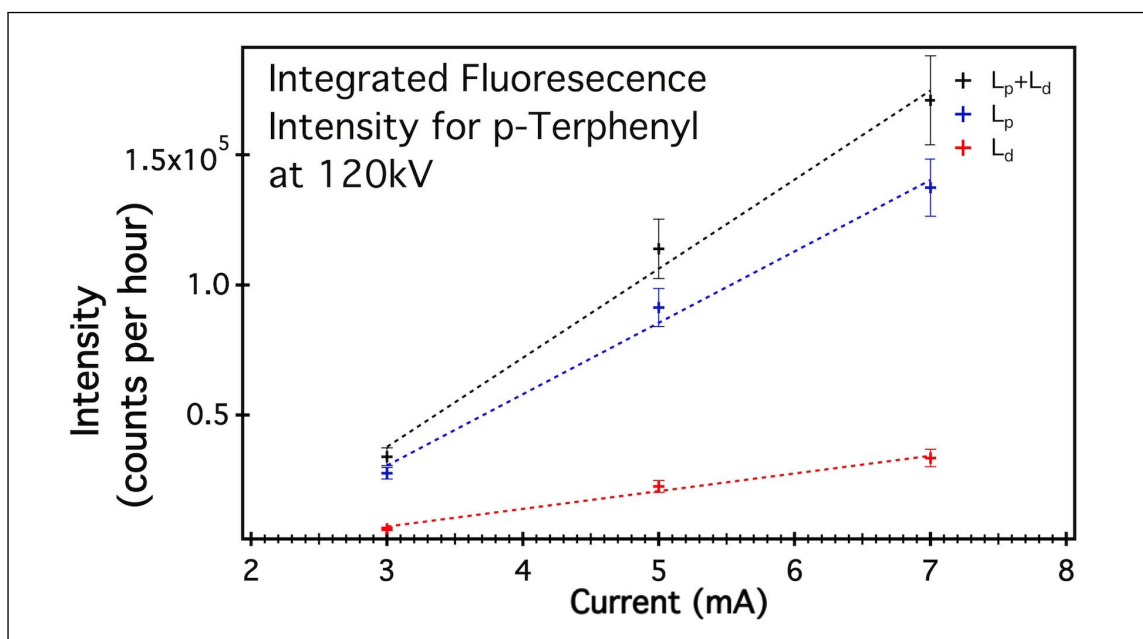


Figure 4.18

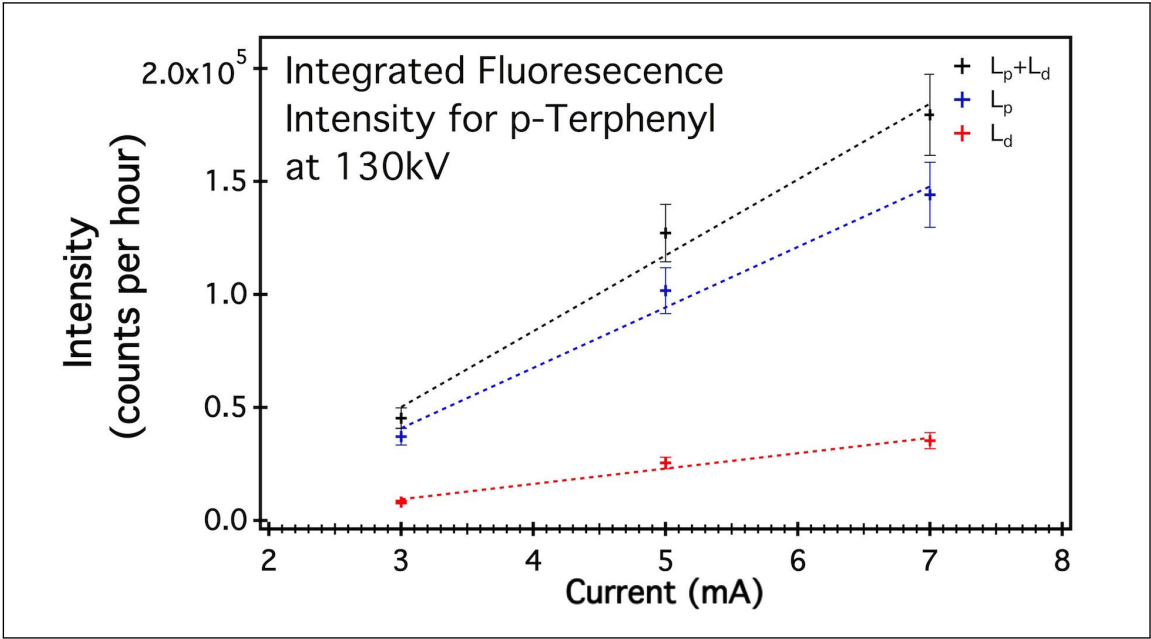


Figure 4.19

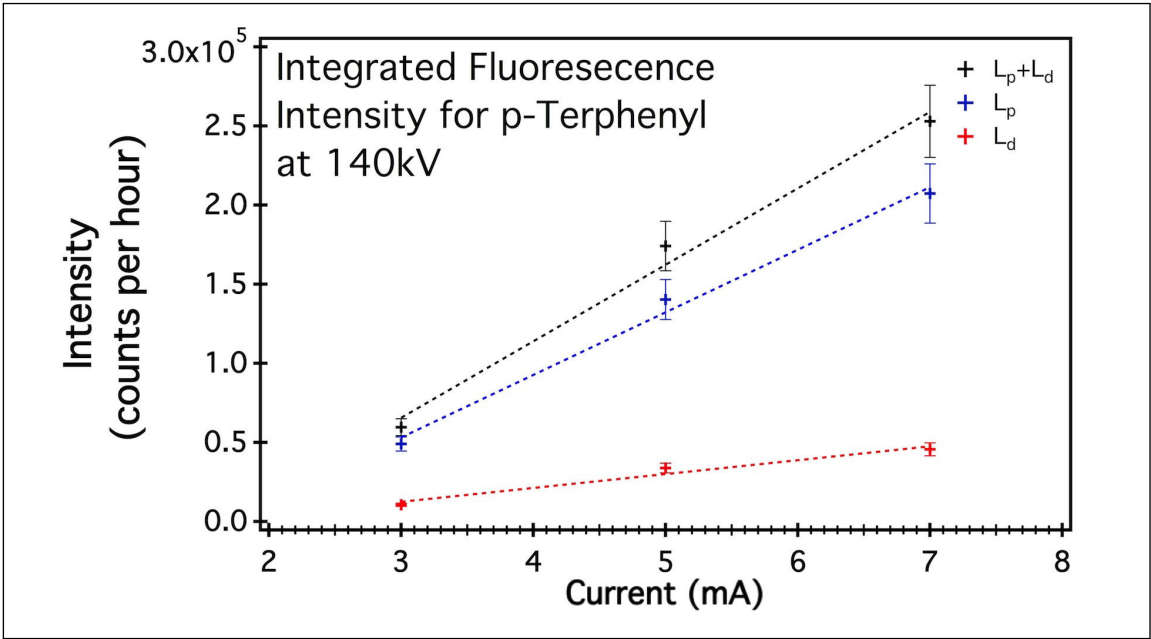


Figure 4.20

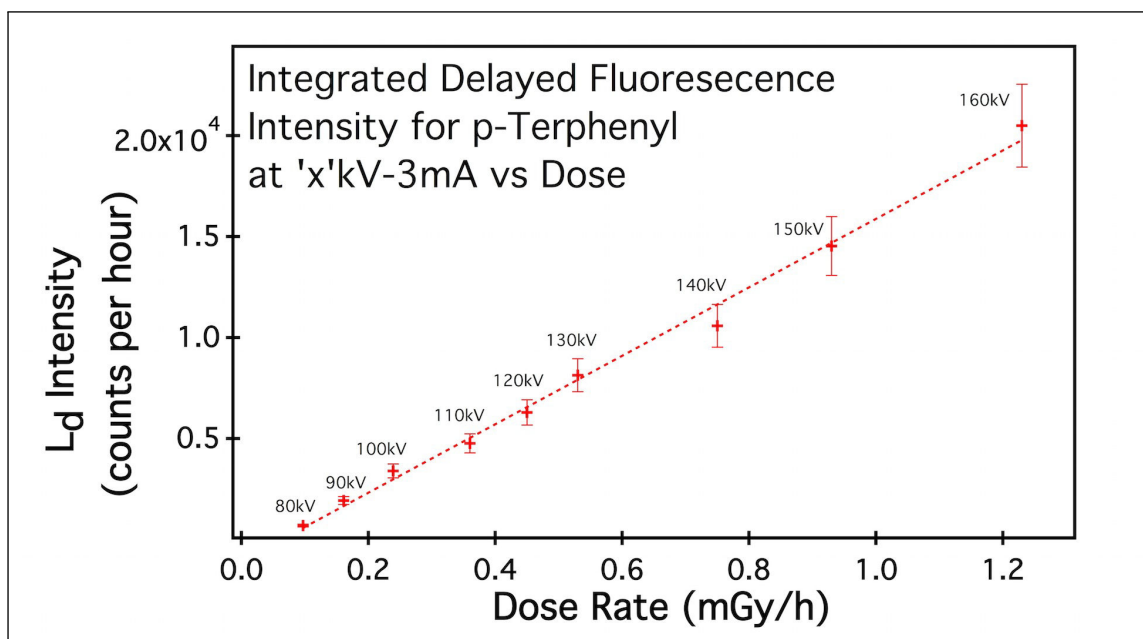


Figure 4.21

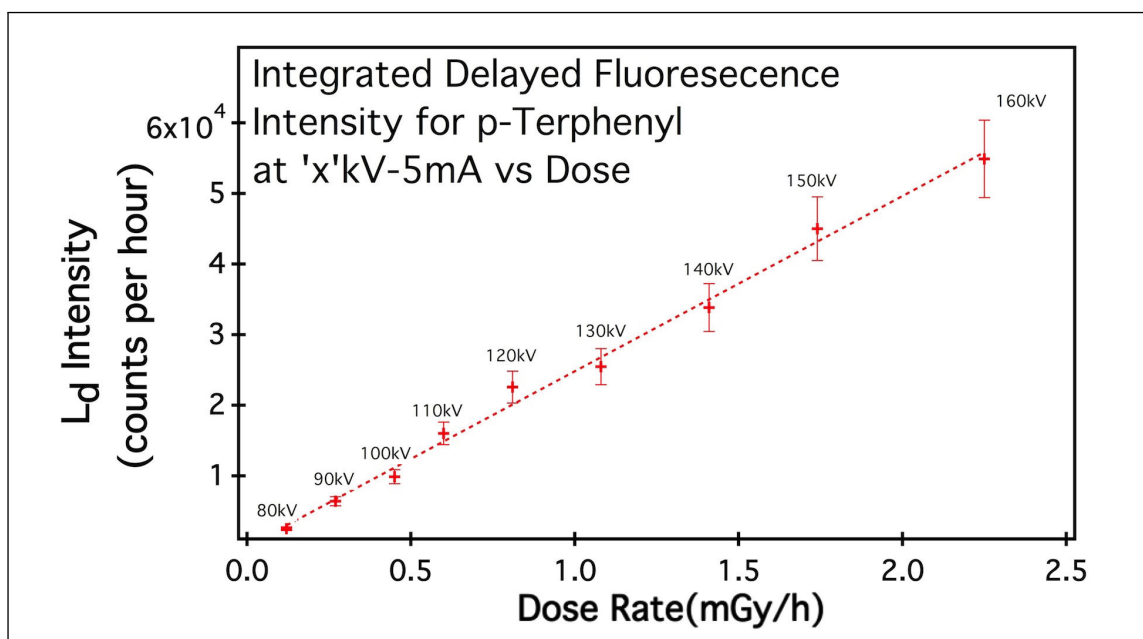


Figure 4.22

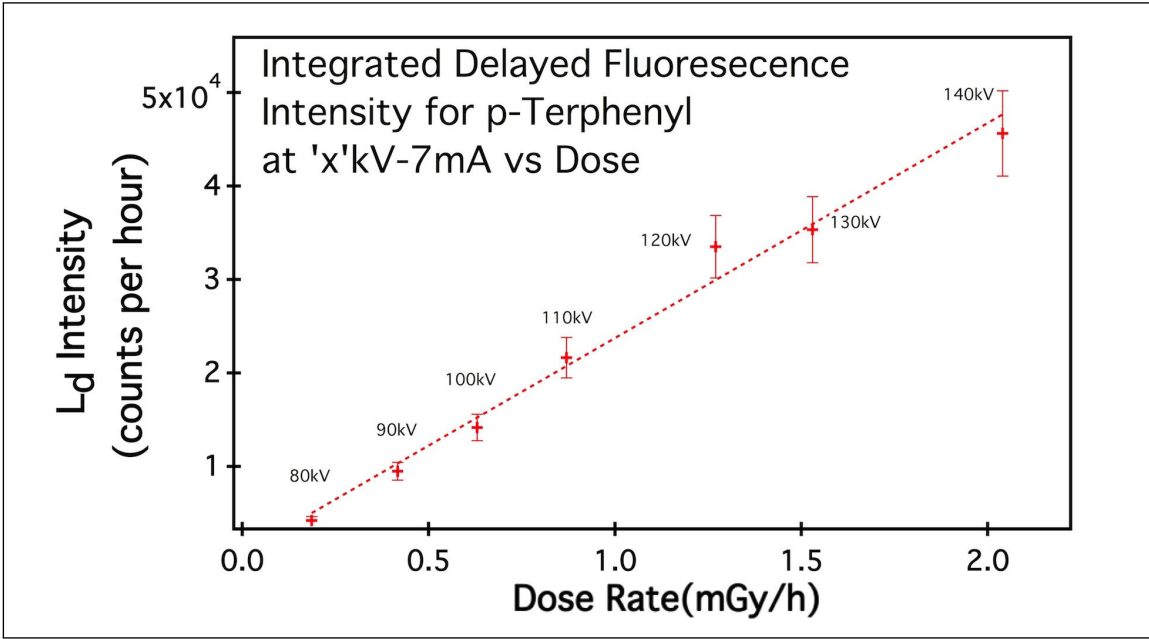


Figure 4.23

4.2.2.3 Anthracene

The experimental data for anthracene irradiated by different energies of X-rays is plot in the following graphs:

- In graphs 4.24, 4.25 and 4.26 the characteristic decay law of $t^{-3/2}$ is plotted over the decay curve obtained with a constant voltage of 140kV and currents of 3, 5 and 7mA.
- Graphs 4.27, 4.28 and 4.29 show at a constant current, the variation of the total intensity ($L_p + L_d$) decomposed in its total prompt (L_p) and total delayed (L_d) components in function of the voltage values of 80kV, 90kV, 120kV, 140kV and 160kV¹⁰.
- The total intensity of light defined ($L_p + L_d$) and the prompt (L_p) and delayed (L_d) is plot in function of the current values of 3mA, 5mA and 7mA at a constant voltage (80kV, 90kV, 120kV and 140kV. Results are in graphs : 4.30, 4.31, 4.32 and 4.33.
- In the following three graphs the comparison of the delayed component of fluorescence in function of the dose rate measured by the Babyline 81 is plotted. The current was constant while the voltage changed using the same values described above.

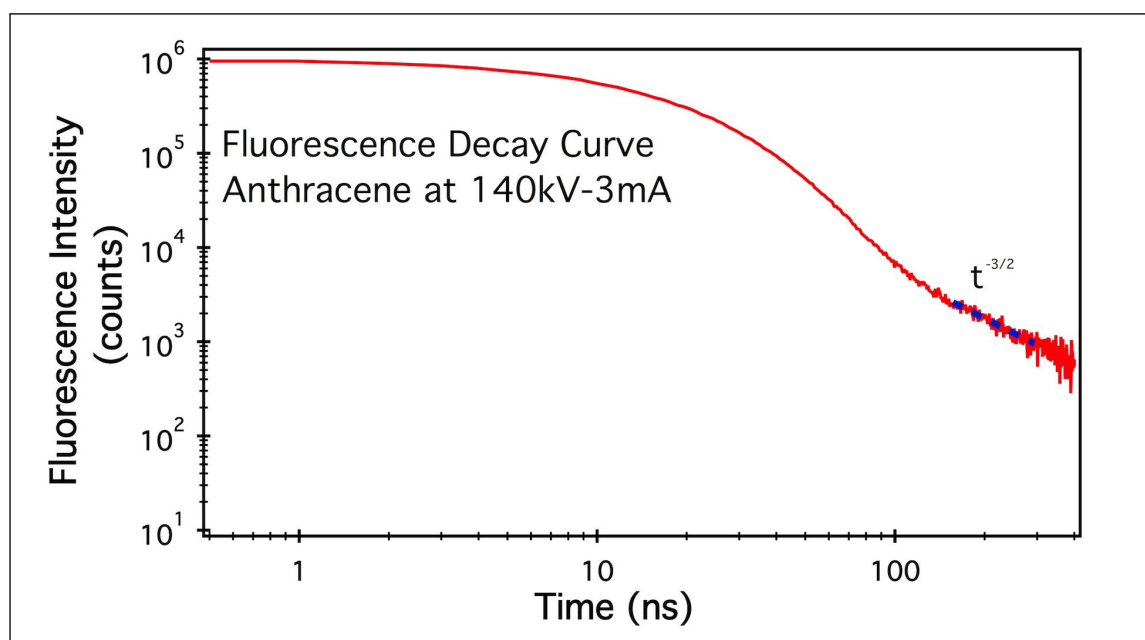


Figure 4.24

¹⁰Except for the current of 7mA due to X-ray machine limits as mentioned before.

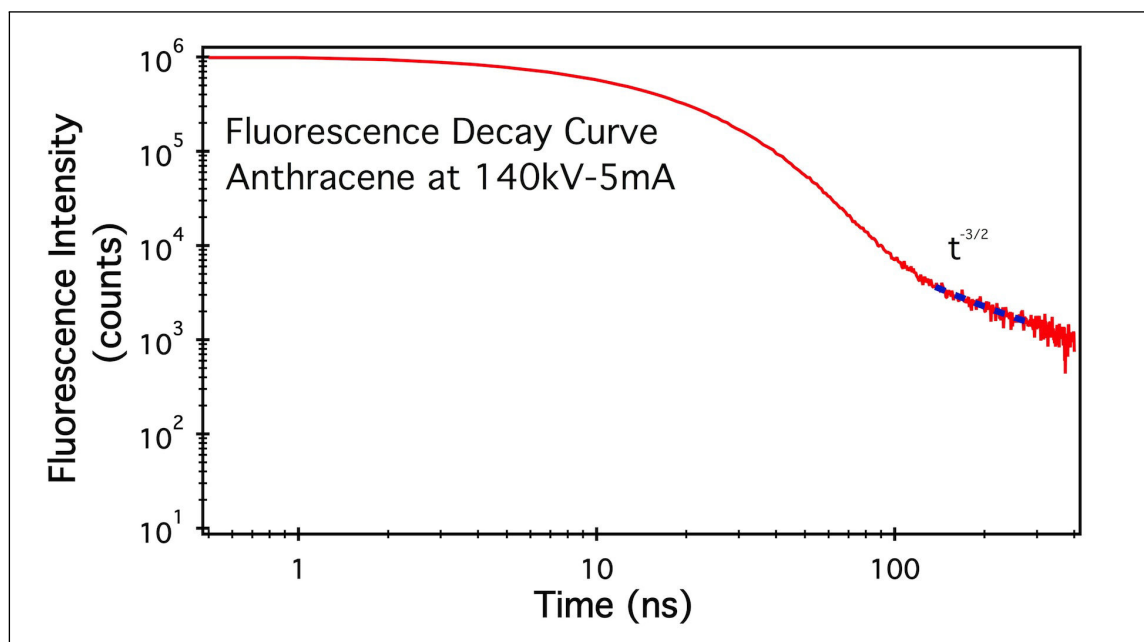


Figure 4.25

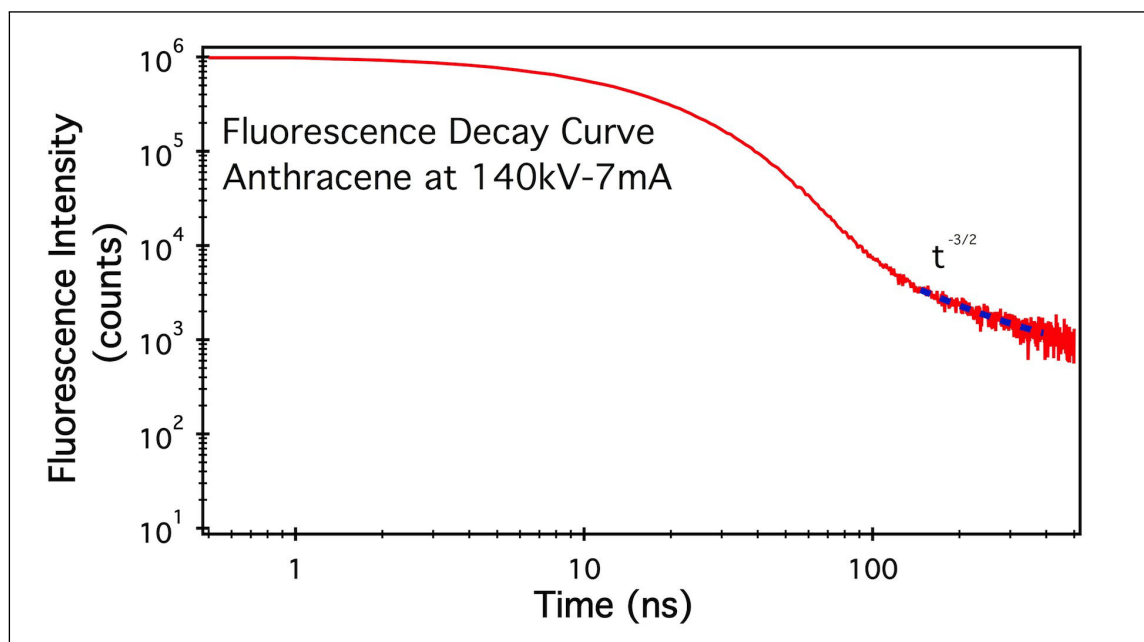


Figure 4.26

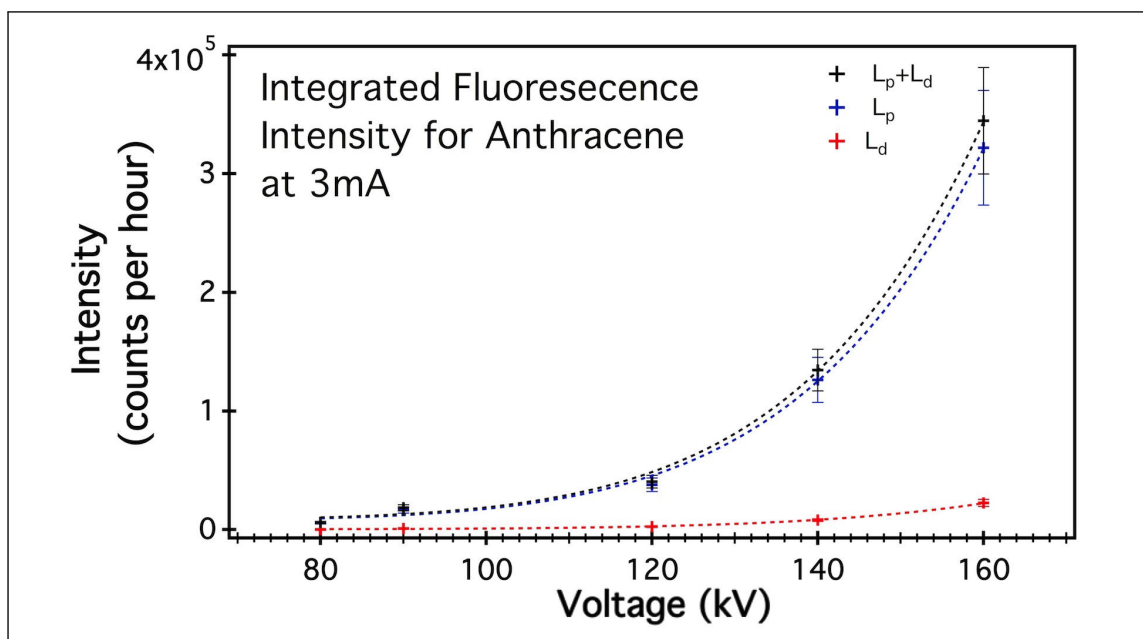


Figure 4.27

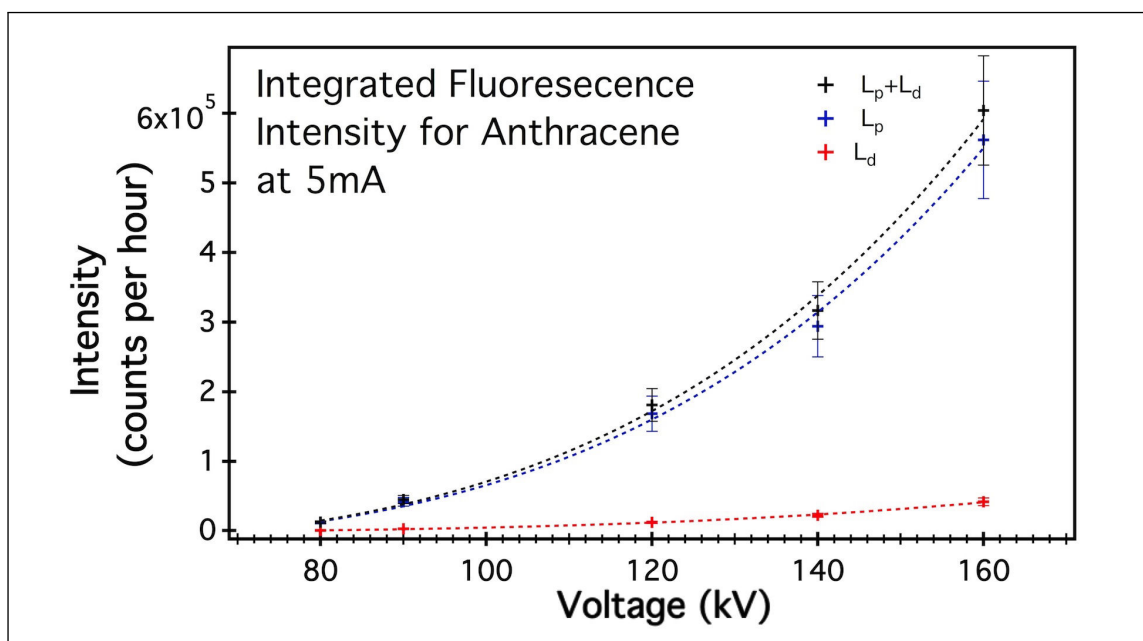


Figure 4.28

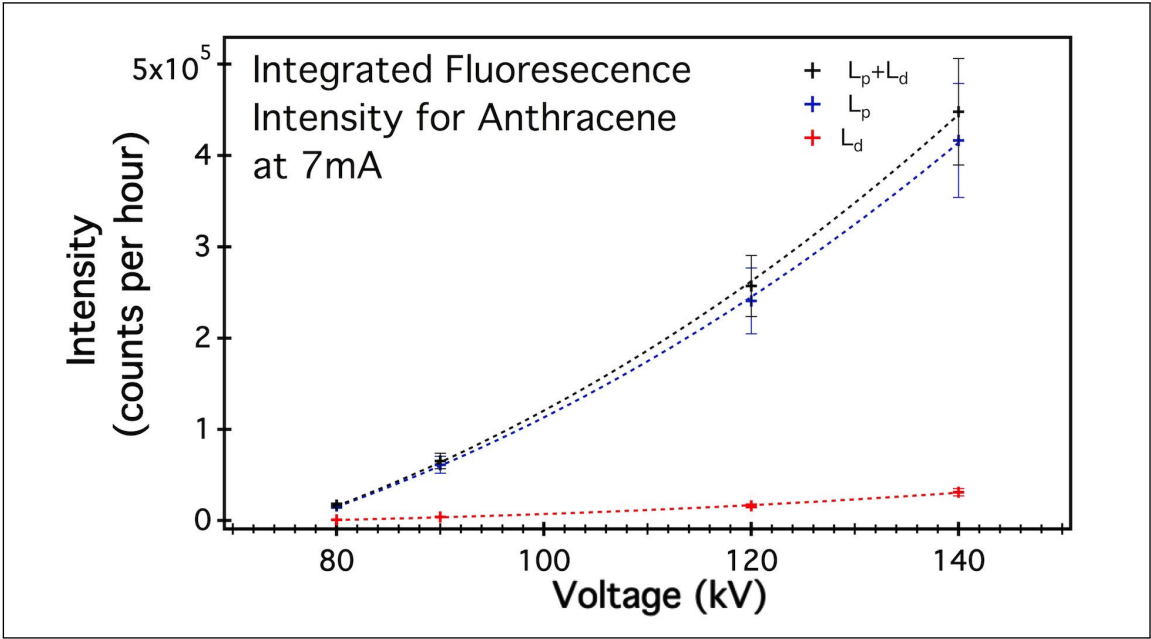


Figure 4.29

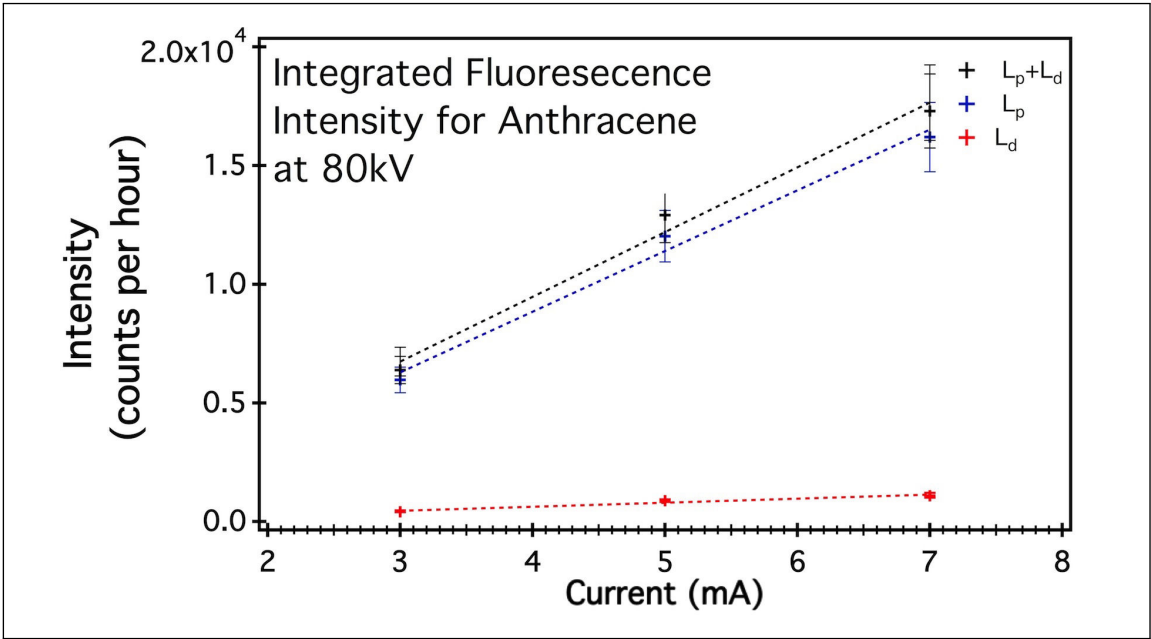


Figure 4.30

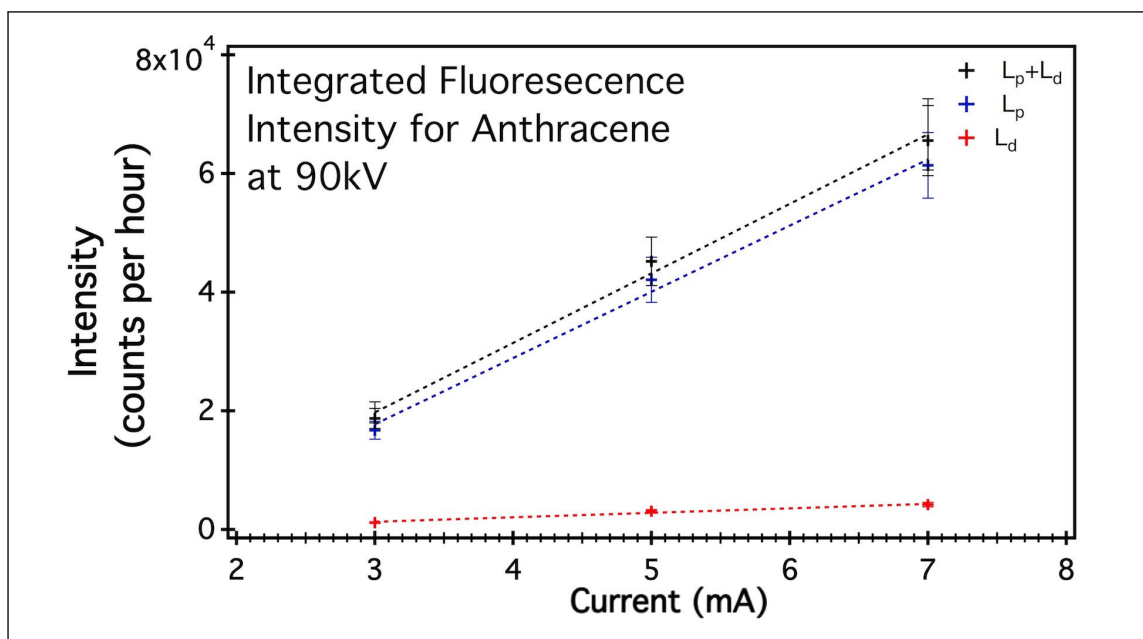


Figure 4.31

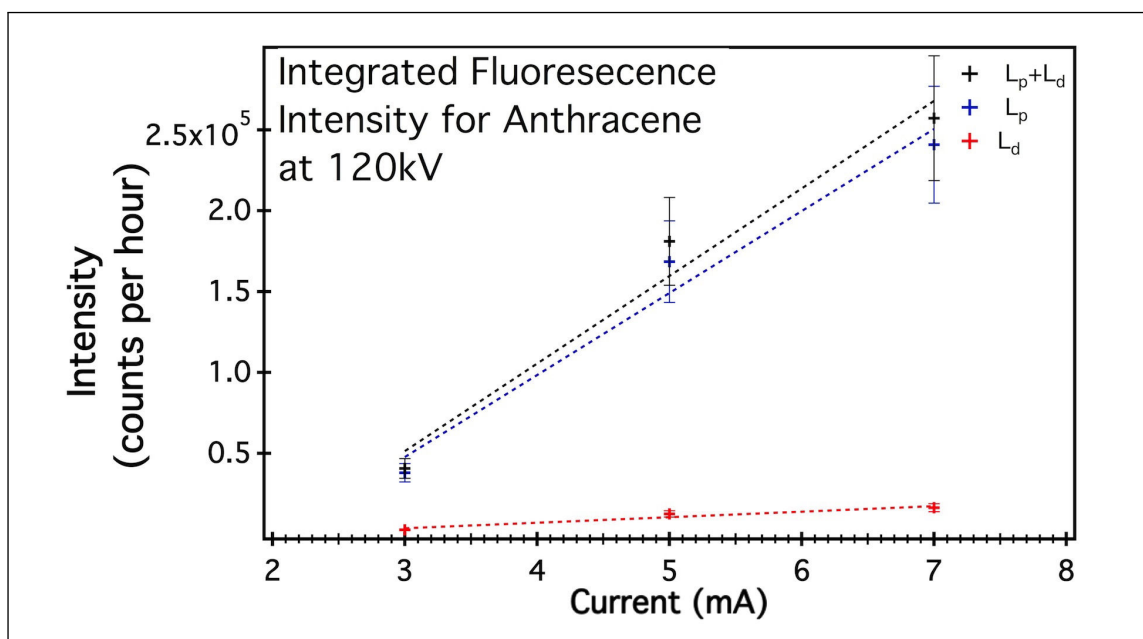


Figure 4.32

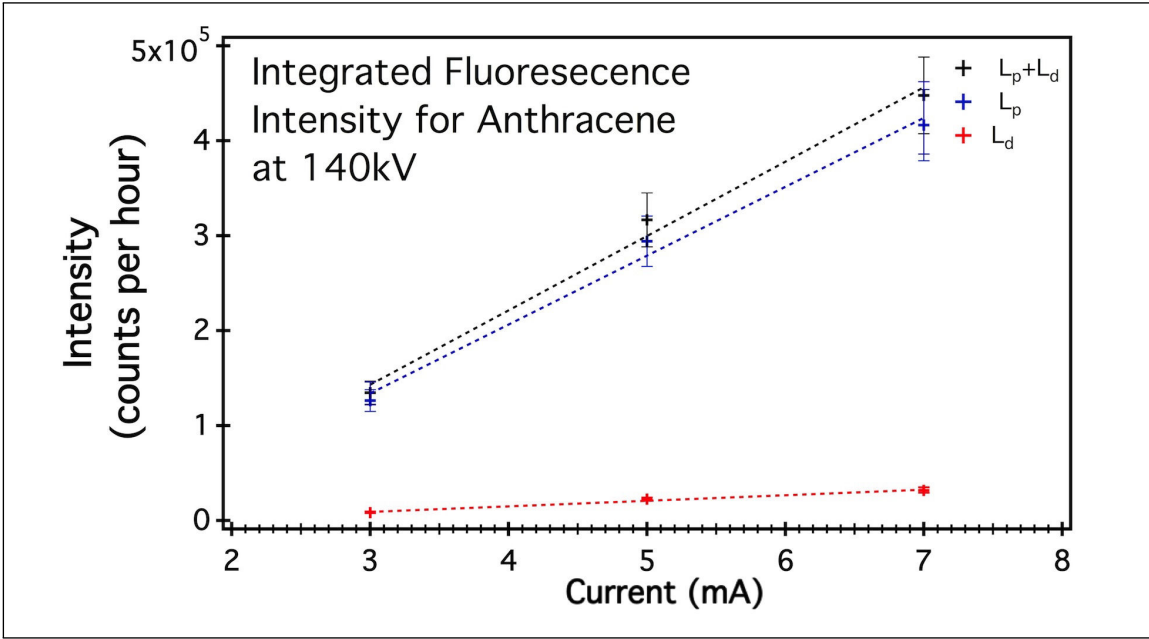


Figure 4.33

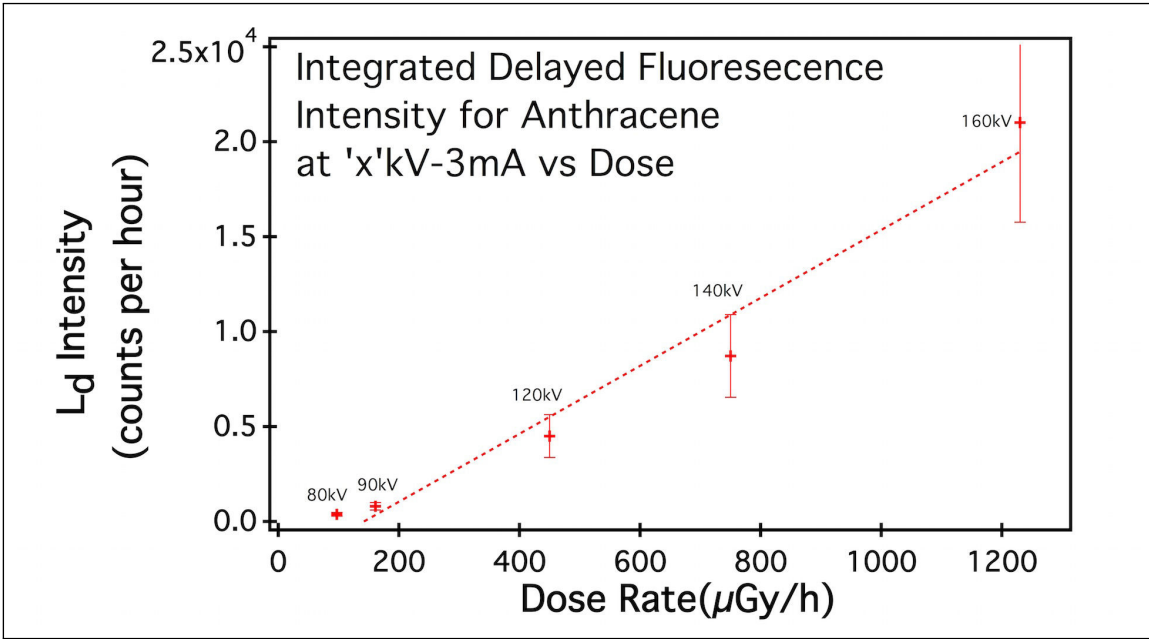


Figure 4.34

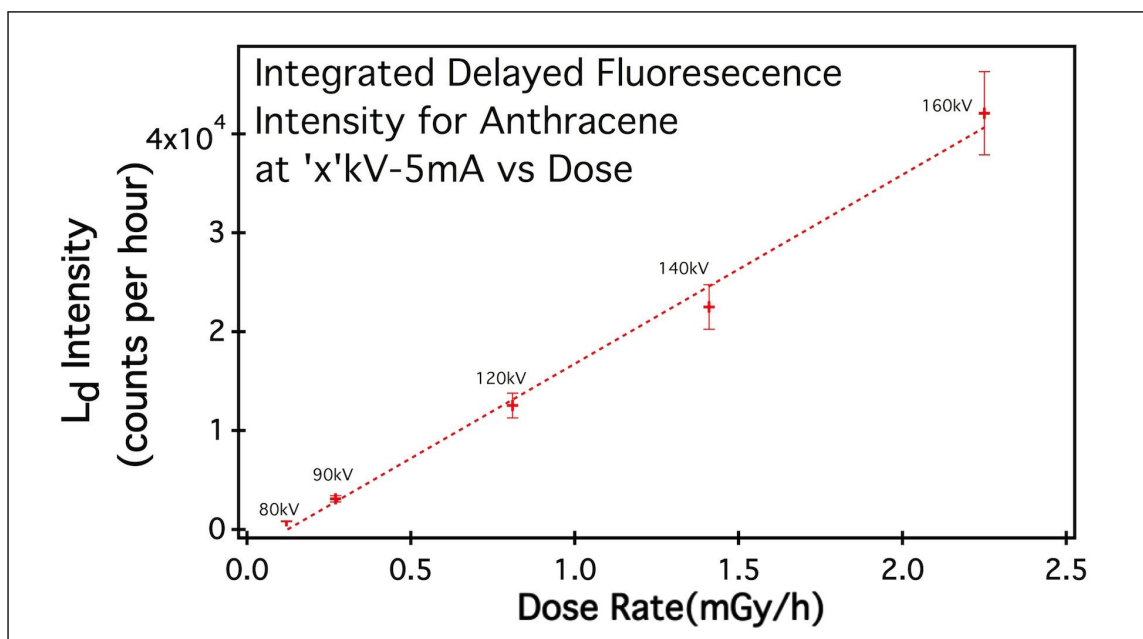


Figure 4.35

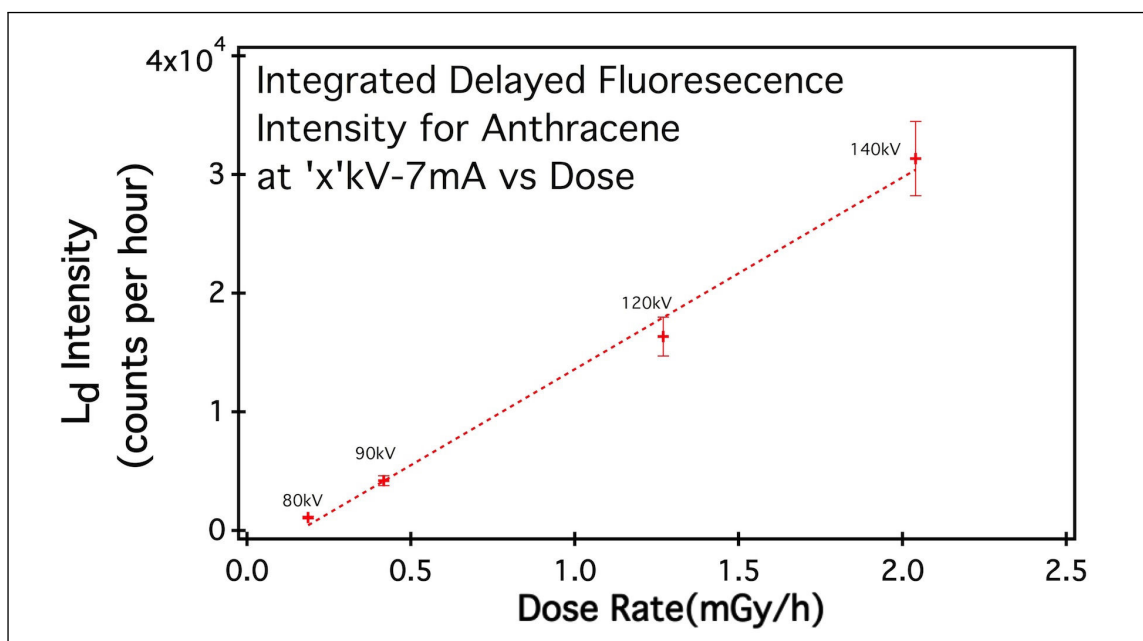


Figure 4.36

*"He aprendido que el mundo
quiere vivir en la cima de la
montaña, sin saber que la
verdadera felicidad está en la
forma de subir la escarpada"*

Gabriel García Márquez

5 Discussions, Conclusions and Perspectives

Discussion

Fluorescence Decay Curves

The Prompt Component

The prompt component is generated by the transition between the vibronic states S_1 and S_0 as explained in Chapter 2 after excitation of the organic scintillator. This excitation may be caused by the primary radiation source as well as secondary δ -electrons. The spontaneous depletion of the S_1 at an instant t after the population of this state, is governed by a first order differential equation with constant coefficients. The solution for this equation is presented in Chapter 2, defined by a mono exponential function, proportional to a constant variable and defined by a decay rate known as the lifetime (τ) of the state S_1 .

The different estimated values of τ were given in the Chapter 4. The experimental values for the lifetimes for p-Terphenyl were consistent with literature values. The literature lifetime values for anthracene vary between 8 ns and around 30 ns according to the different publications (see Chapter 4). The lifetime of anthracene obtained by the TCSPC was around 16 ns, which lies within this range. Moreover, let us recall the lifetime of both our samples were determined with a spectrofluorimeter in agreement with those estimated by the TCSPC.

The fit procedure used to find the lifetime of the different measured decay curves had limits to fit a left tailed Gaussian. It was observed that a longer lifetime would create a fatter left tailed gaussian explained by the fact that the IRF noise was observed by the fluorescence light itself. In consequence, the fit parameters were determined with a lower degree of precision.

Hence, due to the shorter lifetime of p-Terphenyl, better results were obtained.

The Delayed Component

The delayed component has its origin in primary and secondary ionizations of the medium as described in Chapter 2. The notion of dose, presented further on, will be introduced based on this concept.

Ionization is a process where an isolated atom in a vacuum loses one of its electrons and this electron is ejected to the infinite. At that point, the Coulomb field between the ejected electron and atom is equals to zero.

This definition of ionization is ambiguous when talking about a ionization chamber. First, the presence of gas surrounding the ionized molecule leads to the electron thermalization before it escapes to an infinite distance. Second, the gas (dielectric medium) found between the molecule and the ejected electron acts like a screen decreasing the strength of the Coulomb interaction long before the electrons reaches, what it is considered to be, an infinite distance. Thus, a molecule within a gas can be considered as ionized when the Coulomb interaction between the ejected electron has decreased to zero rather than the ejection of the electron to infinity. Then, the electron can freely diffuse to the positive electrode of the chamber generating a response proportional to the deposited energy.

As opposed to molecules in a gas, ionization strongly depends on the existence of free energy states in the medium to receive the ejected electron in dense mediums (solid or liquid). Let us recall the photoelectric effect section in Chapter 1. In the suggested model, the final state was represented by a plane wave corresponding to a free state in vacuum. In a dense medium, this approximation was no longer valid because the final states depended on Pauli's exclusion principle and the notion of effective mass of the electron. For isolators such as anthracene and p-Terphenyl, there are even fewer possible final energy states compared to conductors and semiconductors. This means that there are more available final states in a gas than in a dense state for an ejected electron.

Dense mediums are characterized by their conductivity and this is true for both primary and δ electrons. In consequence, ionization in a dense medium is defined as the transition of an electron from the valence band to the conduction band. The notion of infinity presented before, is even more ambiguous than for molecules in gas state; the distance distribution between electrons and their parent ions is around 10 nm in average[80] regardless the type

of incident radiation. This means that electron is always bounded to its parent molecule creating a geminate pair as described in Chapter 2. The survival probability of the geminate pair is described by Onsager's theory, valid after electron thermalization in the medium. Consequently, this probability depends only on the Onsager's critical radius, the dielectric constant of the medium and temperature. As the Onsager's critical radius is independent of the energy of excitation(primary or secondary), the intensity of the delayed fluorescence is proportional to the number of pairs undergoing recombination. Therefore, as proposed by the cavity theory, Birks and Voltz, the deposited energy depends on the number of electrons generated by ionization, if the recombination yield remains constant and occurs after thermalization.

The recombination kinetics, presented in Chapter 2, described the evolution of geminate pairs in molecular dense media corresponding to the diffusion of a thermal electron, mobile compared to its ion parent, under the mutual Coulomb field. This process gives rise to the fluorescence of recombination observed all along this research. The distribution of geminate pairs at an instant t after electron thermalization as well as the recombination velocity $R(t, E)$,

$$R(t, E) = \frac{1}{\sqrt{4\pi}} \frac{1}{\tau'} \left(\frac{t}{\tau'} \right)^{-3/2} G(E), \quad \tau' = \frac{r_c^2}{D_{e,h}}, \quad (5.1)$$

are determined by an analytical approach solving the Debye-Smoluckowsky equation 2.18. The variable τ' describes the characteristic diffusion time, $G(E)$ the ionization yield and $D_{e,h}$ sum of the electron and hole diffusion coefficients as seen in Chapter 2. The total intensity of the delayed component is given by 5.2,

$$I_d(E, t) = q_f \rho_s N_0(E) R(t), \quad (5.2)$$

where q_f is the quantum yield of fluorescence and ρ_s the density of singlet states at an instant t . This density tends to 25% around 10 ns after the end of the thermalization process[30]. This corresponds to the statistical distribution of spins between the singlet and the three triplet states present in a two spin system. In an organic medium excited by X-rays, the system is 100% singlet after the electron thermalization[81]. The term N_0 corresponds to the number of events considered to deposit energy on the medium for an excitation energy E . This number is proportional to the flux of X photons when there is no saturation of acceptors

in the medium.

It was observed that for any given kV/mA combination set on the X-ray tube and for any type of scintillator (graph 4.22 in Chapter 4), the intensity of the delayed component was governed by 5.2. These results are extremely important because they prove that it is possible to determine a dose integrating the light emitted by delayed component. At first, let us assume that the recombination yield is constant and independent of the incident energy. This assumption will be discussed further on with more detail. Under these conditions, the total light emitted corresponding to the delay component is proportional to the number of electrons generated by the ionization, therefore proportional to the dose rate, as measured by a ionization chamber. The organic scintillator can be then considered as a solid ionization chamber where the recombination fluorescence intensity represents the dose, similar to the charges that create a proportional current to the dose in an ionization chamber. In either case, the measured fluorescence corresponds to the quantity of electrons generated by ionization events within the medium.

kV/mA combination

In the previous Chapter, we presented the results for different kV/mA combinations. The flux of an X-ray tube is given by the following relationship:

$$\Phi(V, I) \propto Z V^2 I, \quad (5.3)$$

where Z is atomic number of the target. It shows that the flux of X photons varies linearly with the X-ray tube current and varies with the square of the X-ray tube voltage.

The Total Delayed Component at Variable Current at Constant Voltage

Results for anthracene are shown in 4.34, 4.35 and 4.36 and for p-Terphenyl in graphs 4.21, 4.22 and 4.23. For the first time, it was observed a linear response between the delayed component of fluorescence of anthracene and p-Terphenyl and the flux of X-ray photons.

The integral of the delayed intensity as presented is given by [41]:

$$L_d = L_d(E; t_1, t_2) = \int_{t_1}^{t_2} i_d(E, t) dt = q_f \rho_s N_0(E) \int_{t_1}^{t_2} R(t, E) dt; \quad t \gg \tau_f \quad (5.4)$$

The function $G(E)$ can be written as G because the excitation energy E is constant. Considering equations 5.1 and 5.2, equation 5.4 becomes:

$$L_d = q_f \rho_s \frac{1}{\sqrt{4\pi}} \frac{1}{\tau'} N_0(E) G \int_{t_1}^{t_2} \left(\frac{t}{\tau'} \right)^{-3/2} dt. \quad (5.5)$$

From the previous relationship, it was deduced that L_d is linear to the number of events responsible of energy deposit, $N_0(E)$, which is in agreement with the experimental analysis. Hence, it was demonstrated there was a linearity between the delayed component and the flux of X-ray photons. Secondary electrons are linear to the incident radiation because the term N_0 takes them into consideration as well.

The Total Delayed Component at Variable Voltage at Constant Current

Let us redefine $G(E)$ presented in relation 5.1:

$$G(E) = \int_0^{E_{kmax}} Y(E, E_k) Q(E_k) dE_k, \quad (5.6)$$

where $Y(E, E_k)$ corresponds to the probability to create a photoelectron (photoemission yield) with initial kinetic energy E_k after molecular excitation with energy E , E_k is the maximum kinetic energy an ejected electron can reach, and $Q(E_k)$, the probability of ionization described by:

$$Q(E_k) = \int_0^\infty \exp\left(-\frac{r_c}{r}\right) h(E_k, r) d\vec{r}. \quad (5.7)$$

The term $h(E_k, r)$ is the distribution of thermalization distances corresponding to the probability of an ejected electron, with energy E_k , to thermalized at a distance r from its parent

Chapter 5. Discussions, Conclusions and Perspectives

ion. The integral in 5.7 is a volume integral; the distances of thermalization are distributed in 3D space within the medium considered as isotropic, hence $\vec{r} = 4\pi r^2 dr$.

Considering both 5.6 and 5.7, equation 5.5 is set to be:

$$L_d = q_f \rho_s \frac{1}{\sqrt{4\pi}} \frac{1}{\tau'} N_0(E) \int_0^{E_{k_{max}}} Y(E, E_k) dE_k \int_0^\infty \exp\left(-\frac{r_c}{r}\right) h(E_k, r) d\vec{r} \int_{t_1}^{t_2} \left(\frac{t}{\tau'}\right)^{-3/2} dt, \quad (5.8)$$

for $t \gg \tau'$.

Equation 5.8 can be simplified considering the discussion in the beginning of this Chapter. We propose two hypotheses:

- To consider that the thermalization radii is extremely small and equal to a mean value given by r_0 .
- The second hypothesis is a consequence of the first one. The kinetic energy distribution transferred to the electrons is given by a mean value E_k ($E_k = E - E_b$ where E_b is the electron's binding energy)

Based on these two hypotheses, we can write $h(E_k, r)$:

$$h(E_k, r) = \delta(E_k - (E - E_b)) \delta(r_0), \quad (5.9)$$

and replacing this equation in equation 5.6 leads to:

$$G(E) = Y(E - E_0), \quad (5.10)$$

and for equation 5.7, we obtain:

$$Q(E_k) = \exp\left(-\frac{r_c}{r_0}\right) \delta(E_k - (E - E_0)), \quad (5.11)$$

and finally, taking into account the relations just described, 5.8 turns out to be:

$$L_d = q_f \rho_s \frac{1}{\sqrt{4\pi}} \frac{1}{\tau'} \exp\left(-\frac{r_c}{r_0}\right) N_0(E) Y(E - E_0) \int_0^\infty \left(\frac{t}{\tau'}\right)^{-3/2} dt \sim N_0(E) Y(E - E_0), \quad (5.12)$$

for $t \gg \tau'$.

This last equation shows the relationship between the total number of events where energy is deposit, $N_0(E)$, and the photoemission yield, $Y(E - E_0)$. The proposed hypotheses, based on very small variations on the transmitted energy to the ejected electron despite the energy of the incident radiation, are very restrictive. Nevertheless, they agree with the study of low energy electrons[82]. Considering the approximation where the variation of $Y(E - E_b)$ can be neglected, we can write:

$$L_d(E; t_1, t_2) \sim N_0(E, t), \quad (5.13)$$

for $t \gg \tau'$, meaning that our device is a proportional counter as the ionization chamber, which is in agreement with the cavity theory. From a fundamental point of view, the proportional counting is due to local deposit of energy, so the response depends on the number of these events, and not on the initial energy. Consequently, the experimental observation is in agreement with 5.3.

A posteriori, the hypotheses about energy deposition and constant thermal distances are validated. This approach helps understand the interaction between matter and the incident radiation here studied.

The Total Prompt Component

The response of the prompt component was similar to the delayed one and depended on the secondary electrons as well. To our knowledge, there were no other documents or articles concerning this subject.

Experimental results showed that the prompt component L_p behaved as the delayed component L_d , for constant current and variable voltage combinations as well as for and constant

voltage and variable current combinations. This led us to conclude that the response of the organic scintillator is similar to the response of the ionization chamber when measuring a dose and let us use the Voltz model to give a first idea to explain this process.

Let us recall that equation 2.53 defined the total prompt component emitted by the organic scintillator. It depended on a quenching term B_0 among others. Obtained results made us believe that there could be probably no quenching, meaning that B_s is equal to zero and letting us write again 2.53 as :

$$\frac{dL_p}{dx} = \frac{q_s}{W_s} \frac{dE}{dx}. \quad (5.14)$$

Another approach to understand the results was to consider the proportional response of the organic scintillator. This meant a constant deposit of energy regardless its origin (X-ray or δ electron), hence dE/dx constant. In other words, the deposited energy would fill the same molecular excitation energy level S_n . The term $\exp[-B_s(dE/dx)]$ in equation 2.53 was considered to be constant as well. As the stopping power is constant for both primary and secondary excitation processes as well, equation 5.14 can be rewritten as :

$$\frac{dL_p}{dx} = \text{constant} \quad (5.15)$$

It is important to remark that the proportional response of the scintillator did not change with or without quenching. This was once again in agreement with the proposed hypothesis of low energy deposit and low molecular excitation for both primary and secondary excitation. This relation between excitation and deposited energy allows us to consider the organic scintillator as a *proportional excitation chamber* for the first time as to our knowledge, this has never been observed in the past.

We have shown based on the analysis and discussion of the results obtained during this research, that it is possible to measure an excitation dose. Having access to this measurement is important knowing that the effects of excitation cannot be measured by an ionization chamber; this effects can cause molecular damage such us dissociation, free radical formations or chemical reactions with neighboring molecules. Generally, the state S_1 posses a gap of around 4eV, which can not be measured by an ionization chamber. This is also valid for ionization as the ionization energies for an organic scintillator is around 8 or 9eV.

Ratio $R = L_p/L_d$

The ratios of L_p/L_d for anthracene (~ 4.37) and p-Terphenyl (~ 14.06) are shown in the Table section in Chapter 4. The difference between these ratios may be explained by the difference in their lifetimes. Anthracene has a longer lifetime. Hence, the total prompt component is larger than the prompt of p-Terphenyl. Once this ratio R is known for a scintillator, it would be possible to determine the L_p or the L_d component just by knowing only one of them or vice versa as well as the total fluorescence $L_p + L_d$.

Dose-Luminescence Relation

Graphs 4.19 to 4.21 and from 4.32 to 4.34 showed the linearity between the total delayed fluorescence and a calibrated Babyline 81 for p-Terphenyl and anthracene respectively. These results showed that the scintillator behaved like a proportional counter as previously discussed. No comparison was done between the total prompt component and calibrated dosimeter because they do not exist. Nevertheless, a linear relationship between prompt and delayed component was observed.

The linear response of organic scintillators do not make them absolute dosimeters. First, the yield of recombination is lower to 100% (except for anthracene) for the delayed component. Regarding the prompt component, a dose can be estimated only under no quenching or if the quenching remains constant during the whole excitation de excitation processes.

The use of organic scintillators for absolute dose measurements may turn out to be a very challenging and difficult task and several aspects should be taken into account. Let us first consider a molecule in the S_n state; it can de excite in two different ways for the same deposited energy: internal conversion which leads to the prompt fluorescence and autoionization leading to the delayed component of fluorescence. If quenching is considered, the scintillator may have a third possibility to de excite increasing the level of complexity of the system. Finally, one should consider there is no primary direct ionization as well. Only secondary electrons would create S_n states responsible for generating the prompt component.

Conclusions and Perspectives

The response of two different organic scintillators to X-rays with energies between 80kV and 140kV at different X-ray tube currents was studied. A systematic study was done for

p-Terphenyl and anthracene in order to determine if organic scintillators could be used to determine a dose in the X-ray imaging most precisely.

In order to acquire all the fluorescence decay curves an experimental platform, based on the Time-Correlated Single Photon Counting technique, was mounted for this research. This kind of setup had never been used to acquire decay curves under a continuous source of X-rays, which implied a certain degree of risk. The originality of the experiment was to replace the excitation source generally used in the TCSPC by a second photomultiplier tube to acquire the luminescence. A lot of work and ingenuity were required to overcome technical difficulties and then set up the experiment to acquire coherent and consistent experimental data. It is important to remark that no saturation was noticed in the results. This means that saturation observed in other studies may be caused by the instrument and not by the scintillator itself.

One of the most original results obtained in this work are about molecular excitation. For the first time ever, it was observed that the excitation response of an organic scintillator was similar to that of a proportional chamber, results which gave us the idea to name the scintillator a *proportional excitation chamber*. It was also observed that the temporal evolution of the experimental delayed component was coherent with theory (t^{-n}). The delayed component was proportional to the ionization chamber as reflected by the comparison of the delayed component to an ionization chamber. This evidenced the linear response of an organic scintillator to X-rays.

The constant ratios between the total prompt and delayed fluorescence found in this work for both anthracene proved that luminescence depends only on the nature of the scintillator and not on energies of the X rays used in this work, being this in agreement with the hypothesis.

From a fundamental point of view, the proportional response of the studied scintillators was explained because the distance of thermalization for the second electron had a constant average value and it was independent of the incident energy. Therefore, it is the vibronic states of the scintillators that governs the process of energy deposition within the scintillator and its de excitation. All these processes occur at low energies of around 30eV. We observed as well the very important role that plays quenching on the estimation of the dose by organic scintillators.

Even if at the end we were not capable to demonstrate or giving any scientific proof and only based on the experience and knowledge gained throughout this research, we would like to say that we strongly believe that the deposited dose from excitation processes should not

be neglected in dosimetry. We consider that further research is needed in this domain and to consider, if proven relevant, to add the notion of excitation dose to international standards.

A Poisson Counting

In 1837, the French mathematician Siméon Denis Poisson discovered a the probability distribution which is named after him. It is used to find the probability of an event X to occur (or not) in a given interval of time. The Poisson probability distribution function for a random discrete positive variable X is given by :

$$P(X = k) = \frac{\lambda^k e^{-\lambda}}{k!}, \quad (\text{A.1})$$

with mean and variance :

$$E(X) = \lambda \quad V(X) = \sigma^2 = \lambda \quad (\text{A.2})$$

The conditions to use this distribution are : the number of n time intervals is indefinitely large; p , the probability of success of an event in any given interval is extremely small ; $\lambda = np$ should be finite where λ is the number of occurrences per unit of time. In graph A.1 different values of λ are traced.

Limiting Cases

- For values of $n > 20$ and $p < 0.05$, the Binomial distribution is approximated by the Poisson distribution.

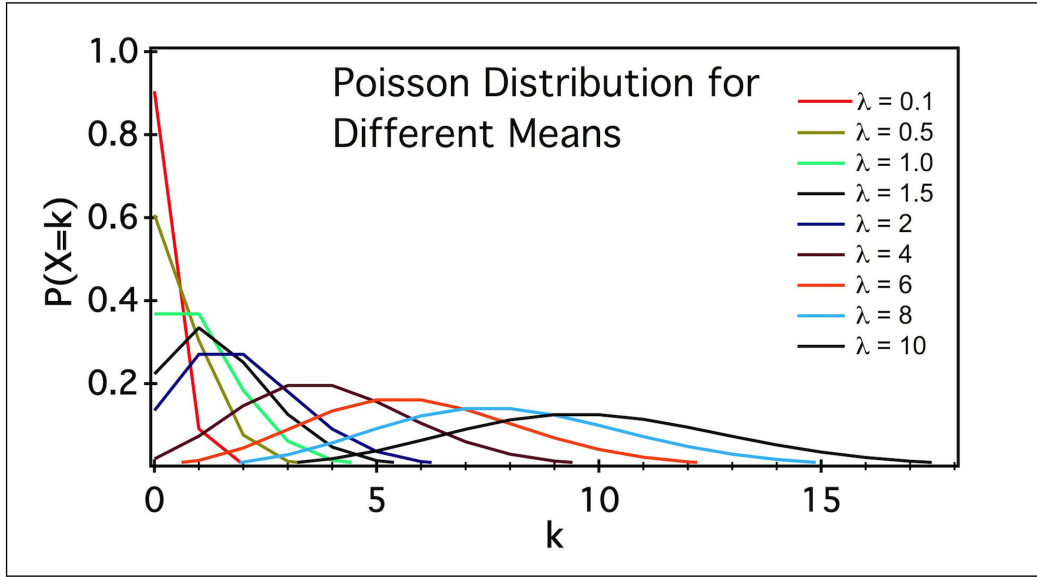


Figure A.1 – The Poisson Distribution for different values of λ

- The Binomial distribution is correctly described the Gaussian distribution if $0.2 < p < 0.8$ and $n > 25$. Therefore, for large values of λ , the Poisson approaches the Gaussian distribution.

Poisson Distribution in Experimental Counting Example

The Poisson statistics fit many different experiments where single independent events must be counted. Let us define Δt and a time interval and λ the expected value of an event to occur within the interval. Let us now divide λ by Δt to obtain a rate r . The probability of observing exactly k events is now:

$$P(X = k) = \frac{(r\Delta t)^k e^{-r\Delta t}}{k!} \quad (\text{A.3})$$

The value of λ is given by :

$$\lambda \approx \bar{k} = \frac{1}{N} \sum_i k_i m_i, \quad (\text{A.4})$$

where m_i is the number of measurements with k_i value and N , the total number of measurements. At the same time, the standard deviation(SD) σ is

$$\sigma^2 \approx s^2 = \frac{1}{N} \sum_i m_i (k - \bar{k})^2 \quad (\text{A.5})$$

The SD of \bar{k} , it is just the SD of the mean and the SD of s^2 , σ_{s^2} , is given by :

$$\sigma_{\bar{k}} = \frac{\sigma}{\sqrt{N}} = \frac{s}{\sqrt{N}} \quad (\text{A.6})$$

$$(\sigma_{s^2})^2 = \sum_i \left[\frac{\partial(s^2)}{\partial k_i} \right]^2 \sigma_{k_i}^2 \quad (\text{A.7})$$

when all σ_i are the same, relationship A.7 simplifies to:

$$(\sigma_{s^2})^2 = \frac{4}{N} \sigma^2 s^2 \approx \frac{4}{N} s^4, \quad (\text{A.8})$$

B TPCSP Modules

A brief description of some of the most important characteristics of the components for the TCSCP setup.

The Constant Fraction Discriminator (CFD)

The CFD is an electronic device capable of processing signal with extremely fast rise times. Regardless the jitter and slope of the input signal, the CFD generates output signal at the same time t_0 determined by a user set signal threshold. Timing is then independent of the input signal which is very important for precise time measurements.

In order to understand how the CFD works, let us start by defining S as the input signal and V_{th} the wanted threshold set by the user. The procedure is the following :

- The time t_d between the beginning and the maximum amplitude of S is measured.
- S is duplicated, inverted and its amplitude reduced to $-V_{th}$ generating S_2 .
- The original S is delayed 30% of t_d generating an S_d signal.
- S_d and S_2 are added and at the point both signals cross zero, the output impulse is generated.

Signals with different rise times processed by the steps above described, will generate and output impulses at the same time, t_0 . This electronic conditions are ideal for extremely precise time measurements, as it is the case of the TCSPC. Nevertheless, the constant fraction signal treatment is more time consuming than other discriminating modes such as *leading*

edge. The advantage of this mode is a faster signal treatment though precision about the starting time t_0 is lost due to the jitter.

The Time-to-Amplitude Converter (TAC)

The TAC is fed by two different signals. The first signal, called the START signal, generates a linear voltage ramp that will charge a capacitor. The capacitor charges until a stop signal is detected. If there is no STOP signal the capacitor is emptied, hence resetting the TAC. Figure B.1 depicts how a TAC works. Usually, the TAC has a full of scale of 10V allowing the user to set the time range needed by the user. Depending on the model, the full time range can vary from $100ns$ to $10\mu s$ full scale according to the experimental needs. The resolution of such a device is of high precision and allows to obtain very precise time outputs (of around several hundred ps)

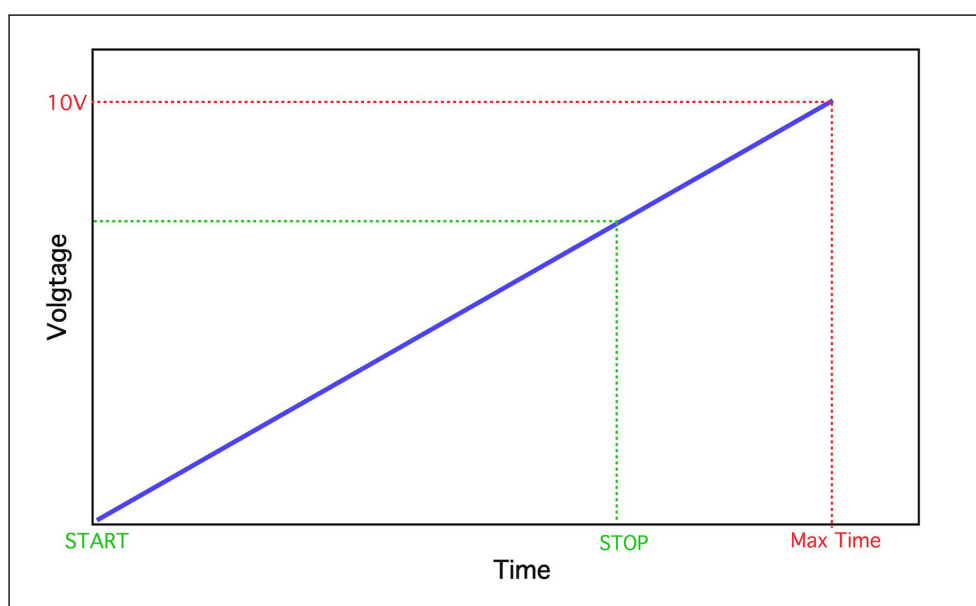


Figure B.1 – Principle of the Time-to-Amplitude Converter

The Multichannel Analyzer (MCA)

The MCA is a device capable of sorting out voltage pulses according to their heights and assigning each of them a memory bin. Every time an event is recorded it is stored to its corresponding bin. The height of each bin in the histogram is directly proportional to the number of events registered by the MCA. They are commonly used to reconstruct energy or

time related data in the form of histograms. Figure B.2 shows an histogram registered by an ORTEC EASY-MCA and displayed by MAESTRO[®] used during my research.

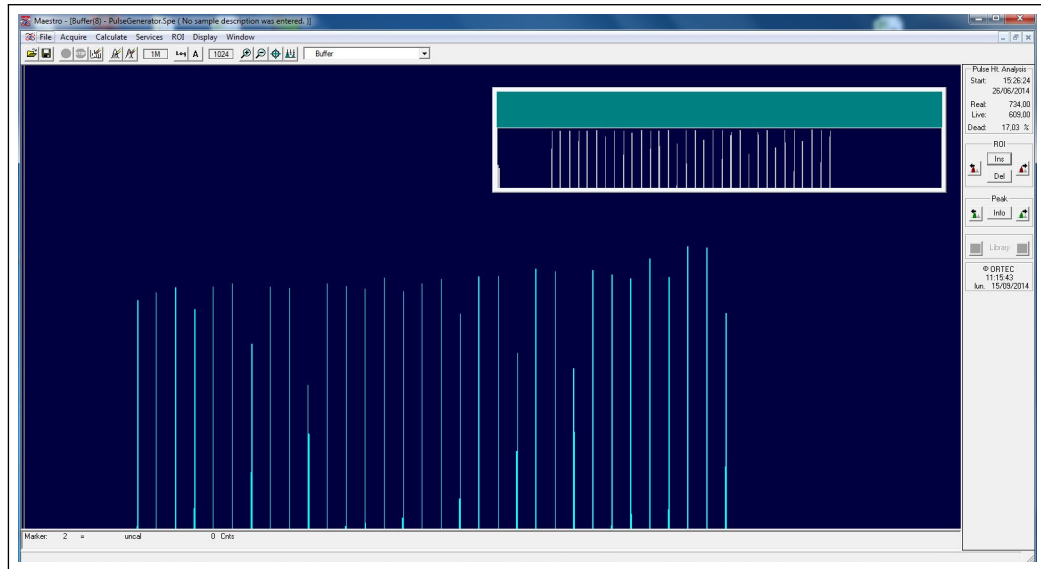


Figure B.2 – This histogram was generated using an ORTEC Time Calibrator. The range and the period can be set to test the performance of the MCA.

C EMG Fit Before the Fluorescence Peak

V.B. Di Marco and G. G. Bombi[79] studied many different ways to fit chromatographic peaks among the EMG function, which turned out to be one of best options to fit the convolution between exponential and gaussian functions. They also discussed the inaccuracy of the EMG to fit the curve before the peak as mentioned in Chapter 4. They explained the difference between the EMG fit and the experimental data.

During the testing phase of the different electronic components of the experimental setup, an an ORTEC 462 Time Calibrator was used to generate random START and STOP impulses. This time calibrator produces a fast negative output with an accuracy of 10ps for a 10ns period. At first, the OUTPUT signals were fed directly to the TAC. The TAC output signal went to the MCA and the finally to the PC, exactly the same setup used in the TCSPC technique. Results were considered satisfactory with the obtained time resolution of 2 ns per peak.

Then we focused the behavior of the CFD. The output signals or the time calibrator were fed into the two different CFD and the electronic chain from there on was the same as for the TCSPC. First, the Leading-Edge(LE) mode of the CFD was tested. This discriminating mode allows to set a threshold regardless the rising time of the signal. In consequence, the timing results are less accurate though the electronics are faster. Results were as expected and it can be seen in figure C.1. For obvious reasons, the LE discrimination is not adequate for fluorescence lifetime measurements.

The constant fraction discrimination mode was chosen next. As expected, time measurements was extremely accurate represented by very high resolution peaks as seen in figure C.2. A left tailed peak was observed too though it was small when compared to the height of the peaks. This source of electronic noise is responsible to a certain extent of those extra

Appendix C. EMG Fit Before the Fluorescence Peak

counts observed at the left of the peak in experimental data.

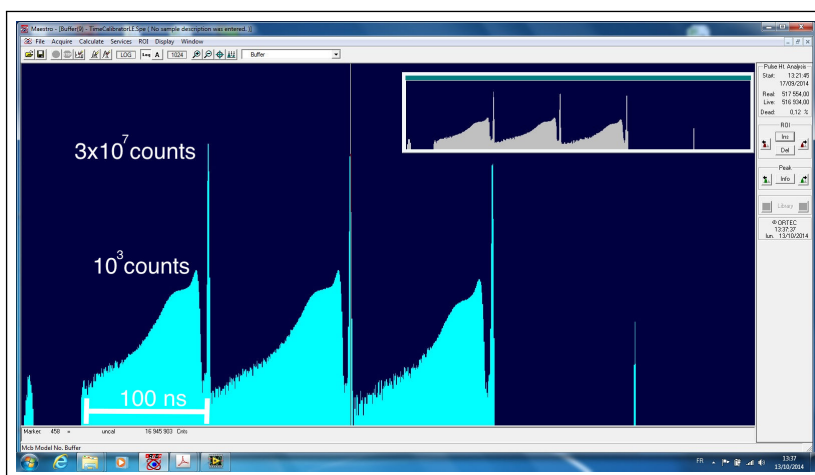


Figure C.1 – A 10-base log scale is used for the Y axis - There are four orders of magnitude between the expected maximum peak and a second peak that tails for around 100 ns.

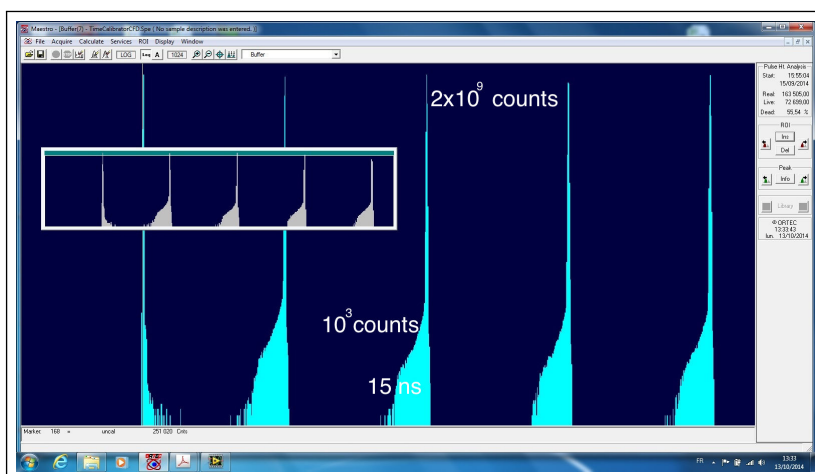


Figure C.2 – A 10-base log scale is used for the Y axis - The peak of the tail is 7 orders of magnitude smaller than the peak tailing for some 15 ns.

Theoretically, one should expect a unity bin resolution peak as it is the signal that is generated by the Time Calibrator. Experimentally, both the CFD and LE mode disturb the timing resolution. The LE mode generates around 100 times more noise than the CFD mode with a tailing peak 6 times bigger. We can conclude that the LE mode may be faster than the CFD mode though it is not compatible for experiments needing a very precise time resolution, such as the TCSPC.

Résumé

Introduction

Depuis la découverte des rayons X, par Wilhelm Röntgen en 1895, et leur application immédiate à l'imagerie médicale, de nombreuses études ont été menées afin de mieux comprendre les mécanismes d'interaction de ces rayonnements avec la matière, ainsi que les effets physiques, physico-chimiques, chimiques et biologiques qui en découlent. Ces études, toujours réalisées dans le but premier de mieux contrôler la dose délivrée au patient, ont d'abord été motivées par l'apparition d'accidents de surirradiation, lesquels sont survenus quasi immédiatement après les premières utilisations des rayons X par Röntgen. Plus tard, avec l'avènement de la radiothérapie, puis de l'imagerie tomodensitométrique, les études sur le contrôle des doses déposées se sont développées afin d'atteindre une compréhension de plus en plus fine de la relation dose effet. Aujourd'hui, avec la multiplication des examens d'imagerie et des actes de radiothérapie, la connaissance de la dose délivrée à un patient est devenue un enjeu de santé publique. Il devient donc, plus que jamais, nécessaire de s'atteler à de nouvelles études fondamentales, à la fois théoriques et expérimentales, de manière à parvenir à une représentation plus précise du phénomène de dépôt de dose, particulièrement à l'échelle microscopique et, conjointement, de développer de nouveaux instruments capables d'accéder en temps réel et in situ à la dose délivrée lors d'un acte, notamment par la recherche de nouvelles observables physiques. Le travail présenté dans ce manuscrit a été réalisé dans cet esprit et tente d'apporter de nouvelles réponses, à la fois fondamentales et expérimentales, à la question particulièrement importante de la mesure d'une dose de rayons X médicaux à l'échelle de la molécule et de la relaxation au milieu irradié de l'énergie initialement déposée. Le travail présenté est à caractère interdisciplinaire. Il fait essentielle-

ment appel au langage de la physique de l'interaction rayonnement matière, de la physique moléculaire et de la physique de la matière condensée dans les aspects fondamentaux du dépôt de l'énergie primaire et de sa relaxation au milieu irradié. L'observation expérimentale fait appel à l'utilisation de matériaux modèles scintillants, équivalents tissus, qui sont étudiés d'un point de vue physique et physico-chimique dans le but de relier un dépôt de dose à l'échelle moléculaire à une émission de fluorescence. Un soin particulier est apporté à l'étude de l'ionisation, en tant qu'observable principale en dosimétrie, mais aussi, et c'est la première originalité de ce travail, à l'excitation moléculaire dont l'existence, lors d'une mesure de dose, est toujours négligée. Au-delà des aspects fondamentaux étudiés, la seconde originalité de ce travail repose sur la détermination de la dose déposée par l'observation expérimentale, en résolution temporelle nanoseconde, d'un signal de fluorescence. Ce type d'approche n'avait jamais été tenté. Pour cela, une nouvelle instrumentation a été spécifiquement développée, basée sur la détection de photons uniques corrélés en temps sous flux continu d'irradiation. Cette instrumentation, unique, permet aujourd'hui de s'affranchir d'une source de rayonnement impulsionnelle pour l'observation d'un signal temporel, ce qui ouvre la porte aux études temporelles in situ à l'aide de générateurs de rayons X médicaux standards.

Chapitre 1

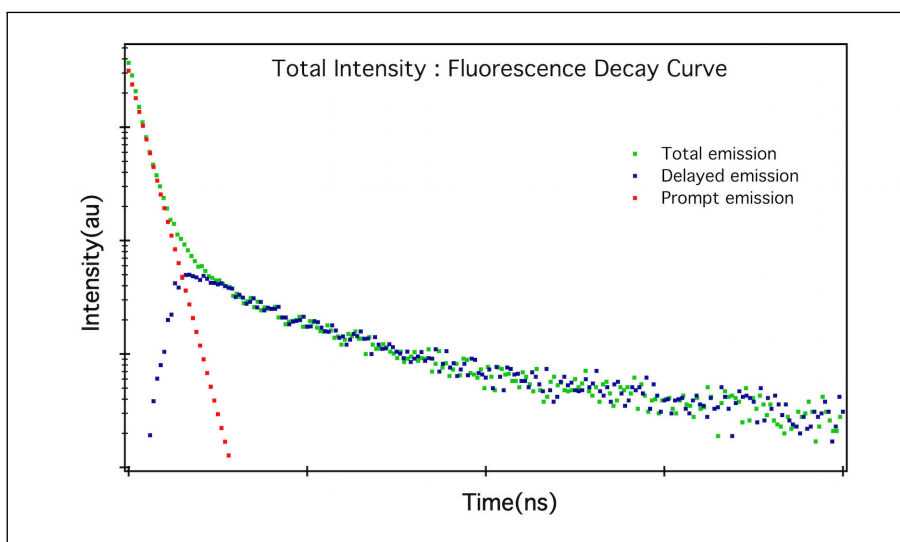
Aspects fondamentaux de l'interaction rayonnement matière

Le premier chapitre du manuscrit est consacré aux aspects fondamentaux de la dosimétrie X par mesure de fluorescence. Il se fonde en premier lieu sur les connaissances théoriques actuelles en matière d'interaction rayonnement matière, dans le cas des photons, afin de traiter aussi bien de l'interaction primaire que des pertes d'énergie des électrons secondaires. Un lien direct est ensuite établi, dans le cadre des modèles de Birks (1) et de Voltz (2), entre les différentes pertes d'énergie secondaires et la quantité de luminescence émise. Une première partie, théorique, consacrée à l'étude du couplage du champ d'irradiation X avec la matière, détaille l'interaction d'une onde électromagnétique avec le milieu représenté par une charge dans l'approximation d'une liaison faible devant l'énergie de couplage. Dans une première étude, l'hamiltonien du système intéressant fait l'objet d'un traitement semi-classique en perturbation conduisant à l'expression de la section efficace de transition dans l'approximation dipolaire entre deux états liés. Dans une seconde étude, on traite de l'ionisation par effet photoélectrique, particulièrement importante en dosimétrie, correspondant à une transition entre un état faiblement lié d'un électron du milieu et un état quasi-libre de celui-ci dans ce même milieu. L'effet Compton est également abordé. Une troisième et dernière étude, consacrée aux électrons secondaires, vecteurs importants de l'énergie initialement déposée par le rayonnement X, rappelle l'approche de Bethe-Block du pouvoir d'arrêt des particules chargées légères dans un milieu continu.

Chapitre 2

La scintillation organique

Le chapitre 2 est consacré à une analyse originale de la relation dose luminescence. Dans un premier temps, on y décrit le déclin de fluorescence qui peut toujours être décomposé en deux contributions: la première, dite rapide ou prompte, trouve son origine dans les excitations directes d'états liés vibroniques du fluorophore, suivie par une relation non radiative conduisant au peuplement d'états singulets scintillants, ou, dans le cas d'un scintillateur dilué, dans les transferts d'énergie intermoléculaires homo ou hétéropolaires ; la seconde, découle de la formation de paires électron trou géminées, par autoionisation de la phase dense, donnant naissance à une composante dite lente, ou différée, par fluorescence de recombinaison.



Déclin de fluorescence en fonction du temps. L'intensité total du déclin (ligne verte) est la somme de la composante rapide (ligne rouge) et de la composant retardée (ligne bleu). La composante rapide a comme origine des phénomènes d'excitation[29] et la composante lente est expliqué par les interactions entre les spins du système ou par des phénomènes de recombinaison [37, 38]

Dans un second temps, on explicite de manière détaillée la relation existant entre dose et luminescence spécifique au travers du modèle simple de Birks établi dans les années 1960. Un troisième temps est consacré au modèle de Voltz, le plus développé du domaine. Nous en faisons une analyse complète et détaillée en vue de son utilisation, moyennant quelques discussions et modifications, dans l'analyse de nos futurs résultats.

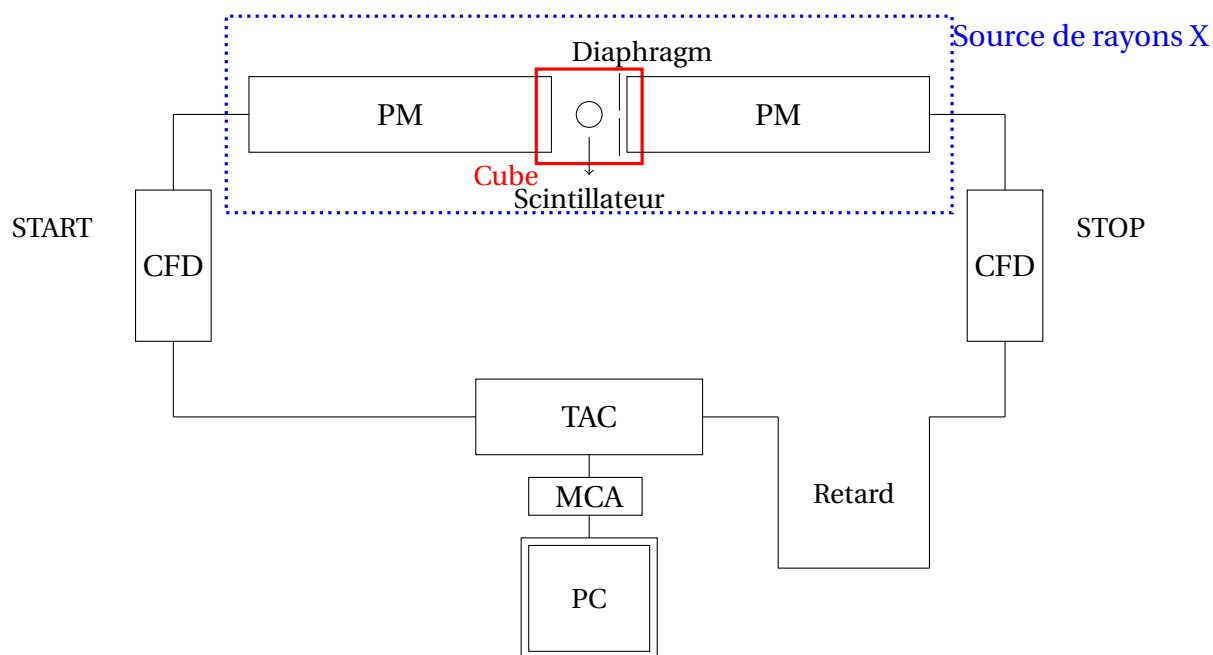
Chapitre 3

Le montage experimental

Le troisième chapitre est consacré aux aspects expérimentaux de la mesure de fluorescence émise par un matériau scintillant lorsque celui-ci est irradié par des rayons X sous flux continu. Une expérience originale a été spécifiquement construite pour cette thèse. Basée sur la mesure, en coïncidences, de photons uniques corrélés en temps en résolution nanoseconde (Time-Related Single Photon Counting technique, figure **Le montage experimental**), elle permet de relever le déclin de fluorescence de n'importe quel scintillateur en s'affranchissant de la nécessité d'une source d'excitation pulsée et ceci, en éliminant, par principe, tout bruit de fond. Utilisant deux photomultiplicateurs au lieu d'un seul, contrairement à tous les autres systèmes actuels de dosimétrie par fluorescence, cette expérience permet aussi d'éviter toute saturation de la détection avec l'intensité lumineuse, les détecteurs ne fonctionnant pas en mode intensité.

Ce chapitre est construit de manière à décrire en détail l'ensemble des systèmes avec comme point de départ l'observable physique intensité de fluorescence. Une description des détecteurs (photomultiplicateurs UV – faible bruit) est suivie par une présentation de l'ensemble de la chaîne électronique d'acquisition, précisant les limites de celle-ci et les réglages utilisés pour les expériences. On y réalise également une étude complète des paramètres d'excitation (description de la source RX utilisée et de la cellule expérimentale et présentation de la chambre d'ionisation utilisée pour déterminer la dose), des échantillons (scintillateur), et de détection (étude théorique du principe de la détection en photoélectron unique). Cette étude est la première du genre en dosimétrie X. Elle permet la validation d'une approche expérimentale nouvelle en dosimétrie et montre qu'une réponse linéaire de la mesure de scintillation est possible en régime de photoélectron unique sous certaines conditions particulières.

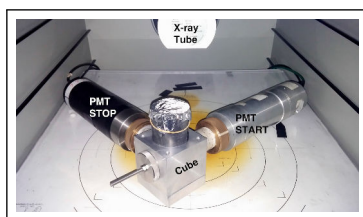
Schème et photographies de l'expérience:



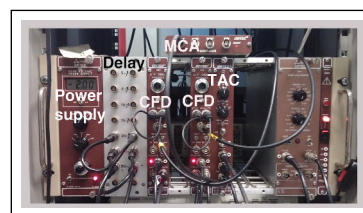
Le montage expérimental - Le scintillateur est placé à l'intérieur du cube pour isoler les deux photomultiplicateurs (PM) de la lumière. Le PM START sert à démarrer l'électronique tandis que le PM STOP l'arrête. Le temps écoulé entre ces deux signaux est utilisé pour la reconstruction statistique du déclin. Chaque signal sortant du PM est envoyé à un discriminateur à fraction constante (CFD) pour adapter les signaux électroniques au convertisseur temps-amplitude (TAC). C'est dans le TAC que les différences temporelles entre le START et le STOP sont mesurées pour finalement stocker l'information dans un histogramme à l'aide d'un analyseur multi-canaux (MCA). Un ordinateur (PC) est utilisé pour régler le MCA et afficher les résultats.



Source de rayons X.



Le système de détection placé à l'intérieur de la source de rayons X. On observe le tube X, les PM START et STOP et le cube.



Electronique permettant mesurer les signaux PM, de le traiter, de mesurer l'écart temporel entre les deux signaux et de le stocker.

Chapitre 4

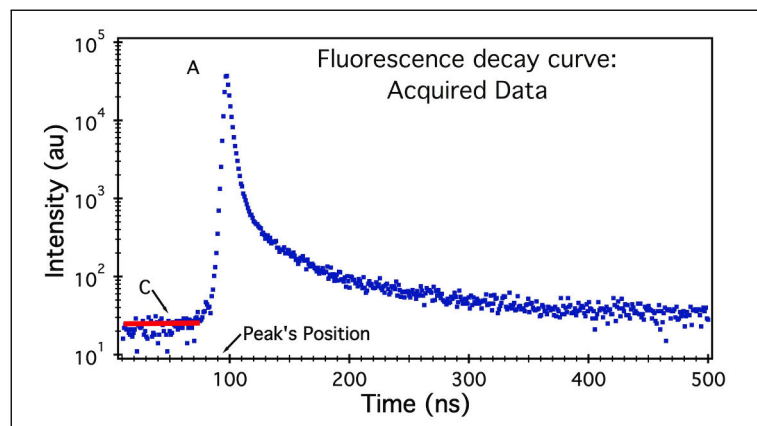
Les résultats

Ce chapitre est consacré à la présentation des résultats expérimentaux. L'objectif de ce chapitre est à la fois fondamental, par l'étude de scintillateurs modèles (p-terphényle et anthracène) utilisés en détection nucléaire et leur utilisation pour la dosimétrie des rayons X, et appliqué, par l'étude concomitante d'une fibre optique scintillante industrielle dopée avec ces mêmes scintillateurs.

Après une introduction décrivant le plan d'expérience et ses motivations, on présente la modélisation des déclin de fluorescence, incluant la convolution du signal observable avec la fonction d'appareillage et basée sur une gaussienne modifiée par une exponentielle, permettant de retrouver les composantes rapides et lentes de fluorescence. Le déclin de fluorescence est modélisé à l'aide de l'équation suivante :

$$y(t) = C + \frac{A}{2} \exp \left[\frac{\sigma^2}{2\tau^2} - \frac{t - \mu}{\tau} \right] \left[1 + \operatorname{erf} \left(\frac{t - \mu - \frac{\sigma^2}{\tau}}{\sigma\sqrt{2}} \right) \right],$$

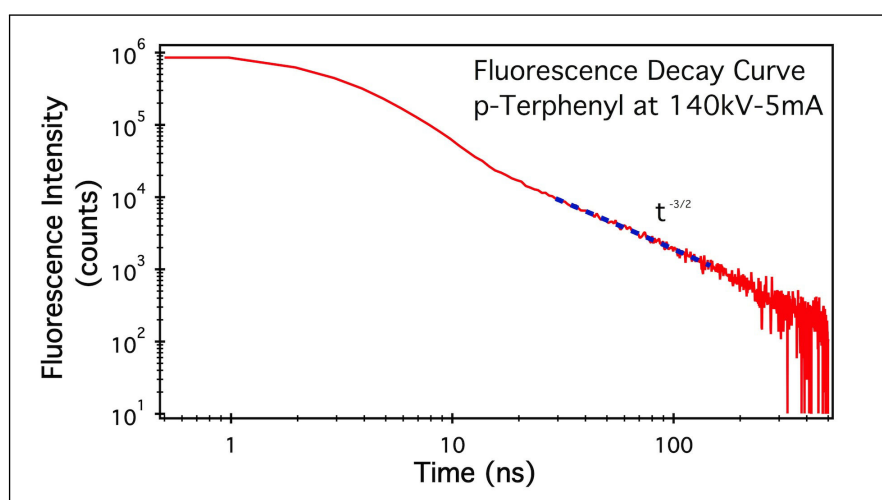
Les paramètres A , C et μ sont estimés, dans un premier temps, par simple observation du déclin de fluorescence (figure **Déclin de fluorescence**) et les paramètres σ , correspondant à la réponse instrumentale, et τ , la durée de vie de la fluorescence, sont ensuite déterminés.



Déclin de fluorescence Le paramètre A correspond à l'amplitude maximale de l'intensité de lumière, μ est la position du déclin et C correspond à la moyenne du bruit de fond *avant* le déclin.

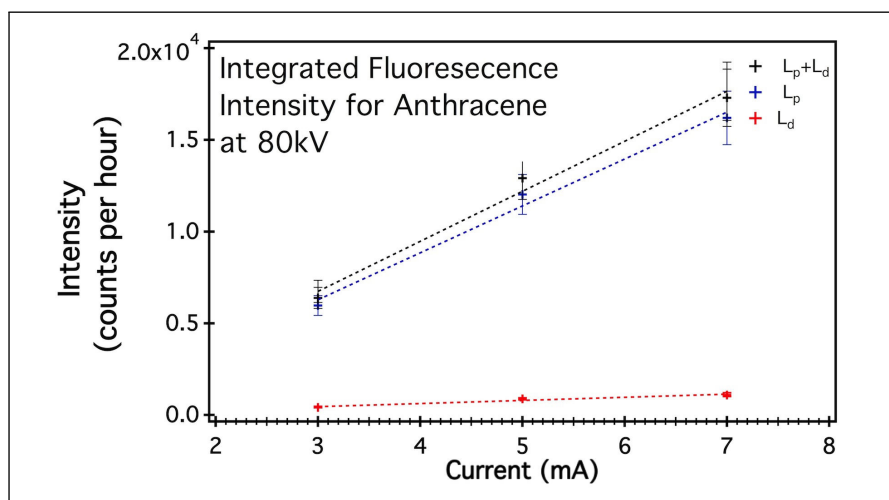
On présente ensuite les résultats obtenus pour différentes conditions d'utilisation de la source de rayons X. Les paramètres d'expériences ont été choisis de manière particulière, afin de pouvoir faire correspondre l'étude des scintillateurs modèles et celle de la fibre optique à la situation réelle d'un examen clinique. Les paramètres étaient les suivants : tension appliquée au tube (énergie maximale des photons), courant dans le tube (flux de photons). Les études ont porté sur les doses déposées et les débits de doses. Pour chaque mesure, des comparaisons ont été faites avec une dosimétrie par chambre d'ionisation normalisée. Ensuite, on présente quelques résultats expérimentaux.

Déclin de fluorescence:

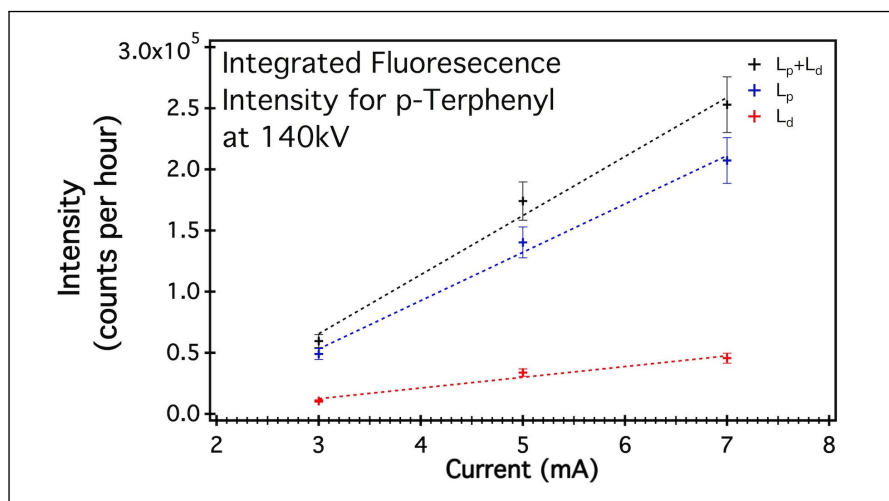


Déclin de fluorescence du p-terphenyle irradié par de rayons X. La composante lente du déclin suit une loi temporelle en puissance $t^{-3/2}$ du temps, conforme au modèle de diffusion de Debye-Smolukowsky.

Réponses de scintillateurs aux variations du courant à différentes tensions constantes :

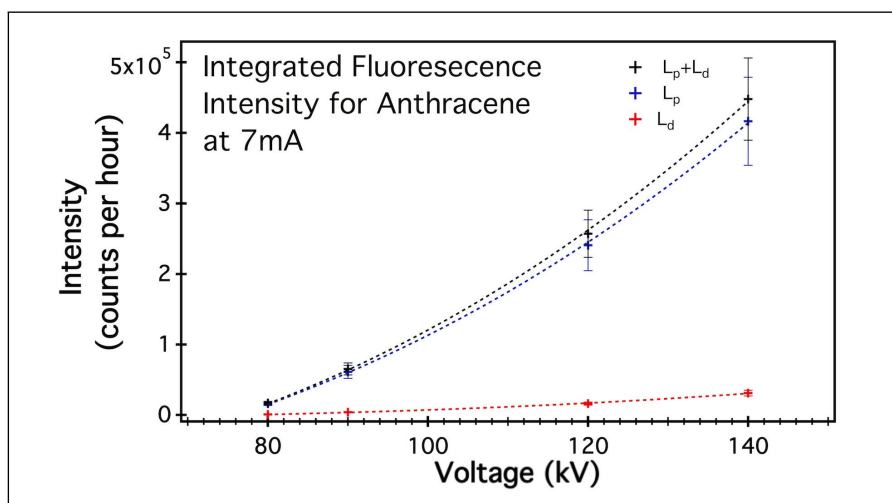


Intégrale totale du déclin de fluorescence de l'anthracène avec le tube de rayons X réglé avec une tension de 80kV et un courant variant entre 3 et 7mA. Les réponses observées sur les composantes lentes L_p et rapides L_d sont linéaires. La réponse totale $L_p + L_d$ est également linéaire.

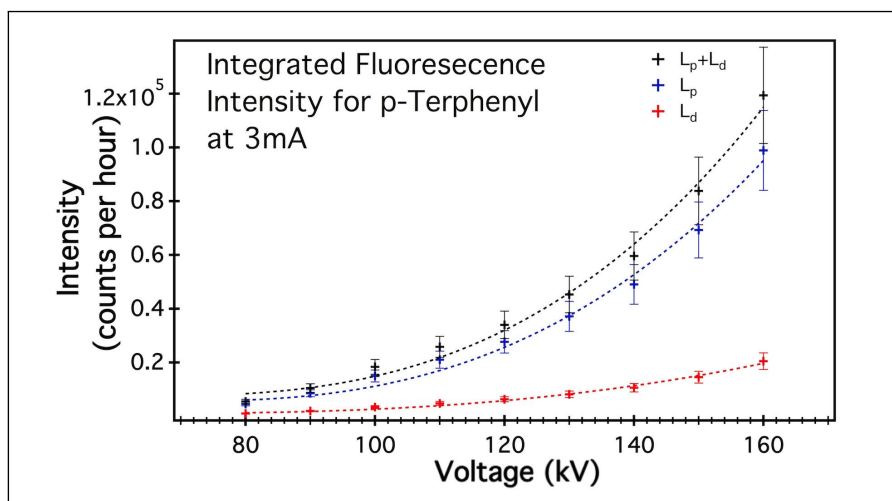


Intégrale totale du déclin de fluorescence du p-terphényle avec le tube de rayons X réglé avec une tension de 140kV et un courant variant entre 3 et 7mA. Les réponses observées sur les composantes lentes L_p et rapides L_d sont linéaires. La réponse totale $L_p + L_d$ est également linéaire.

Réponses de scintillateurs aux variations de la tension à différents courants constants :

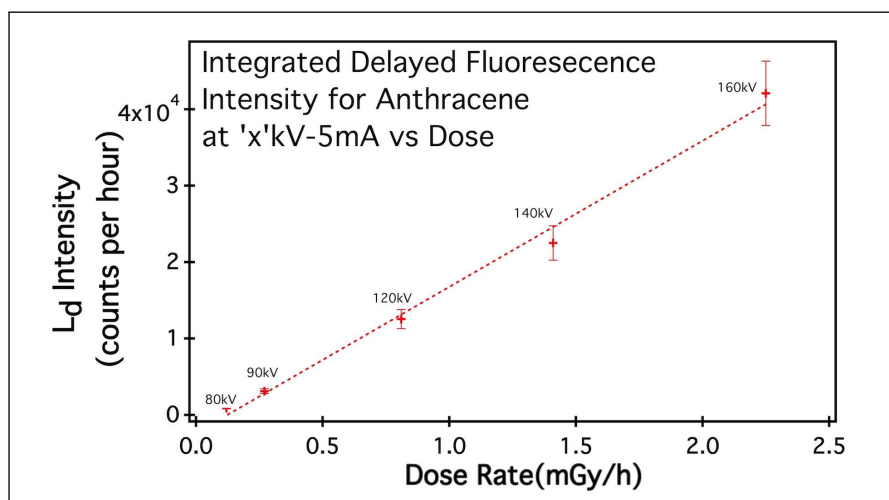


Intégrale totale du déclin de fluorescence de l'anthracène avec le tube de rayons X réglé avec un courant de 7mA et différentes tensions variant entre 80 et 140kV. Les réponses observées à partir des composante lente L_p et rapide L_d varient au carré ainsi que la réponse totale $L_p + L_d$.

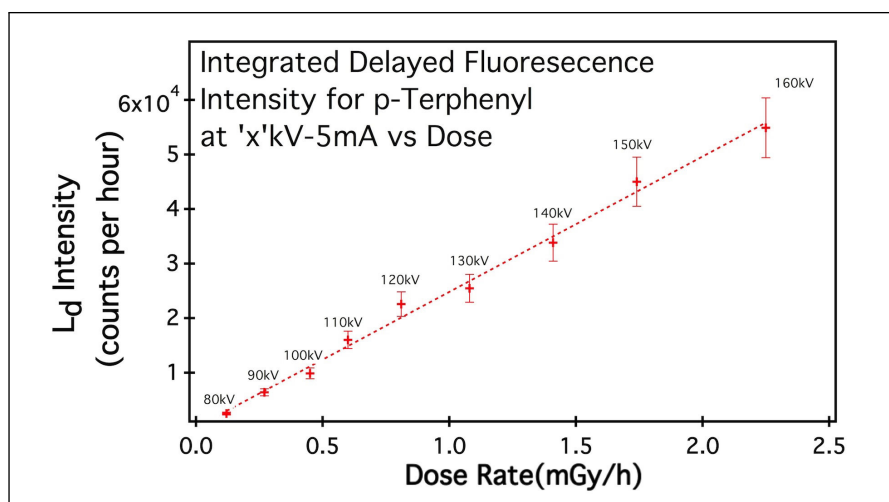


Intégrale totale du déclin de fluorescence du p-terphényl avec le tube de rayons X réglé avec un courant de 3mA et différentes tensions variant entre 80 et 140kV. Les réponses observées à partir des composante lente L_p et rapide L_d varient au carré ainsi que la réponse totale $L_p + L_d$.

Relation entre le débit de dose et la composante lente:



l'intégrale de la composante lente de l'anthracène en fonction du débit de dose mesuré par la chambre d'ionisation.



Intégrale de la composante lente du p-terphényle en fonction du débit de dose mesuré par la chambre d'ionisation.

Chapitre 5

Conclusions et perspectives

Le dernier chapitre est une discussion des résultats obtenus au regard des connaissances fondamentales acquises depuis l'origine des études sur les scintillateurs organiques, auxquelles s'ajoutent les différentes contributions nouvelles de ce travail de thèse. Il se décompose en deux grandes parties.

La première partie porte sur l'étude des déclin de fluorescence en fonction de l'énergie maximale du spectre de rayons X, à flux constant, dans une gamme allant de 80 keV à 140 keV. Les contributions des phénomènes d'excitation et d'ionisation sont déduites, sur l'ensemble de la gamme d'énergie, par intégrations successives des données expérimentales après extraction des composantes, respectivement rapides et lentes. Les données font apparaître, pour la première fois, que les rendements relatifs aux deux phénomènes d'excitation et d'ionisation sont constants avec l'énergie d'excitation, ce qui indique que les contributions respectives des canaux excitation et d'ionisation à la dégradation de l'énergie primaire n'évolue que très peu sur la gamme d'énergie des rayons X médicaux. Les résultats obtenus sur les composantes lentes aux différentes énergies sont en accords avec ceux mesurés par dosimétrie conventionnelle par chambre d'ionisation, ce qui n'avait jamais été établi auparavant, mais s'explique par les modèles développés dans ce travail. Par ailleurs, une contribution non négligeable de l'excitation moléculaire, non ionisante, est mise en évidence, laquelle n'est jamais prise en compte dans les normes de la dosimétrie conventionnelle alors qu'elle correspond bien à un dépôt de dose pouvant conduire à des effets transitoire et permanents. Ce dépôt de dose, que la technique développée dans ce travail est actuellement la seule capable de détecter, avait déjà été observé dans travaux de thèse récent du groupe, dans le cadre de la synthèse de nouvelles molécules scintillantes pour la discrimination neutron-gamma et aussi, lors d'une étude portant sur la hadronthérapie par faisceaux de carbone.

La deuxième partie porte sur l'étude des déclin de fluorescence en fonction du flux de photons, à énergie maximale constante. Le premier résultat important de l'étude montre que, dans tous les cas de figure, il n'existe pas de phénomène de saturation du signal de

fluorescence avec la dose et le débit de dose. Ceci indique que les dépôts, aussi bien en excitation qu'en ionisation, sont isolés et conduisent à la production de paires électron trou spatialement décorréliées les unes des autres. Ceci était évidemment attendu dans le cas d'un flux de photons issu d'un tube à rayons X car déjà observé dans le pic de Bragg lors d'études précédentes de notre équipe avec des faisceaux d'ions à hauts TEL. Ce résultat est néanmoins original pour les rayons X. Au-delà, il pose la question de l'observation, par différents auteurs, d'un phénomène de saturation de la luminescence, particulièrement en scintillation liquide lorsque l'on utilise qu'un seul photomultiplicateur pour la mesure. Ce phénomène, toujours interprété par une saturation du milieu, est, selon nous, à attribuer davantage à une saturation instrumentale, ce qui remet en question de nombreuses études. Il apparaît ici, que l'utilisation de deux photodétecteurs fonctionnant en coïncidence constitue une approche instrumentale bien meilleure. Découlant de ces observations, celles d'un rapport constant, avec la dose et le débit de dose, des rendements d'excitation et d'ionisation, également observée pour la première fois avec des photons, est alors évidente à interpréter.

En conclusion de ce travail, on rappelle les principaux points originaux des études théoriques et expérimentales réalisées, ainsi que leur très bon accord. La contribution de ce travail, additionnée, à celles déjà effectuées dans l'équipe, ouvre d'importantes perspectives en recherche fondamentale, mais aussi en recherche appliquée, particulièrement dans la prise en compte des doses déposées dans un milieu par excitation moléculaire non ionisante et la future mise en corrélation de ces doses avec les dégâts induits. A ce jour, la plupart des études peinent à mettre en corrélation la dose déposée par ionisation avec les dégâts infligés, particulièrement à l'échelle cellulaire. De ce point de vue, il nous semble important que des études nouvelles soient entreprises afin d'introduire la contribution des phénomènes d'excitation dans les modélisations et les expériences, mais aussi dans les normes de radioprotection au sens large.

Bibliography

- [1] R. Loudon, *The quantum theory of light*. Oxford university press, 2000.
- [2] J. D. Jackson and J. D. Jackson, *Classical electrodynamics*, vol. 3. Wiley New York etc., 1962.
- [3] C. Cohen-Tannoudji, B. Diu, and F. Laloë, *Quantum Mechanics, Volume I*. Wiley and Hermann, 1977.
- [4] O. Keller, *Light-The Physics of the Photon*. CRC Press, 2014.
- [5] J. D. Jackson, “From lorentz to coulomb and other explicit gauge transformations,” *American Journal of Physics*, vol. 70, no. 9, pp. 917–928, 2002.
- [6] G. C. Schatz and M. A. Ratner, *Quantum mechanics in chemistry*. Courier Corporation, 2002.
- [7] J.-L. Basdevant and J. Dalibard, “The lagrangian and hamiltonian formalisms, lorentz force in quantum mechanics,” *Quantum Mechanics*, pp. 293–308, 2005.
- [8] M. O. Scully, *Quantum optics*. Cambridge university press, 1997.
- [9] O. Hemmers, R. Guillemin, and D. W. Lindle, “Nondipole effects in soft x-ray photoemission,” *Radiation physics and chemistry*, vol. 70, no. 1, pp. 123–147, 2004.
- [10] E. A. Power., *Introductory quantum electrodynamics*. Longman, London, 1964.
- [11] G. F. Knoll, *Radiation detection and measurement*. John Wiley & Sons, 2010.
- [12] J. Beutel, H. L. Kundel, and R. L. Van Metter, *Handbook of Medical Imaging, volume 1: Physics and Psychophysics*. Spie Press Bellingham, Washington, 2000.
- [13] J. H. Hubbell, “Photon cross sections, attenuation coefficients, and energy absorption coefficients from 10 kev to 100 gev,” tech. rep., DTIC Document, 1969.

Bibliography

- [14] M. J. Cooper, A. Bansil, P. E. Mijnarends, N. Sakai, and N. Shiotani, *X-ray Compton scattering*. Oxford Univ., 2004.
- [15] C. Leroy and P.-G. Rancoita, *Principles of radiation interaction in matter and detection*, vol. 2. World Scientific, 2009.
- [16] M. J. Berger, J. Hubbell, S. Seltzer, J. Chang, J. Coursey, R. Sukumar, D. Zucker, and K. Olsen, “Xcom: photon cross sections database,” *NIST Standard reference database*, vol. 8, no. 1, pp. 3587–3597, 1998.
- [17] N. PSTAR, “Stopping power and range tables for protons,” *PSTAR. html*, 2009.
- [18] J. Ashley, C. Tung, and R. Ritchie, “Inelastic interactions of electrons with polystyrene: Calculations of mean free paths, stopping powers, and csda ranges,” *Nuclear Science, IEEE Transactions on*, vol. 25, no. 6, pp. 1566–1570, 1978.
- [19] J. F. Ziegler, M. Ziegler, and J. Biersack, “Srim—the stopping and range of ions in matter (2010),” *Nuclear Instruments and Methods in Physics Research Section B: Beam Interactions with Materials and Atoms*, vol. 268, no. 11, pp. 1818–1823, 2010.
- [20] N. ESTAR, “Stopping power and range tables for electrons,” *ESTAR. html*, 2009.
- [21] F. Brooks, “Development of organic scintillators,” *Nuclear Instruments and Methods*, vol. 162, no. 1, pp. 477–505, 1979.
- [22] D. L. Horrocks, *Organic scintillators*. Gordon and Breach, 1968.
- [23] A. Beierholm, C. Andersen, L. Lindvold, F. Kjær-Kristoffersen, and J. Medin, “A comparison of bcf-12 organic scintillators and al₂o₃:c crystals for real-time medical dosimetry,” *Radiation Measurements*, vol. 43, no. 2, pp. 898–903, 2008.
- [24] R. L. Platzman, “Superexcited states of molecules,” *Radiation Research*, vol. 17, no. 3, pp. 419–425, 1962.
- [25] G. Klein and R. Voltz, “Formation and decay of superexcited states in dense organic matter under high energy radiation,” *International Journal for Radiation Physics and Chemistry*, vol. 7, no. 2, pp. 155–174, 1975.
- [26] Y. Hatano, “Interaction of photons with molecules—cross-sections for photoabsorption, photoionization, and photodissociation,” *Radiation and environmental biophysics*, vol. 38, no. 4, pp. 239–247, 1999.

-
- [27] K. Feron, W. J. Belcher, C. J. Fell, and P. C. Dastoor, "Organic solar cells: Understanding the role of förster resonance energy transfer," *International journal of molecular sciences*, vol. 13, no. 12, pp. 17019–17047, 2012.
- [28] G. Klein, "Production of pairs of singlet excitons and triplet excitons in anthracene crystals," *Chemical Physics Letters*, vol. 97, no. 1, pp. 114–118, 1983.
- [29] G. Laustriat, "The luminescence decay of organic scintillators," *Molecular Crystals*, vol. 4, no. 1-4, pp. 127–145, 1968.
- [30] R. Voltz and G. Laustriat, "Radioluminescence des milieux organiques i. étude cinétique," *Journal de Physique*, vol. 29, no. 2-3, pp. 159–166, 1968.
- [31] K. Falkowski, W. Stampor, P. Grygiel, and W. Tomaszewicz, "Sano–tachiya–noolandi–hong versus onsager modelling of charge photogeneration in organic solids," *Chemical Physics*, vol. 392, no. 1, pp. 122–129, 2012.
- [32] L. Onsager, "Initial recombination of ions," *Physical Review*, vol. 54, no. 8, p. 554, 1938.
- [33] S. P. McGlynn, T. Azumi, and M. Kinoshita, *Molecular spectroscopy of the triplet state*. Prentice-Hall, 1969.
- [34] G. G. Guilbault, *Practical fluorescence*, vol. 3. CRC Press, 1990.
- [35] D. L. Horrocks, "Pulse shape discrimination with organic liquid scintillator solutions," *Applied Spectroscopy*, vol. 24, no. 4, pp. 397–404, 1970.
- [36] R. Voltz, H. Dupont, and G. Laustriat, "Radioluminescence des milieux organiques. ii. vérification expérimentale de l'étude cinétique," *Journal de Physique*, vol. 29, no. 4, pp. 297–305, 1968.
- [37] C. Parker and C. Hatchard, "Delayed fluorescence from solutions of anthracene and phenanthrene," *Proceedings of the Royal Society of London. Series A. Mathematical and Physical Sciences*, vol. 269, no. 1339, pp. 574–584, 1962.
- [38] W. L. Buck, "The origin of scintillations in organic materials," *Nuclear Science, IRE Transactions on*, vol. 7, no. 2-3, pp. 11–16, 1960.
- [39] J. L. Da Silva and R. Voltz, "Variation du rendement de radioluminescence des scintillateurs organiques avec la perte d'énergie et le nombre de charges des particules ionisantes," *Revue de Physique Appliquée*, vol. 7, no. 2, pp. 127–132, 1972.

Bibliography

- [40] R. Kepler, J. Caris, P. Avakian, and E. Abramson, "Triplet excitons and delayed fluorescence in anthracene crystals," *Physical Review Letters*, vol. 10, no. 9, p. 400, 1963.
- [41] J.-M. JUNG, *Photoproduction, thermalisation et recombinaison de paires de charges dans les liquides moléculaires*. PhD thesis, Université de Strasbourg I, 1991.
- [42] J.-M. JUNG, "Photoionisation des liquides moléculaires," habilitation à diriger de recherches, Université de Strasbourg I, 2003.
- [43] T. Murai, T. Nakamura, and A. Yamamoto, "A new method of integral dose measurement with a plastic scintillator phantom," *Journal of radiation research*, vol. 5, no. 1, pp. 23–34, 1964.
- [44] "Beam characterization studies at nsrl," tech. rep., NSRL, 2010.
- [45] R. Craun and D. Smith, "Analysis of response data for several organic scintillators," *Nuclear Instruments and Methods*, vol. 80, no. 2, pp. 239–244, 1970.
- [46] E. Brannen and G. L. Olde, "The response of organic scintillators to electron energy deposited in them," *Radiation research*, vol. 16, no. 1, pp. 1–6, 1962.
- [47] J. Birks and F. Brooks, "Scintillation response of anthracene to 6-30 kev photoelectrons," *Proceedings of the Physical Society. Section B*, vol. 69, no. 7, p. 721, 1956.
- [48] A. Beddar, T. Mackie, and F. Attix, "Water-equivalent plastic scintillation detectors for high-energy beam dosimetry: II. properties and measurements," *Physics in medicine and biology*, vol. 37, no. 10, p. 1901, 1992.
- [49] W. Busjan, K. Wick, and T. Zoufal, "Shortlived absorption centers in plastic scintillators and their influence on the fluorescence light yield," *Nuclear Instruments and Methods in Physics Research Section B: Beam Interactions with Materials and Atoms*, vol. 152, no. 1, pp. 89–104, 1999.
- [50] I. Rosman and K. Zimmer, "Damage to plastic scintillators by ionizing radiation," *The Soviet Journal of Atomic Energy*, vol. 2, no. 1, pp. 57–62, 1957.
- [51] Z. Li, W. Chong, H. Yuekun, Z. Xiaojian, S. Feng, S. Zhijia, W. Jinjie, A. Zhenghua, Z. Yuda, Z. Ziping, *et al.*, "Properties of plastic scintillators after irradiation," *Nuclear Instruments and Methods in Physics Research Section A: Accelerators, Spectrometers, Detectors and Associated Equipment*, vol. 552, no. 3, pp. 449–455, 2005.
- [52] G. Shani, *Radiation dosimetry instrumentation and methods*. CRC Press, 2000.

-
- [53] J. R. Greening, *Fundamentals of radiation dosimetry*. CRC Press, 1985.
- [54] G. Alm Carlsson, "Bragg-gray dosimetry: Theory of burch," tech. rep., Östergötlands Läns Landsting, Department of Radiation Physics, 2001.
- [55] A. J. Bos, A. Rosenfeld, T. Kron, F. d'Errico, and M. Moscovitch, "Fundamentals of radiation dosimetry," in *AIP Conference Proceedings-American Institute of Physics*, vol. 1345, p. 5, 2011.
- [56] J. A. Haider, L. D. Skarsgard, and G. K. Lam, "A general cavity theory," *Physics in medicine and biology*, vol. 42, no. 3, p. 491, 1997.
- [57] J. B. Birks, *The theory and practice of scintillation counting*. Pergamon, 1964.
- [58] R. Voltz, J. L. Da Silva, G. Laustriat, and A. Coche, "Influence of the nature of ionizing particles on the specific luminescence of organic scintillators," *The Journal of Chemical Physics*, vol. 45, no. 9, pp. 3306–3311, 1966.
- [59] D. Horrocks, *Organic Scintillators and Scintillation Counting*. Elsevier, 1971.
- [60] T. Iwata, H. Shibata, and T. Araki, "A deconvolution procedure for determination of a fluorescence decay waveform applicable to a band-limited measurement system that has a time delay," *Measurement Science and Technology*, vol. 19, no. 1, p. 015601, 2008.
- [61] D. O'Connor, *Time-correlated single photon counting*. Academic Press, 1984.
- [62] T. Salthammer, "Numerical simulation of pile-up distorted time-correlated single photon counting (tcspc) data," *Journal of fluorescence*, vol. 2, no. 1, pp. 23–27, 1992.
- [63] S. Dong, Q. Zhou, W. Zhang, Y. He, W. Zhang, L. You, Y. Huang, and J. Peng, "Energy-time entanglement generation in optical fibers under cw pumping," *Optics express*, vol. 22, no. 1, pp. 359–368, 2014.
- [64] C. Eckart and F. R. Shonka, "Accidental coincidences in counter circuits," *Physical Review*, vol. 53, no. 9, p. 752, 1938.
- [65] K. Hamamatsu Photonics, "Photomultiplier tubes: Basics and applications," *Edition 3a*, 2006.
- [66] R. C. Sangster and J. W. Irvine Jr, "Study of organic scintillators," *The Journal of Chemical Physics*, vol. 24, no. 4, pp. 670–715, 1956.

- [67] P. Martin, *Photoexcitation de la fluorescence de recombinaison différée dans l'ultra-violet lointain et relaxation des états super-excités dans les cristaux moléculaires organiques*. PhD thesis, Université de Strasbourg I, 1993.
- [68] T.-S. Ahn, A. M. Müller, R. O. Al-Kaysi, F. C. Spano, J. E. Norton, D. Beljonne, J.-L. Brédas, and C. J. Bardeen, "Experimental and theoretical study of temperature dependent exciton delocalization and relaxation in anthracene thin films," *The Journal of chemical physics*, vol. 128, no. 5, p. 054505, 2008.
- [69] M. Sluch, A. Averjushkin, O. Tolstikhin, and A. Vitukhnovsky, "Influence of reabsorption on fluorescence lifetime of molecular crystals at α -particle excitation," *Physica Scripta*, vol. 50, no. 5, p. 585, 1994.
- [70] J. A. Seibert, "X-ray imaging physics for nuclear medicine technologists. part 1: Basic principles of x-ray production," *Journal of nuclear medicine technology*, vol. 32, no. 3, pp. 139–147, 2004.
- [71] Y. Nievergelt, "Total least squares: State-of-the-art regression in numerical analysis," *SIAM review*, vol. 36, no. 2, pp. 258–264, 1994.
- [72] N. Mastronardi, P. Lemmerling, and S. Van Huffel, "Fast structured total least squares algorithm for solving the basic deconvolution problem," *SIAM Journal on Matrix Analysis and Applications*, vol. 22, no. 2, pp. 533–553, 2000.
- [73] N. Mastronardi, P. Lemmerling, and S. Van Huffel, "Fast regularized structured total least squares algorithm for solving the basic deconvolution problem," *Numerical linear algebra with applications*, vol. 12, no. 2-3, pp. 201–209, 2005.
- [74] S. Basharin, G. Gachko, L. Kivach, S. Maskevich, A. Maskevich, and V. Udovydchenko, "Deconvolution of fluorescence decay curves," *Journal of Applied Spectroscopy*, vol. 52, no. 1, pp. 32–36, 1990.
- [75] D. O'Connor, W. Ware, and J. Andre, "Deconvolution of fluorescence decay curves. a critical comparison of techniques," *Journal of Physical Chemistry*, vol. 83, no. 10, pp. 1333–1343, 1979.
- [76] N. Periasamy, "Analysis of fluorescence decay by the nonlinear least squares method," *Biophysical journal*, vol. 54, no. 5, pp. 961–967, 1988.
- [77] W. R. Ware, L. J. Doemeny, and T. L. Nemzek, "Deconvolution of fluorescence and phosphorescence decay curves. least-squares method," *The Journal of Physical Chemistry*, vol. 77, no. 17, pp. 2038–2048, 1973.

- [78] D. Hanggi and P. W. Carr, "Errors in exponentially modified gaussian equations in the literature," *Analytical Chemistry*, vol. 57, no. 12, pp. 2394–2395, 1985.
- [79] V. B. Di Marco and G. G. Bombi, "Mathematical functions for the representation of chromatographic peaks," *Journal of Chromatography A*, vol. 931, no. 1, pp. 1–30, 2001.
- [80] Y. Hatano, Y. Katsumura, and A. Mozumder, *Charged particle and photon interactions with matter: Recent advances, applications, and interfaces*. CRC Press, 2011.
- [81] B. Brocklehurst, "Spin correlation and magnetic field effects in radiolysis," *Radiation Physics and Chemistry*, vol. 50, no. 3, pp. 213–225, 1997.
- [82] C. Ferradini and J.-P. Jay-Gerin, *Excess electrons in dielectric media*. CRC press, 1991.